NOTE TO USERS

Contact parameter estimation using a space manipulator verification facility

Julie Agar

Department of Mechanical Engineering

McGill University

Montreal, Canada

November 2004

A thesis submitted to McGill University in partial fulfillment of the requirements of the degree of Master of Engineering.

Your file Votre référence
ISBN: 0-494-12574-8
Our file Notre référence
ISBN: 0-494-12574-8

Abstract

Computer simulations play an important role in the design and verification of space robotic operations since on-orbit tests are impossible to conduct before launch. Thus, accurate computer modelling and simulation of space robotic tasks is essential. Of particular difficulty are space manipulator operations, which involve constrained or contact tasks. Here, the contact dynamics capability in the modelling tools becomes critical for high fidelity simulation. This in turn implies a need for accurate determination of contact parameters, which are used as inputs to contact dynamics simulation. In this work, the identification of contact dynamics parameters based on sensor data obtained during robotic contact tasks is considered.

The contact parameter estimation problem is addressed for simple and complex contacting geometries using the SPDM Task Verification Facility Manipulator Test-bed (SMT) at the Canadian Space Agency. The SMT is a space-representative robotic simulation facility. Single- and multiple-point contact parameter estimation software toolboxes were developed and used with SMT experiments. Single point SMT contact experiments were performed with six different payloads. The single point toolbox was used as part of the process of identifying payload stiffness from SMT experimental data.

Multiple point contact parameter estimation experiments with the SMT were conducted using a mock-up of an International Space Station Arm Computer Unit (ACU) as payload. The multiple point toolbox was used to generate contact stiffness, damping and friction estimates. An evaluation of the sensitivity of the parameter estimation algorithm to mismatches in ACU physical dimensions and ACU geometry files was conducted.

Résumé

Les simulations jouent un rôle important dans la conception et la vérification des opérations robotiques de l'espace étant donné l'impossibilité de faire des tests en orbite avant le lancement. La modélisation et la simulation des tâches spatiales sont donc essentielles. Les opérations des manipulateurs spatiaux comprenant des tâches de contact ou forcées sont particulièrement difficiles. Une bonne dynamique de contact dans les outils de modélisation est critique dans l'obtention de simulations précises. Ceci implique une nécessité de déterminer exactement les paramètres de contacts utilisés comme entré dans les simulations de dynamique de contact. Finalement, l'identification des paramètres de dynamique de contact basée sur des données sensorielles obtenues lors de tâches robotiques de contact est considérée.

Le problème d'estimation des paramètres de contact s'adresse à des géométries simples et complexes en utilisant le SPDM Task Verification Facility Manipulator Test-bed (SMT) a l'Agence Spatiale Canadienne. Le SMT est un banc d'essai robotique permettant des simulations représentatives de l'espace. Des "software librairies" pour l'estimation de paramètres de contact d'un ou plusieurs points ont été développées et utilisées lors d'expériences avec le SMT. Des expériences de contact à un seul point ont été exécutées avec six charges différentes sur le SMT. La librairie a été utilisée dans le processus d'identification de la rigidité des charges à partir des données expérimentales du SMT.

L'estimation de paramètres de contact à points multiples a été exécutée sur le SMT en utilisant un modèle du Arm Computer Unit (ACU) de la Station Spatiale Internationale comme charge. La librairie pour points multiples a été utilisée pour générer des estimations de rigidité, d'amortissement et de friction. Une évaluation de la sensibilité de l'algorithme d'estimation de paramètres aux différences entre les dimensions du ACU et les fichiers de la géométrie du ACU a été effectuée.

Table of Contents

List of Figures

List of Tables

Acknowledgements

I would like to thank my supervisor, Dr. Inna Sharf, and my co-supervisor, Dr. Christian Lange, for their ongoing support and patience during this research. I would also like to thank Yves Gonthier at the Canadian Space Agency (CSA) for his assistance and support throughout.

I wish to acknowledge Stefan Rondeau and Dr. Christian Lange of CSA for their assistance in conducting experiments with the STVF robotic facility. I would like to thank the machine shop at CSA for manufacturing the robotic payloads. Thanks are also extended to the department of Chemical Engineering at McGill University for allowing me to use their Instron material testing machine and especially to Nitin Borse for offering his time to instruct me on the use of this machine. Thanks are also given to Wael Dabboussi for introducing me to finite element modelling.

Funding for this research was provided by the Natural Sciences and Engineering Research Council of Canada (NSERC) and the Canadian Space Agency.

Chapter 1

Introduction

1.1 Parameter Estimation

The engineering design process is often aided through the practice of characterizing a physical system with a mathematical model. Physical systems can be represented by mathematical models of varying degrees of complexity, which in turn depends upon the desired end use of the model. In the matter of control engineering, algebraic and differential equations are commonly used to model the dynamic behaviour of a system. The coefficients of the mathematical equations that govern these dynamic processes are considered as the model *parameters*. In some cases, the values of these parameters are unknown, and hence, an important aspect of the study of engineering is the extraction of parameter information from available input and output data. Most usually, the model parameters have physical significance and are termed *properties*. Examples of parameters that may also be properties are density, Young's modulus, viscosity and electrical capacitance. *Parameter estimation* is the term used to refer to the process of estimating or identifying the model parameters from the input and output data, while assuming knowledge of the model details. Eykhoff [1] states, *"the use of the word estimation is due to the fact that in almost all realistic situations the observations made on the system under study are contaminated with random influences (disturbances, errors)."* In the presence of these disturbances, statistical procedures can be used to find the best parameter estimation results from the input and output measurements.

The subject of parameter estimation (or parameter identification) is studied in many disciplines such as mechanical engineering, electrical engineering, aerospace

engineering, civil engineering, and biomedical engineering. Examples of parameter estimation problems being studied in some of these fields are described below:

- In the field of aerospace engineering, parameter estimation methods have been developed by Lo et al. [2] to provide estimates of the speed and altitude of low-flying jet aircraft, travelling with uniform linear motion over solid ground. The methods developed use the temporal variation between the arrival of ground-reflected signals and direct path signals emitted by the jet aircraft to determine the parameters.
- Roux et al. [3] have conducted research in the field of hydraulic parameter identification. Aerial photographs of a flooded river were used to determine hydraulic parameters necessary for flood simulation studies. Some of the characterizing parameters identified by Roux et al. include discharge, Manning roughness coefficients and geometry of the river cross-section.
- Hahn et al. [4] have researched parameter identification in the area of vehicle control systems. With the intention of making these control systems adaptive to changes in the road, Hahn et al. developed a real-time identification algorithm for the tire-road friction coefficient used in the vehicle control method. Additionally, work has also been done in real-time identification of the road-bank angle, another significant disturbance in the vehicle steering control [5].
- Wang et al. [6] developed a genetic algorithm for identifying friction parameters in pneumatic actuator systems after they have been manufactured and assembled, where direct determination of the friction parameters cannot be done.
- Parameter estimation is a popular subject in the area of motors and synchronous generators. In Karayaka et al. [7] small excitation disturbances are used to identify linear model armature circuit and field winding parameters. Parameter estimation is useful in this field because aging and use of the machine mean that machine parameters can deviate significantly from their original manufactured specifications. Kim et al. [8] applied a recently developed optimization algorithm to the problem of identification of induction motor parameters, such as stator and rotor resistance and inductance.

- Li et al. [9] presented an identification algorithm using fuzzy theory and genetic algorithms to identify joint parameters (equivalent stiffness and damping coefficients) in robots.
- Lefebvre et al. [10] presented an optimization method to identify inaccurately known position and orientation information of contacting objects in compliant robotic tasks.

The last two examples discuss parameter estimation in the field of robotics, which is of particular interest to the work presented here. Continued advances in computer technology have made real-time (or *online*) solutions to the parameter estimation problem feasible and practical. Real-time solutions allow parameter estimation to play an important role in the field of robotics, where the ability to have robots adapt to situations in real-time is useful. In this thesis, however, the focus remains solely on *offline* parameter estimation for robotic contact tasks. *Offline* parameter estimation refers to carrying out parameter estimation after the experiments of interest have been fully completed. In this situation, the entirety of the input and output data is available for processing, and the resulting parameter estimates can be used to improve future performance of the robotic task in question.

1.2 Robotics and Space Robotics

Robotic operations are generally classified into two categories: unconstrained and constrained tasks. Unconstrained tasks refer to situations where the manipulator is instantaneously free to move in any direction without making contact with the environment. Examples of unconstrained robotic tasks include spray painting and visual inspection tasks. A constrained task occurs when the manipulator interacts with the environment through one or more points of contact. Examples of constrained tasks include spot-welding, cutting, grinding or assembly operations. Of specific interest here is the study of parameter estimation for *constrained* robotic tasks.

Robotic manipulators are often designed to resemble the human arm and wrist and are ultimately used to substitute for human labour. This is especially important and valid for

tasks that are difficult to execute or those that must be performed in dangerous environments. The assembly of the International Space Station (ISS) is a good example of a project that relies on the use of robots for construction tasks in a dangerous environment.

1.2.1 The International Space Station

As part of the multi-national collaboration to build the International Space Station, Canada's main contribution, through the Canadian Space Agency (CSA), is the Mobile Servicing System (MSS). The MSS, used for ISS assembly and maintenance, has two manipulator systems as its main components: the Space Station Remote Manipulator System (SSRMS) and the Special Purpose Dexterous Manipulator (SPDM). The research here is particularly related to the SPDM, which is scheduled to launch in 2007. The SPDM is being developed by Macdonald Dettwiler Space and Advanced Space Robotics Ltd. (MD Robotics) for CSA. The SPDM is composed of two 3.5 metre arms, each having seven joints. Mounted on a rotating body, it has a total of 15 degrees of freedom (DOF) [11]. The SPDM will perform many constrained operations. It is responsible for handling various Orbital Replacement Units (ORUs) during maintenance of the space station.

The complexity of the contact and insertion tasks performed by the SPDM suggests a need for an on-ground verification facility to be used to confirm that a specified task can be performed in orbit as intended. The SPDM Task Verification Facility (STVF) was developed as the on-earth verification facility by CSA. The dynamics of the SPDM end-effector is emulated with the STVF manipulator test-bed (SMT) using a hardware-in-the-loop simulation scheme, in which components of the simulated system are replaced by physical parts [11]. The SMT has been used by CSA to conduct experimental contact parameter estimation for general contact dynamics modeling software [41]. In the present thesis, the SMT and the experiments conducted by CSA [41] are of particular interest in the research of parameter estimation. This thesis presents work and results covering single and multiple point contact experimentation and contact parameter identification with the SMT.

1.3 Contact Parameter Estimation in Robotics

As mentioned in Section 1.2, many robotic tasks involve some form of contact with the environment or objects in the environment. Constrained, or contact tasks encompass some of the most difficult aspects of robotic operations. When contact occurs, the manipulator may experience significant disturbances that can perturb the control systems. In this research we are interested in contact tasks of space station manipulators. A major complication that arises when dealing with space-based manipulators is the inability to conduct on-orbit tests before the launch of the manipulator. Furthermore, ground-based physical tests, such as those conducted with the SMT facility at the CSA, cannot be made completely space-representative for the entire system. Due to these limitations, accurate computer modelling and simulations play an essential role in supporting the design, development and operation of space robotics systems.

In terms of multi-body dynamics computer modelling and simulation, there are currently several approaches available to model the contact dynamics associated with constrained tasks [12 - 16]. MD Robotics has developed a generic Contact Dynamics Toolkit (CDT) as part of their Manipulator Development and Simulation Facility (MDSF) [14]. Their work in contact dynamics modelling and simulation has played an essential role in the development of the new Canadian space robots for use on the ISS. However, successful computer modelling and simulation depends on two main elements. First, the fidelity of the simulation facility is key. In particular, the validity of the fundamental modelling theories, numerical algorithms, computer software and simulation processing defines the reliability of the simulation facility. Second, the accuracy of the model parameters used as inputs to the simulation software to represent the physical system being simulated is of great importance. MD Robotics has expended considerable effort addressing the first element with CDT. Of interest to us in this thesis is the second element, specifically the problem of determining model parameters required for contact dynamics simulation. This problem is referred to as *contact parameter estimation* in this thesis. The parameters that are of main interest for identification in this work are the stiffness, damping and friction parameters of the contact interface between a payload and its environment.

Under ideal circumstances, manipulator sensor data obtained during space operations would be used to identify the space-environment contact parameters. Using well-calibrated position, velocity and force sensor information from space manipulators and mathematical contact force models, the contact dynamics parameters for the system could be estimated. It is desired, and expected, that the contact parameters determined with the contact parameter estimation procedure would result in the confident use of contact dynamics simulations to support space-based operations and mission planning.

1.4 Background on Robotic Contact Parameter Estimation

The starting point for our work arose from research dealing with the problem of environment estimation in the context of robot impedance control [17, 18, 20]. Singh and Popa (1995) [17] showed that model reference adaptive control (MRAC) could be applied to impedance force control to realize force tracking for a linear system. Estimates of the environment contact parameters were required. Seraji and Colbaugh (1997) presented a force tracking impedance controller by estimating the environment stiffness and location [18] using either direct or indirect adaptive control. Love and Book [20] showed that improved stability during contact operations could be achieved using environment parameter estimation. Their work established how environment impedance parameter estimates could allow an impedance controller to maintain stability during and at the onset of contact [20]. Furthermore, they showed that inaccurate environment parameter estimates could potentially result in unstable contact.

1.4.1 Single Point Contact Parameter Estimation

The original research in environment parameter estimation began an on-going effort to address the contact parameter estimation problem. The work on contact parameter estimation has evolved through several phases, and began with a focus on the simple contact geometry parameter estimation scenario. This initial research focused primarily on contact stiffness and damping estimation for the single point contact case. Erickson [19] implemented two parameter estimation methods – the *indirect adaptive* and the *recursive least squares* – and adapted them to the contact parameter estimation problem. These algorithms were implemented in simulation and then evaluated experimentally

using a planar robotics test-bed at the University of Victoria [19, 21]. Figure 1-1 shows the robot end-effector contact interface (environment) from these experiments, with stiffness and damping parameters of 4800 N/m and 200 kg/s, respectively. The estimation methods employed in Erickson's research were based on the original work by Seraji and Colbaugh [18] and Love and Book [20], respectively. Small modifications to these methods were necessary for successful implementation. Regardless, these methods were based on a one-point contact model between the manipulator payload and the environment, requiring the measured contact force and displacement at the point of contact. The methods developed by Erickson processed the data in time domain.

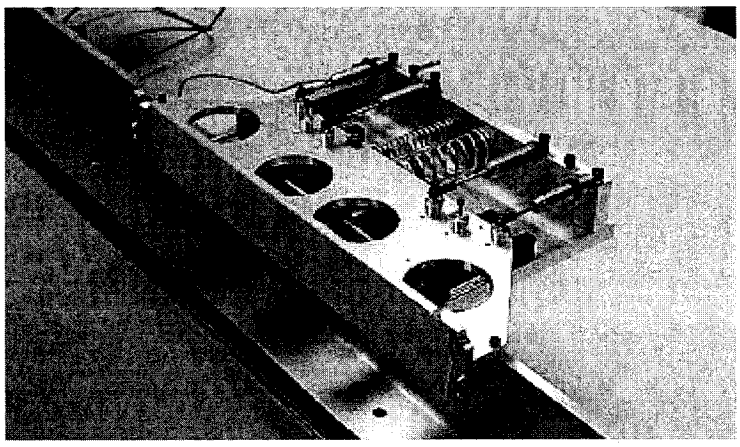

Figure 1-1 University of Victoria planar robotics test-bed contact interface

Weber [22] expanded on the original work by Erickson [19]. After major upgrades to the planar robotics test-bed facility at the University of Victoria, Weber implemented five *offline*, time-domain based, contact parameter estimation algorithms, also for the single point contact model. Experiments with the upgraded test-bed were used to validate Weber's identification algorithms.

Erickson [19] and Weber [22] concluded that the identification of contact stiffness was feasible provided that the normal force and corresponding displacement at the contact point could be accurately measured. However, they determined that accurate estimation of contact damping was unlikely without the use of special (persistently exciting) maneuvers. It was noted, however, that some estimation of contact damping was possible during the transient response at the initial and final phases of contact, given that the convergence rate of the algorithm was sufficiently fast [19, 21, 22].

Patel [23] continued work on the parameter estimation problem for simple contacting geometries by exploring estimation algorithms that process data in the frequency domain. Patel developed four offline, frequency-domain identification strategies capable of estimating contact stiffness and damping parameters. The validation of Patel's algorithms was completed using the experimental data from Weber's [22] planar robotic test-bed experiments at the University of Victoria.

Patel [23] compared the performance of Weber's [22] time-domain contact parameter estimation algorithms with the frequency-domain estimation algorithms. It was concluded that the success of the stiffness estimation results was similar for both the time-domain and frequency-domain identification algorithms. Patel further noted that the time-domain methods developed by Weber [22] gave more accurate damping estimates than the frequency-domain methods when the maneuvers were persistently excited, but both sets of methods performed similarly for unexcited trajectories. The nature of Patel's frequency-domain algorithms required that the main frequencies of the system be identified manually. Patel concluded that the inability to identify all the frequencies of interest resulted in the observed overall poor damping estimation.

1.4.2 Multiple Point Contact Parameter Estimation

The investigations of Erickson [19], Weber [22] and Patel [23] showed that successful identification of contact stiffness and damping for the simple contacting geometry scenario was possible, provided that accurate measurements of the dynamics were available. This is generally not a problem for robotic contact tasks that involve a single point of contact, as the robot's end-effector sensors can sense the required contact force and displacement. It is more realistic, however, to expect that practical constrained robotic tasks would involve complex payload and environment geometries, implying complex contact situations whereby contact occurs simultaneously at multiple points. The process of obtaining the required dynamic information for multiple point contact parameter estimation is significantly more complex than what is required for the single point problem. Sharf et al. [24] proposed an algorithm to isolate the single point contact phases, which possibly exist at the beginning of contact between bodies, by using the

force sensor data from the robot end-effector. The work in [24] thus allowed for the use of the identification methods for single point contact problems for contact between complex payload and environment geometries. The resulting methodology described in [24], was applied successfully to identify contact friction for the Integrated External Assembly (IEA) battery mating operation.

Weber [22] and Weber et al. [25] used a multiple point contact parameter estimation algorithm to directly identify contact stiffness, damping and friction for complex payload and environment geometries. The method employed in [22, 25] considers simultaneous contact at multiple points, as what would be realistically expected in practical robotic tasks. In the estimation method, contact stiffness, damping and coefficient of friction parameters are assumed identical at each contact point. Weber was able to obtain accurate stiffness estimation results, but results for damping and friction were poor. Weber also concluded that the identification algorithm for the multiple contact point problem demonstrated sensitivity to noisy position and force data.

Patel [23] continued the multiple point contact parameter estimation research by Weber [22] and Weber et al. [25] and was able to successfully resolve the issue of poor friction estimation by modifying the friction model settings in the simulation software to better match the friction model assumed in the identification algorithm. Patel [23] proceeded to investigate the performance of the multiple point contact parameter estimation algorithm in the presence of noise. The estimation results were sensitive to measurement noise, but Patel concluded that with filtering, dramatic improvements in contact stiffness and damping estimation could be realized. Patel found no improvements in the contact friction estimation after filtering the noisy data. Patel concluded that the identification algorithm for the multiple point contact scenario was successfully validated with the simulated test case.

1.5 Thesis Objectives

In previous research on the single point contact parameter estimation problem by Weber [22], five time-domain algorithms - recursive least squares, instantaneous least squares,

indirect adaptive, Kalman filter and global least squares - were applied to a simple geometry robotic contact experiment. The experiment involved parameter estimation of a relatively soft environment, of known stiffness and damping. Four frequency-domain parameter estimation algorithms were applied to the same experiment in research by Patel [23]. One aim of the work described in this thesis is to consolidate all of these estimation algorithms into a user-friendly software package. The software package is intended to allow the user to extend algorithm use to any single point contact experiment with ease. Another aim of this research is to validate and use the algorithms with practical experiments with much stiffer environments and payloads than those used in the experiments by Weber [22]. In particular, we attempt to estimate payload contact parameters from new, and existing [41], experiments conducted with the STVF facility. This research also aims to determine the capabilities and limitations of the STVF manipulator test-bed for contact parameter estimation research.

The second main objective of this research is to explore time-domain contact parameter estimation for realistic multiple point contact experiments. The multiple point contact parameter estimation algorithm was previously validated with simulations [23], but not experimentally. Thus, this thesis aims to apply the identification algorithm to practical STVF multiple point contact experiments. As part of this process, a user-friendly software package incorporating the multiple point contact parameter identification algorithm is developed, complementing the single point parameter estimation software package. In addition, an assessment of the sensitivity of the multiple point identification algorithm to mismatches between the payload geometric model and the physical unit is conducted. Finally, this research is also aimed to add to and support the ongoing contact dynamics research at the Canadian Space Agency.

1.6 Thesis Organization

Chapter 1 included an introduction on robotic constrained motion, with an emphasis on space robotic contact tasks. A background discussion on the parameter estimation problem was presented, followed by the motivation and objective for this thesis.

Chapter 2 presents the development of a Matlab-based, user-friendly software toolbox containing nine parameter estimation algorithms for the single point contact parameter estimation problem. The estimation algorithms, which are both time- and frequency-domain based methods, are briefly described. The implementation and integration of the algorithms in the form of a toolbox is discussed and screen shots of the final product are presented.

Chapter 3 presents details about the STVF manipulator test-bed experimental facility, followed by toolbox estimation results for a series of STVF contact experiments with simple geometry payloads. Results are given for each of the nine estimation algorithms in the toolbox. This is followed by a presentation of using independent experiments to determine the stiffness of the STVF test-bed (without a payload) and the stiffness of the payloads alone. These results are used in conjunction with the STVF payload experiment results to show the feasibility of estimating payload stiffness using only STVF test-bed experiments. The limitations of single point contact parameter estimation using the STVF manipulator test-bed are discussed.

Chapter 4 presents the Multiple Point Contact Parameter Estimation Toolbox. The model and the contact parameter identification algorithm for complex contacting geometries is given, which addresses the issue of contact occurring at multiple points simultaneously. This is followed by an exposition of the integration of the identification algorithm into a user-friendly, Matlab-based software toolbox. Screenshots of the final product are given.

Chapter 5 presents contact parameter estimation results for multiple point contact experiments using the STVF test-bed. In these experiments the payload is an Orbital Replacement Unit (ORU) that is inserted into a receptacle. Further attention is given to a sensitivity analysis of the identification algorithm using a simulated gravity drop experiment. The sensitivity analysis investigates model geometry sensitivity.

Chapter 6 presents conclusions and recommendations for future research.

Chapter 2

Single Point Contact Parameter Estimation Toolbox

In this chapter, the development of the Single Point Contact Parameter Estimation Toolbox is described. This toolbox was developed with several goals in mind. The first goal of the toolbox was to incorporate nine unique single point contact parameter estimation algorithms in one software package that could be easily integrated with existing modelling software at CSA. Secondly, the toolbox was to provide a user-friendly graphical user interface (GUI), complete with help documentation, for using the algorithms. Finally, the toolbox was required to be capable of estimating contact parameters for experiments having various input data file formats. Specifically, the toolbox needed to be able to automatically process experimental data from contact experiments conducted at CSA with the STVF manipulator mentioned in Chapter 1. A detailed description of the STVF manipulator and the single point contact experiments carried out are provided in Chapter 3.

The development of the *Single Point Contact Parameter Estimation Toolbox* will be discussed in several stages. For brevity, in this thesis we will refer to this toolbox as the *Single Point Toolbox*. The first section of this chapter will describe the environment contact model upon which the nine estimation algorithms are based. The subsequent section will provide brief descriptions of each of the nine estimation algorithms. The final section discusses the implementation and integration of the toolbox.

2.1 Environment Model

The toolbox described in this chapter makes several assumptions about the nature of the contact event. Primarily, the contacting bodies (i.e. the robot end-effector and the environment) are assumed to be of simple geometry, whereby the ensuing contact events have only one contact point. Furthermore, it is assumed that the robot end-effector motion is restricted to the direction normal to the environment, as shown in Figure 2-1. Under these assumptions, the friction force is omitted from the analysis. A commonly used normal contact force (F_n) model is the spring-dashpot model, also known as a first-order impedance model. This model of the environment is illustrated in Figure 2-1 and described mathematically by:

$$F_n = kx + b\dot{x} \tag{2.1}$$

where k is the contact stiffness, b is the contact damping, x is the deformation at the contact point and $\dot{x}$ is the deformation rate [25]. Accordingly, the contact parameter identification problem is to identify the values of k and b from measured F_n, x and possibly $\dot{x}$.

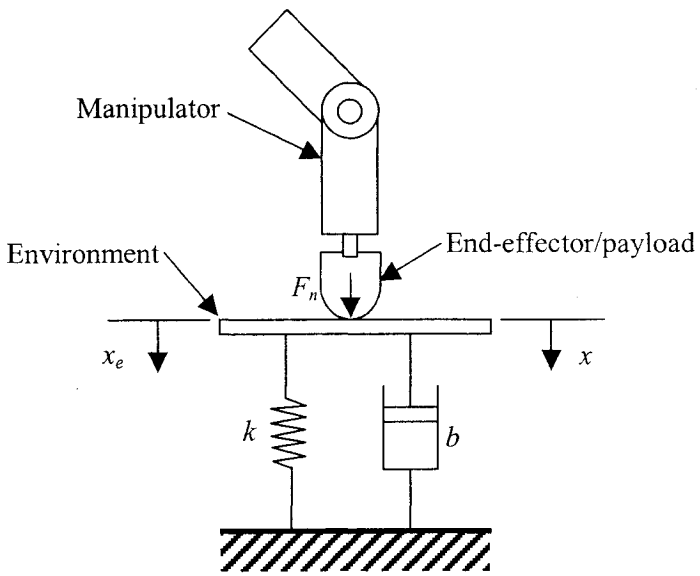

Figure 2-1 Single point contact environment model

2.2 Identification Algorithms

Of the nine estimation algorithms incorporated in the toolbox, five process the contact data in the time domain. They are the Recursive Least Squares (RLS) algorithm, the

Instantaneous Least Squares (ILS) algorithm, the Indirect Adaptive (IA) algorithm, the Kalman Filter algorithm and the Global Least Squares (GLS) algorithm. The RLS and IA algorithms were first developed by Erickson [19] as *online* estimation methods. Weber [22] implemented the RLS and IA methods as *offline* methods. Weber [22] also applied the ILS, Kalman Filter and GLS methods for offline contact parameter estimation. The four remaining algorithms in the toolbox process the data in the frequency domain. They are the Empirical Transfer Function Estimator (ETFE), the Equation Error Method (EEM), the Output Error Method (OEM) and the Generalized Maximum Likelihood Estimator (GMLE). These algorithms were originally applied to the contact parameter estimation problem in [23]. The frequency domain algorithms can be applied to a linear identification problem only, as is the case here (equation 2.1). The following sections provide a brief description of the theory behind the nine algorithms included in the toolbox and discuss what information is required to be specified by the user. The algorithms as presented here are designed for offline contact parameter estimation.

2.2.1 Time Domain Algorithms

Recursive Least Squares Algorithm

A detailed description of this algorithm can be found in [19, 22]. The method was based on the original work by Love and Book [20]. In this method, the parameter estimation problem is formulated in standard linear regression form:

$$Y = \phi^T \theta \tag{2.2}$$

where θ is a function of the contact parameters to be estimated, Y contains the normal force data and ϕ is a function of the environment displacement. The recursive least squares solution to (2.2), and hence the parameter estimation, is then carried out using the following matrix inversion lemma [26]:

$$\theta_{[k]} = \theta_{[k-1]} + L_{[k]}\left(Y_{[k]} - \phi_{[k]}^T \theta_{[k-1]}\right) \tag{2.3}$$

where

$$L_{[k]} = \frac{P_{[k-1]}\phi_{[k]}}{\lambda + \phi_{[k]}^T P_{[k-1]}\phi_{[k]}} \tag{2.4}$$

and

$$P_{[k]} = \frac{1}{\lambda}\left(P_{[k-1]} - \frac{P_{[k-1]}\phi_{[k]}\phi_{[k]}^T P_{[k-1]}}{\lambda + \phi_{[k]}^T P_{[k-1]}\phi_{[k]}} \right) \tag{2.5}$$

The values of λ and P_0 are chosen by the user with $0 \leq \lambda \leq 1$ (typical values are $0.95 \leq \lambda \leq 0.99$ [19]). The matrix P_0 is of the form aI where a is a scalar value, usually on the order of 10^5 or 10^6, specified by the toolbox user and I is the identity matrix [19]. It should be noted that in addition to environment stiffness and damping, the RLS algorithm also provides estimation of the environment mass. The user is required to specify initial guesses for the contact stiffness, damping and mass. An advantage of this algorithm is that only the contact force and contact displacement are needed for estimation. The velocity and acceleration are calculated internally by the finite difference technique.

Instantaneous Least Squares Algorithm

The ILS algorithm is based on the RLS algorithm, but uses velocity data for parameter estimation, along with measurements of contact force and contact point deflection. The ILS method is described in detail in [22]. This method assumes that the environment mass and acceleration are negligible during contact, and hence provides estimates only for the contact stiffness and damping. The velocity data can be measured directly or computed indirectly with the finite difference of the deflection data. The force, deflection and velocity information are used to determine the parameter estimates at every time instant using the recursive least squares technique of equation (2.3). With the exception of an initial guess for the environment mass, the user is required to provide the same algorithm input information necessary for the RLS routine.

Indirect Adaptive Algorithm

The theory describing this algorithm is explained in detail in [19, 22]. The original work derives from research done in [18]. The IA algorithm formulates the parameter estimation problem in standard linear regression form and uses the estimated contact force, calculated from the estimates for the environment stiffness and damping:

$$\hat{F}_n = \phi^T \hat{\theta} \tag{2.6}$$

where the vector $\hat{\theta}$ combines the estimates of contact stiffness and damping. Then, the parameter adaptation (update) law is defined by [28]:

$$\dot{\hat{\theta}} = -\Gamma^{-1}\phi\tilde{F}_n \tag{2.7}$$

where Γ is a positive definite gain matrix, $\tilde{F}_n = \hat{F}_n - F_{meas}$ and F_{meas} is the measured contact force. Slotine and Li [27] showed that the convergence of the parameters was guaranteed with the adaptation law of equation (2.7). The toolbox user supplies initial guesses for the contact stiffness and damping and specifies the gain matrix Γ.

Kalman Filter Algorithm

For a complete description of the offline Kalman Filter estimation routine briefly summarized here, refer to [22]. The Kalman filter is a popular method for determining the state vector in a state-space representation of a linear system where there are noisy inputs and outputs. Additional information on Kalman filtering can be found in [28, 29].

The Kalman filter finds a solution for stochastic linear systems of the following form:

$$\begin{aligned} x_{[k+1]} &= Gx_{[k]} + w_{[k]} \\ z_{[k]} &= Hx_{[k]} + v_{[k]} \end{aligned} \tag{2.8}$$

where x is the state vector, z is the system output, G is the state transition matrix, H relates the system inputs and outputs, w is the state estimate noise, and v is the output measurement noise. The Kalman Filter algorithm implemented in the Single Point Toolbox uses measurements of displacement, velocity and force at the contact point and defines the state vector x as:

$$x = \begin{bmatrix} k & b \end{bmatrix} \tag{2.9}$$

If the states are time invariant (which is assumed to be the case for stiffness and damping), the state transition matrix G is the identity matrix and state error can be neglected ($w = 0$). The vector H contains the displacement and velocity inputs, while the system output z represents the contact load.

A series of four main steps are recursively executed in the Kalman filtering procedure to generate estimates for the state vector x after each time step. The recursive update steps

rely on matrices containing stochastic information about the system. The details of these steps are described in [22]. The user is required to specify an initial guess for the contact stiffness and damping, as well as the prediction error covariance matrix P. The matrix P is used in the four recursive steps in the Kalman filtering procedure and is of the form aI where a is a scalar value and I is the identity matrix.

Global Least Squares Algorithm

The Global Least Squares (GLS) Algorithm uses all the information that was acquired during the time of contact with the environment to produce a single estimate for the contact parameters (as opposed to a time history of estimates). Complete details about this algorithm can be found in [22].

In the GLS routine, the force, displacement and velocity data from each time step are combined to form an overdetermined system of equations of the form:

$$\mathrm{Y} = \Phi^T \hat{\theta} \tag{2.10}$$

where the parameter estimates $\hat{\theta}$ are determined using a standard least squares solution:

$$\hat{\theta} = \left(\Phi\Phi^T\right)^{-1} \Phi\mathrm{Y} \tag{2.11}$$

This algorithm is straightforward and is also a good option if the previously discussed algorithms are unable to converge during the time of contact, or if one wishes to obtain a single answer for parameter estimates.

2.2.2 Frequency Domain Algorithms

Empirical Transfer Function Estimate Algorithm

This method determines the transfer function of the linear system using the input and output data in the frequency domain [26, 30]. It determines the level of magnification (gain M) and phase-shift ϕ of the output with respect to the input [30]. The theoretical model of the transfer function contains expressions for the parameters to be estimated. The estimated value of the transfer function is compared with the theoretical model of the transfer function, which allows the contact parameters to be identified.

To employ this method for contact parameter identification, we rewrite the contact force model in the frequency domain:

$$F(j\omega_i) = (bj\omega_i + k)X(j\omega_i) \tag{2.12}$$

where $F(j\omega_i)$ and $X(j\omega_i)$ are the discrete Fourier transforms of the force and displacement, respectively. In this linear system, the contact force, F, is considered the input and the displacement, X, is the output and hence the transfer function of the system at frequency ω_i, is:

$$G(j\omega_i) = \frac{X(j\omega_i)}{F(j\omega_i)} = \frac{1}{bj\omega_i + k} \tag{2.13}$$

The transfer function can be described by the gain M and the phase shift ϕ, which are estimated from the measured force and displacement data, and according to (2.13) are both functions of the contact stiffness and damping. The parameter estimates are then calculated by solving for k and b from the equations for M and ϕ. More detailed information regarding the implementation of this contact parameter estimation algorithm can be found in [23]. In the context of the toolbox, the user is required to specify the frequencies of interest; that is to say, a discrete set of frequencies that he/she determines are involved in the signal based on an analysis of the frequency spectrum of the input and output signals. The toolbox includes this step as part of the procedure that the user must comply to when processing data with the frequency domain algorithms.

Output Error Method

The Output Error Method (OEM) is a popular technique for parameter estimation of linear dynamic systems, as noted in [1, 31, 32]. The OEM is a 'model reference' iterative procedure [33] where the goal is to minimize the error between the measured and modelled output that is produced from identical inputs.

The contact parameter estimation problem is formulated as a model reference problem for i=1,2,...,m, where m is the number of frequencies of interest in the system:

$$\begin{aligned} F(j\omega_i, \theta) &= (bj\omega_i + k)X(j\omega_i) \\ Z(j\omega_i) &= F(j\omega_i, \theta) + V(j\omega_i) \end{aligned} \tag{2.14}$$

In this system, F is the modelled output force, X is the measured input displacement, Z is the measured force, V is the (assumed) Gaussian force measurement noise (with zero mean and covariance R), and θ contains contact parameter estimates as before. To estimate the parameters, the following cost function is minimized:

$$J = \frac{1}{2}\sum_{i=1}^{m}[Z(j\omega_i) - F(j\omega_i,\theta)]^* R^{-1}[Z(j\omega_i) - F(j\omega_i,\theta)] \tag{2.15}$$

A Newton-Raphson technique is used for estimation. The iterative routine executes until the minimum of the cost function is found. The new parameter estimates after each iteration are found by:

$$\hat{\theta} = \theta_{previous} + \Delta\hat{\theta} \tag{2.16}$$

where

$$\Delta\hat{\theta} = \left[\mathrm{Re}\left(\sum_{i=1}^{m} h^*(j\omega_i,\theta)R^{-1}h(j\omega_i)\right)\right]^{-1} \times \left[\mathrm{Re}\left(\sum_{i=1}^{m} h^*(j\omega_i,\theta)R^{-1}V(j\omega_i)\right)\right] \tag{2.17}$$

In this equation, the term h^* is the complex conjugate transpose of h. The term h refers to the *ith* row of sensitivity matrix H and can be expressed as [23]:

$$h(j\omega_i,\theta) = [1 \quad j\omega_i]X(j\omega_i) \tag{2.18}$$

The routine is stopped either when $\Delta\hat{\theta}$ (the change in the parameter values) reaches a specified tolerance or when the maximum number of iterations have been performed. In the toolbox, the user is required to specify the frequencies of interest, initial values for the contact parameter estimates, the maximum number of iterations and the tolerance on $\Delta\hat{\theta}$.

Equation Error Method

The Equation Error Method (EEM) is a simple, non-iterative procedure for parameter estimation. It is based on the principle of least squares and the estimates are found by minimizing the error in the (state) equation [31, 34]. Complete details on the implementation of this method as a contact parameter estimation routine are in [23].

The frequency domain model of the contact force problem (equation 2.12) is rewritten as:

$$j\omega_i X(j\omega_i) = -\frac{k}{b}X(j\omega_i) + \frac{1}{b}F(j\omega_i) \tag{2.19}$$

Thus, the error equation for the above state equation is:

$$\varepsilon(j\omega_i) = j\omega_i \tilde{X}(j\omega_i) + \frac{k}{b}\tilde{X}(j\omega_i) - \frac{1}{b}\tilde{F}(j\omega_i) \tag{2.20}$$

where $\tilde{X}$ and $\tilde{F}$ are the *measured* displacement and force, respectively. The system can be formulated as a least-squares regression problem:

$$y = x\theta + \varepsilon \tag{2.21}$$

where ε is given by equation (2.20), θ is a function of the parameter estimates, x is a matrix containing $\tilde{X}$ and $\tilde{F}$ data and y is a vector containing $j\omega_i \tilde{X}(j\omega_i)$ data.

From [35] the least squares cost function is shown to be:

$$J = \frac{1}{2}(y - x\theta)^* \cdot (y - x\theta) \tag{2.22}$$

the minimizing solution to which is given by [36]:

$$\hat{\theta} = \left[\mathrm{Re}(x^* x)\right]^{-1} \mathrm{Re}(x^* y) \tag{2.23}$$

In terms of the Single Point Toolbox, the user is only required to specify the frequencies of interest. The user does not have to specify an initial guess for the contact parameters.

Generalized Maximum Likelihood Method Algorithm

The general idea behind Generalized Maximum Likelihood Method (GMLM) is to obtain estimates for the parameters that best describe the given data [23, 36, 37]. The GMLM uses the same formulation as the EEM method, equation (2.19).

For this method, the force measurements are assumed to be free of noise, while the displacement measurements are subjected to noise V, with a mean of zero and covariance R. The measured displacement, Z, is therefore:

$$Z(j\omega_i) = X(j\omega_i) + V(j\omega_i) \tag{2.24}$$

From [36, 37], the log-likelihood function is presented as:

$$L(\theta) = -\frac{N\Delta t}{2}\mathrm{Re}\sum_{i=1}^{N} V^*(j\omega_i)R^{-1}V(j\omega_i) - \frac{N}{2}\log|R| \tag{2.25}$$

where N is the total number of frequency samples and Δt is the time step size between samples. Minimizing equation (2.25) with respect to covariance, R, gives:

$$\hat{R} = \Delta t\sum_{i=1}^{N} V(j\omega_i)V^*(j\omega_i) \tag{2.26}$$

The estimation routine starts with initial guesses for the parameters and iterates until the likelihood function minimum is reached. The new parameter estimates obtained after each iteration are determined through the following expression [36]:

$$\hat{\theta} = \theta_{previous} - M^{-1}g \tag{2.26}$$

where M and g are functions of the contact parameter estimates, $\theta_{previous}$, the contact force, as well as $\hat{R}$, N, Z and Δt. The full expressions for M and g are found in [23, 37].

As with the other frequency domain estimation routines, the estimates can be found using only the m frequencies of interest. In the context of the Single Point Toolbox, the user must specify initial guesses for the parameters, the frequencies of interest, the maximum number of iterations and the tolerance on $\Delta\hat{\theta}$.

2.3 Single Point Toolbox Implementation and Integration

The original algorithms described in Section 2.2 were programmed in Matlab and were hard-coded to work optimally for one specific set of contact experiments conducted at the University of Victoria [19, 22, 23]. These original algorithms were modified in order to interface with the GUI and work for the general case. For ease of use and compatibility with the modelling environment at CSA, the Single Point Toolbox was also developed in Matlab.

2.3.1 Toolbox Implementation

The toolbox was developed in the Matlab 6 Release 13 environment. Matlab is equipped with a GUI Design Environment (GUIDE) where a set of tools is available to create a GUI to run Matlab scripts. A GUI consists of a *.fig* file, which includes layout

information and properties of the GUI's appearance, and an *.m* file, which contains the behaviour control code of the GUI features. The GUI features can include, but are not limited to, push buttons, radio buttons, check boxes, axes, edit fields, text fields and drop down menus.

One major benefit of creating a GUI for these estimation algorithms is that the algorithm details are encapsulated from the user. In addition, the user does not necessarily have to be familiar with the programming language in order to run experimental data through the algorithms. The user must merely possess a general understanding of what input data and algorithm parameters he/she must modify and how to modify them.

2.3.2 Toolbox Architecture and Functionality

The general program architecture is shown in Figure 2-2. When using the toolbox, the user is first presented with a main menu screen (Figure 2-3), which lists all possible options. Based on the user's selection on the main menu, the toolbox diverts to a different screen or segment of the program. The toolbox offers the time domain and the frequency domain estimation algorithms in separate modules and hence the user is limited to working with one domain at a time. All parameters required for use in the algorithms can be modified directly on the GUI. Screen shots of the toolbox main menu and of the time domain GUI are shown in Figure 2-3 and Figure 2-4.

In building the toolbox, options were included to allow for the use of a generic file format. In addition, the goal of designing the toolbox to specifically process STVF experimental data, which requires some additional processing steps, was met. In Chapter 3, a detailed discussion of the single point STVF contact experiments is given, where the processing issues, which had to be addressed within the toolbox, will become evident.

The toolbox comes complete with documentation, which is integrated in the standard Matlab *Help* environment, as shown in the screen shot in Figure 2-5. The documentation includes a description of all GUI features and algorithms, as well as detailed demos. The toolbox also provides graphical output following an estimation routine, as shown in

Figures 2-6 (a) and (b). Additionally, the toolbox has been programmed with error checking features. For example, the toolbox notifies the user with a pop-up error message when an invalid input is encountered.

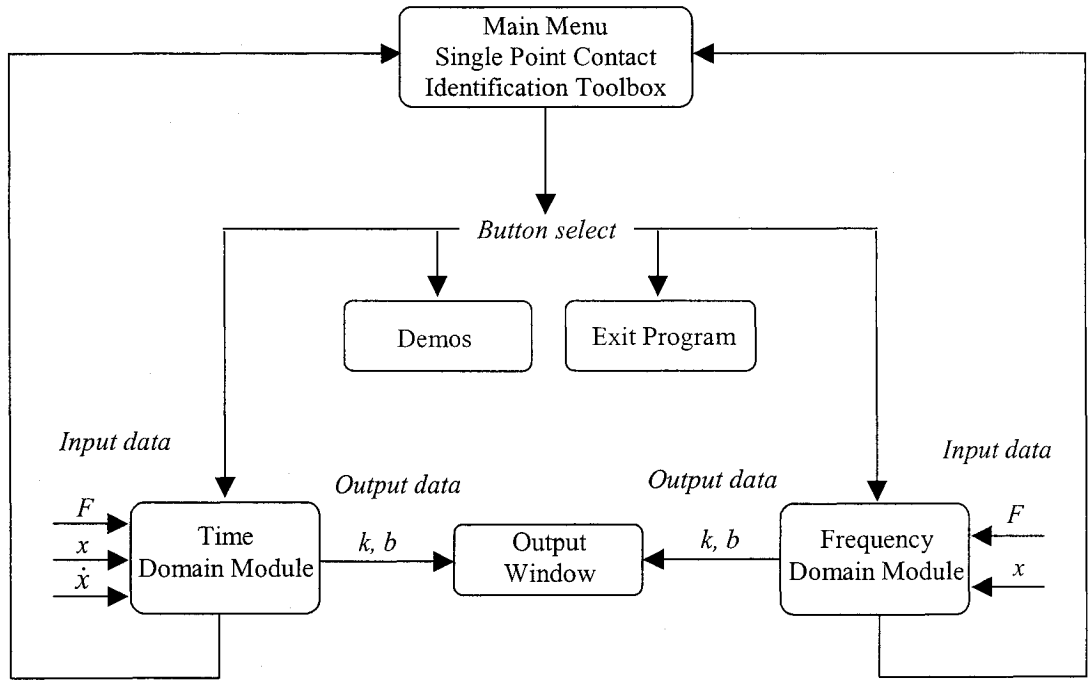

Figure 2-2 General program architecture

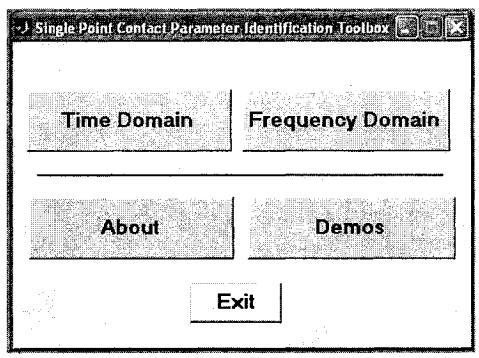

Figure 2-3 Single point contact parameter estimation toolbox main menu

As mentioned previously, the toolbox is inherently limited to *offline* contact parameter estimation. Some of the toolbox algorithms can potentially be modified to allow for *online* estimation, though the modifications to the toolbox to enable online estimation would be significant.

The Single Point Toolbox was integrated in CSA's SMT modelling environment, which is largely based in Simulink, a component of Matlab. A Simulink block was created whereby the user can access the toolbox directly from Simulink.

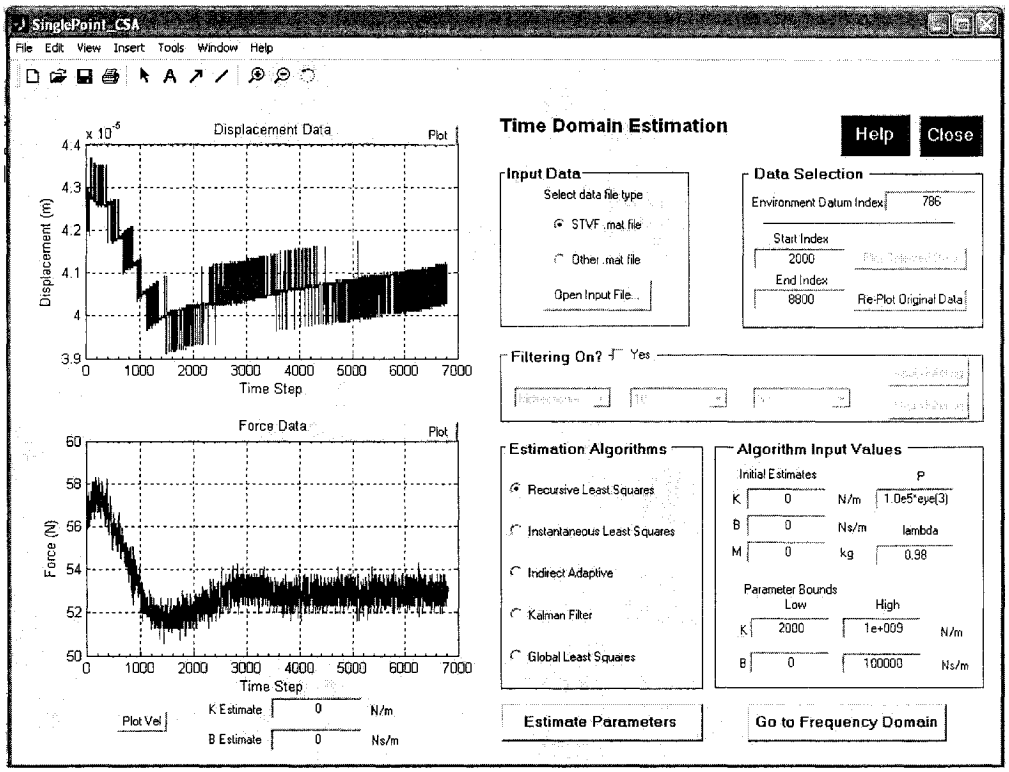

Figure 2-4 Single point contact parameter estimation toolbox time domain module

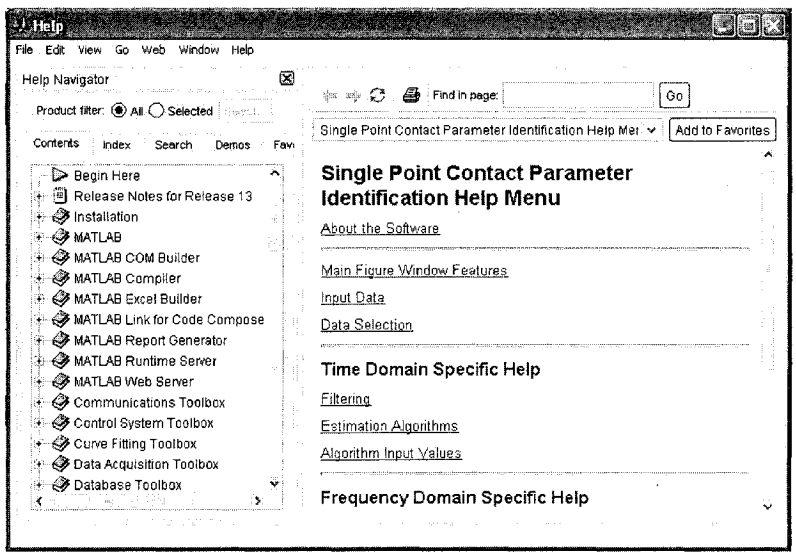

Figure 2-5 Screen shot of toolbox help documentation

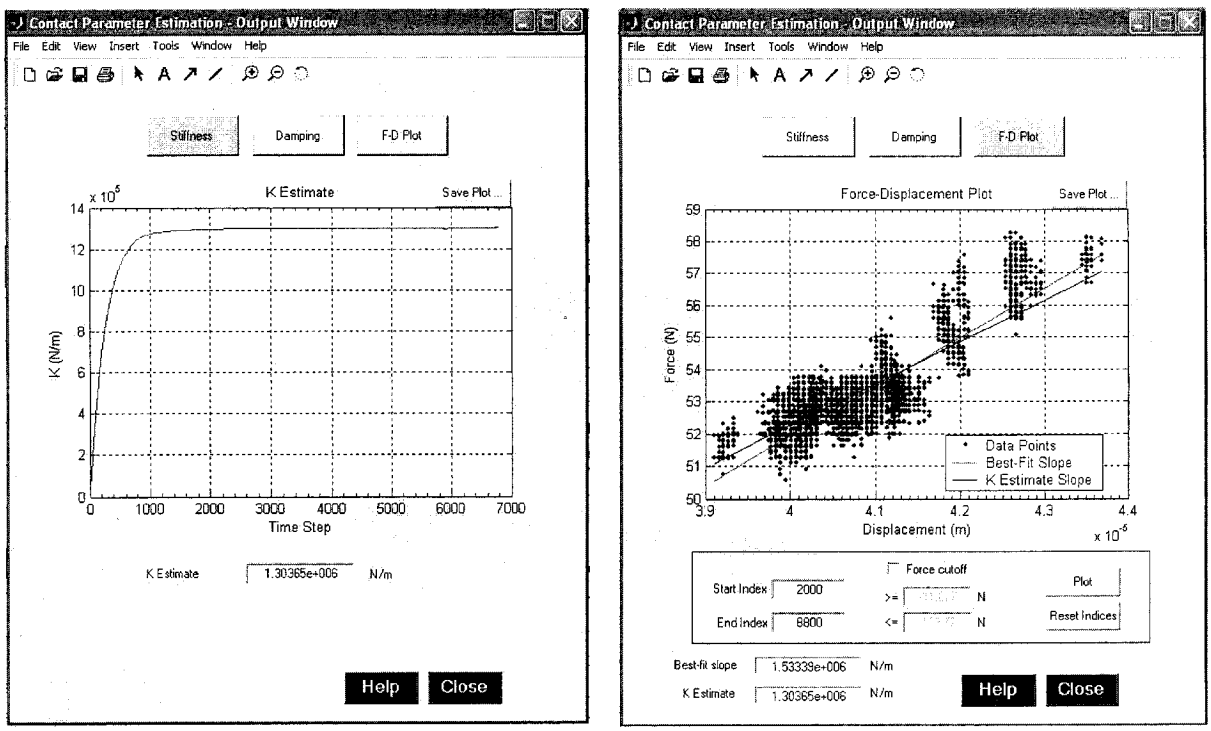

(a) (b)

Figure 2-6 Screen shots of toolbox output windows: stiffness estimate convergence plot (a) and linear best-fit estimation (b)

Chapter 3

Contact Parameter Estimation of Simple Geometry Payloads using the STVF Manipulator Test-bed

In Chapter 2, the development of a single point contact parameter estimation toolbox was presented. The Single Point Toolbox, created in the Matlab programming environment, incorporates nine different contact parameter estimation routines. One goal of the Single Point Toolbox was to provide a tool capable of processing measured data from experiments carried out with the STVF manipulator test-bed at CSA. The use of the Single Point Toolbox in this capacity is realized in this chapter.

There are several focuses in this chapter. First, we aim to use the Single Point Toolbox successfully in processing STVF contact experiment results. In this aspect, the performance and consistency of the estimation algorithms in the toolbox will be assessed using STVF contact experiments with relatively stiff payloads. Second, the work presented in this chapter aims to demonstrate the feasibility of estimating *payload* stiffness solely using STVF manipulator test-bed experiments.

The chapter begins by discussing the STVF experimental test-bed facility in detail (Section 3.1). This is followed by the description of the main contact experiments carried out with the STVF and the payloads used. Subsequently, the details of the system under contact parameter estimation are clarified (Section 3.2), where elements that are discussed further in later sections are introduced. The following sections (3.3 - 3.5)

present and discuss the estimation results for each component of the system. Finally, a brief attempt at quantifying some of the errors in the estimation process is given (Section 3.6).

3.1 Experimental Test Facility

As mentioned in Chapter 1, the Canadian contribution to the International Space Station (ISS) is the Mobile Servicing System (MSS). Part of the MSS includes the Special Purpose Dexterous Manipulator (SPDM). As previously discussed, the SPDM is designed to perform maintenance tasks on the ISS, which typically consist of on-orbit replacement of Orbital Replacement Units (ORU) on the ISS.

The level of risk and high costs associated with the types of space-based robotic operations as those envisioned for the SPDM makes on-earth verification of these orbital tasks highly valuable. Canada is responsible for the verification of the SPDM operations and for this purpose the SPDM Task Verification Facility (STVF) was developed by CSA. The dynamics of the SPDM end-effector is emulated with the STVF Manipulator Test-bed (SMT), which is part of a hardware-in-the-loop simulation that mimics SPDM operations.

3.1.1 STVF Manipulator Test-bed

The STVF manipulator (Figure 3-1) is a very stiff, six degree-of-freedom serial robot, with a backhoe configuration. The base shaft, upper arm and forearm structural components of the robot are constructed from steel. The components in the wrist are made from aluminum. Each of the six manipulator joints include hydraulic actuators, position and velocity sensors, load sensors and an accelerometer. The 23 bit optical joint encoders were chosen to provide the required end-effector resolution of 0.5 mm and 0.05 degrees at the edge of the workspace, and a velocity sensing requirement of 1 mm/s and 0.1 deg/s. The STVF robot was designed to handle payloads up to 100 kg. The current SMT robot control scheme guarantees a relative position accuracy of 0.2 mm.

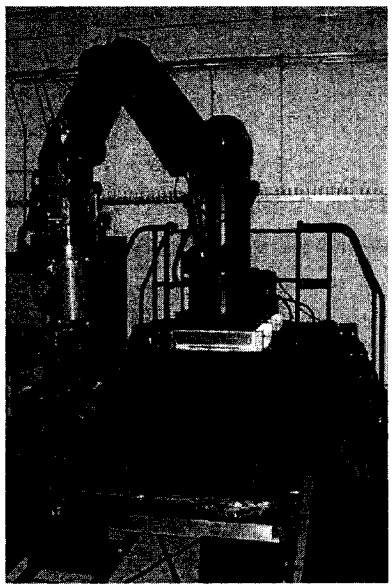

Figure 3-1 SPDM Task Verification Facility (STVF)

(Photograph © Canadian Space Agency)

The end-effector assembly consists of a 6-axis force/torque sensor, a gripper and an ORU Tool Change-Out Mechanism Emulator, which fits between the sensor and the gripper. The gripper has a 909 N (2000 lb) closing force. A micro-fixture interface was designed to match the 'fingers' of the gripper. The micro-fixture is bolted to the payloads and provides the means by which the STVF can manipulate them (Figure 3-2).

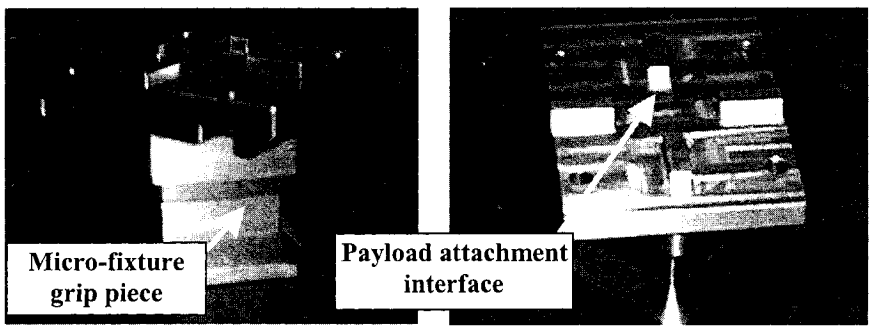

(a) **(b)**

Figure 3-2 Micro-fixture interface

In this thesis, the term *SMT* refers to the combination of the STVF manipulator assembly and the worksite force plate. The worksite force plate measures the contact forces and moments. The force plate was custom-built by Bertec Corporation, with a resolution of 0.5 N. The STVF robot has force/moment accommodation (FMA) motion control. The FMA control scheme allows for insertion tasks in Cartesian velocity control mode where

there is no risk of damaging the worksite. The maximum applied force is bounded by the FMA and proportional to the desired velocity. Further details are found in [11, 38 - 41].

3.2 STVF Contact Experiments

A series of quasi-static contact experiments with six different payloads was carried out using the SMT. As indicated earlier, the main goal of this chapter is to use these quasi-static experiments to estimate the contact parameters of simple geometry payloads, while making use of the Single Point Toolbox. In this section, the STVF experiment procedure is outlined, the payload specifications are described and the general overview of the contact system is presented. The discussion of the contact system in this section leads directly to the work presented in Sections 3.3 and 3.4.

3.2.1 STVF Experiment Conditions and Procedure

In the STVF experiments, an aluminum plate is mounted upon the worksite force plate to protect it from damage when contacted by the payloads. The supporting legs on the aluminum plate are 105 mm in height, with a diameter of 32 mm. The aluminum plate is 10 mm thick. During the contact experiments, the STVF end-effector brings the payloads, which are bolted to the micro-fixture interface, into contact with the aluminum plate, in the general proximity of one of the four supporting legs (Figure 3-3). The payload is brought into contact in the direction normal to the aluminum plate.

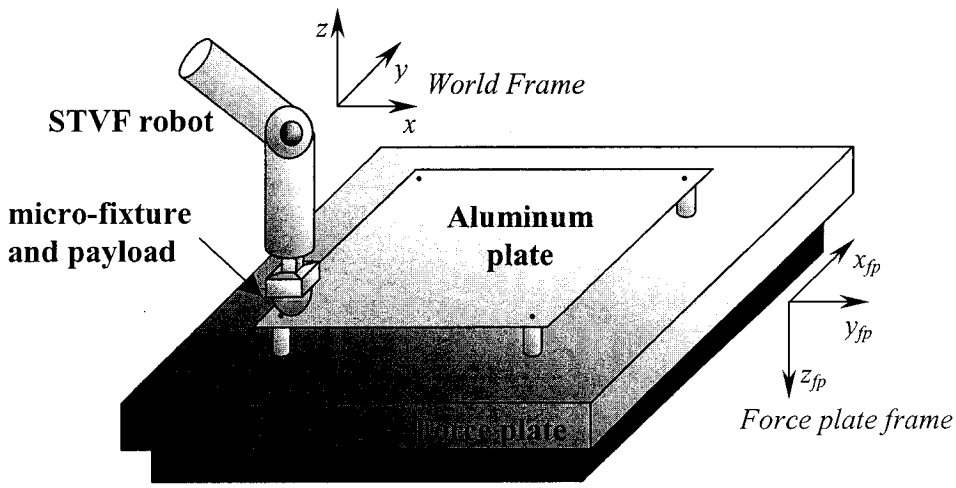

Figure 3-3 Single point contact experimental set-up with SMT

Following initial contact between the payload and aluminum plate, the experiments consisted of stepwise increments in the normal force, where each load level was held constant for several seconds. Under the FMA control scheme, stepwise increases of force plate loads are achieved by stepwise increases of the downward velocity (-z) of the end-effector. Reaction (normal) forces in the range of 50 to 400 N were recorded, with step sizes of roughly 50 N. This experiment was carried out twice for each payload.

3.2.2 Simple Geometry Payloads

In total, ten contact specimens were manufactured by the Canadian Space Agency for single point contact experiments. These specimens are the payloads referred to in Section 3.2.1 and subsequently in this chapter. The manufactured shapes include a cube, a triangular prism, a pyramid, a cone and a half-sphere, each constructed out of two different materials: Aluminum 6061 and Acetron GP Acetal, a general purpose plastic with a high strength and stiffness. The range of shapes manufactured allows for the study of the effects of having different contact geometries, such as an edge or a rounded tip.

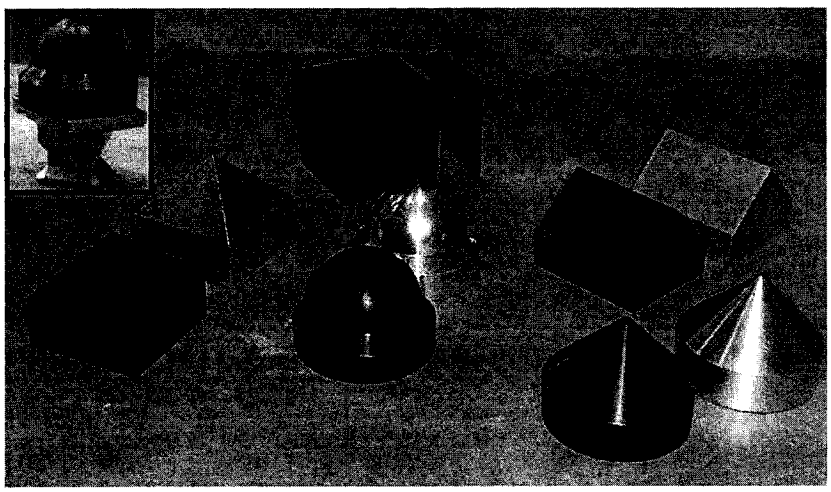

Figure 3-4 Simple geometry contact specimens (payloads)

Figure 3-4 shows the ten contact specimen payloads. To date, STVF experiments have been performed with all the plastic contact specimens but only the aluminum half-sphere. The inset image in Figure 3-4 depicts the plastic half-sphere specimen interfaced with the micro-fixture of Figure 3-2. Design documents of the payloads are in compiled Appendix A.

3.2.3 Contact Parameter Estimation System

As discussed in Chapter 2, the Single Point Toolbox accepts as inputs the displacement, velocity and load data required to solve the contact parameter estimation problem. With STVF experiments, the displacement and velocity data are provided in the form of end-effector position and velocity. These values are determined from rigid-body robot kinematics based on joint encoder readings, while the contact loads are acquired from the force plate. To estimate the contact parameters, displacement, not position, data is needed. To find the displacement, the end-effector position at the *instant* of contact is used as the reference datum. Subsequent end-effector position readings are then subtracted from this reference datum to determine the displacement of the end-effector (and the force plate) during contact. This data is used in the Single Point Toolbox to produce stiffness and damping estimates.

To understand the meaning of the contact stiffness estimates that are generated by the toolbox with the provided STVF experiment data, we need to consider what the end-effector position (and hence displacement) readings represent. Figure 3-5 shows a simplified, one-dimensional model of the SMT and payload system, where the stiffness of each component is represented by a spring and all springs are interconnected in series.

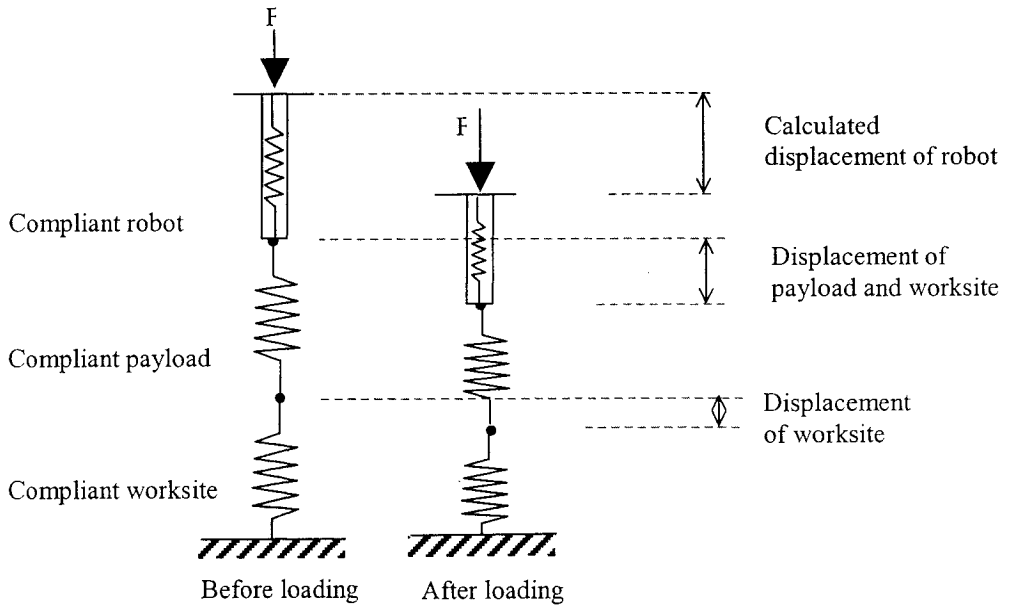

Figure 3-5 SMT test-bed and payload as a system of springs in series

Inspection of Figure 3-5 reveals that the calculated displacement of the robot end-effector, based on rigid-body kinematics, corresponds to the displacement of the *entire* system: the robotic facility and the payload. Thus, contact parameter estimates calculated by the toolbox with the robot end-effector displacement represent these of the combination of the SMT and the payload. In this thesis, we henceforth refer to "contact" parameters of each element of the described system by including a descriptive subscript. For example, $k_{SMT+payload}$, k_{SMT} and $k_{payload}$ represent the linear stiffness estimates of the combined SMT/payload system, the SMT alone and the payload, respectively.

The following subsection introduces the procedure for obtaining stiffness estimates for the combined SMT/payload system (i.e. $k_{SMT+payload}$) using the Single Point Toolbox. The estimation results follow directly. Section 3.3 covers the determination of the stiffness estimates for the SMT without a payload present. Section 3.4 presents a procedure for determining independent payload stiffness estimates. The results from Section 3.3 are used in combination with the Single Point Toolbox results (Section 3.2.5) to generate estimates for payload stiffness. The independent payload stiffness results from Section 3.4 are used to assess the success of this estimation.

3.2.4 Raw STVF Contact Experiment Data

In Figures 3-6 (a) and (b), a sample set of the output data from the STVF experiments is shown. The stepwise increase of the reaction (contact) force can be seen clearly in the force plot, Figure 3-6 (a). The inset portion of the end-effector position plot, Figure 3-6 (b), shows the corresponding stepwise changes in recorded end-effector position[1]. The nature of the data from these experiments provides a good opportunity to obtain contact stiffness estimates for the system. Additionally, close inspection of the plots surrounding the general time frame of initial contact indicates the presence of some transient data (Figure 3-7). During this time period, we might also expect some damping estimation to be possible, as suggested by the background research presented in Chapter 1.

[1] The positions shown here and in other plots in this chapter represent the z-coordinate of the end-effector position in the World Frame (Figure 3-3)

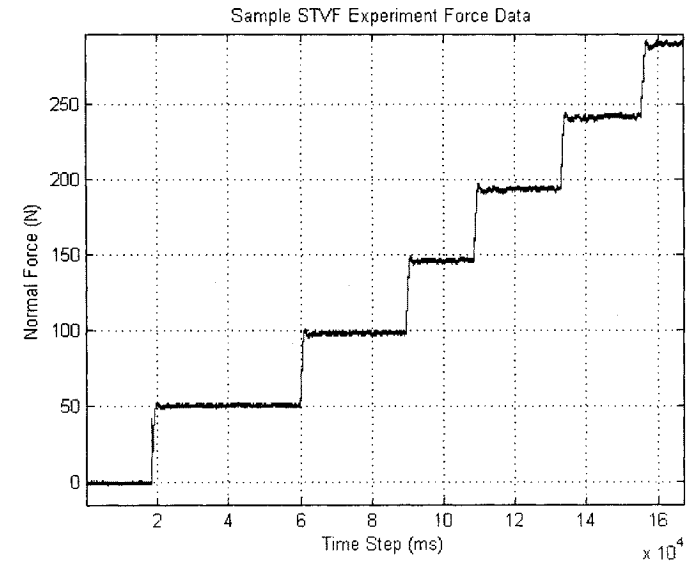

(a)

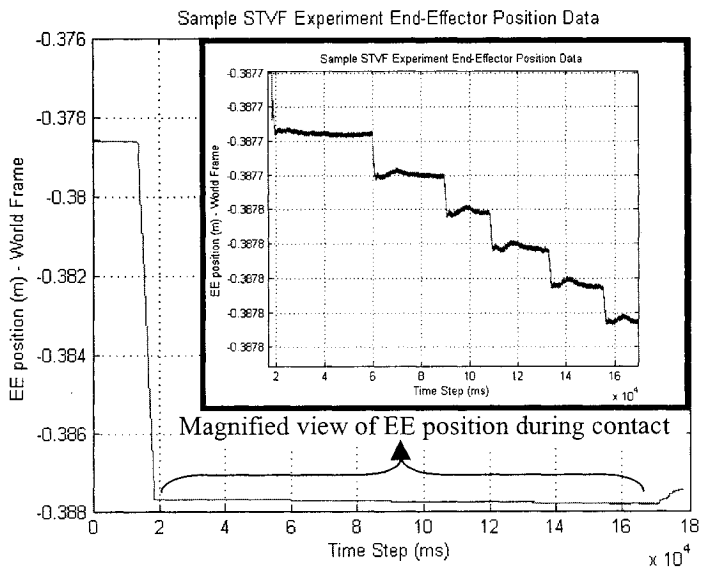

(b)

Figure 3-6 Sample STVF experimental data – Force (a), Position (b)

As discussed in the previous section, the displacement of the system is determined by considering the end-effector position during contact with respect to its position at the instant of initial contact. To determine the instant at which contact begins the force plot is inspected. From the force plot, initial contact can be determined by noting the time index of the first 'spike' in the force reading. The end-effector position at that time index is recorded and considered the 'datum' for calculating subsequent displacements. Figure 3-7 depicts the process of determining the instant of initial contact.

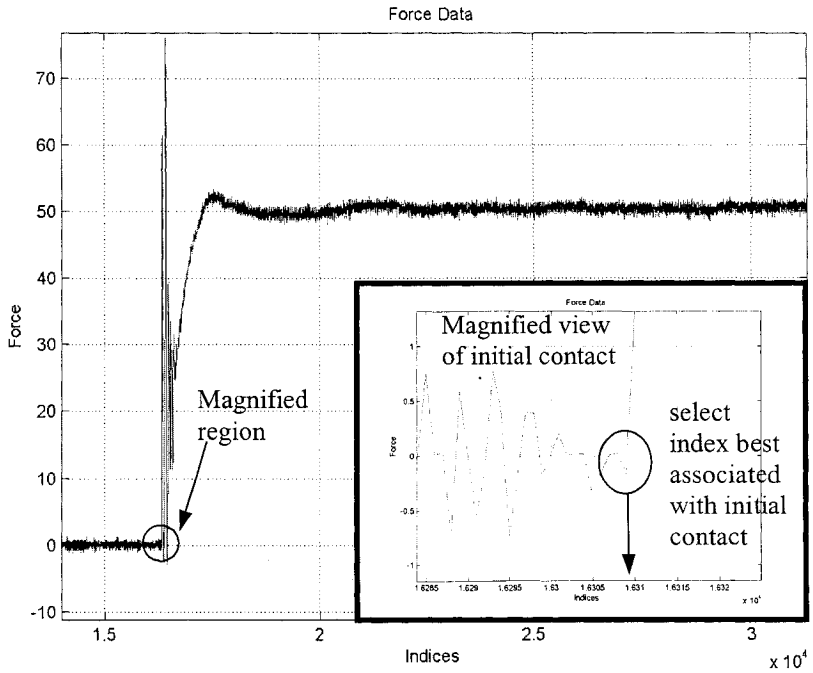

Figure 3-7 Instant of initial contact

In Section 3.2.1, it was mentioned that during the STVF single point contact experiments the payloads are brought into normal contact with the aluminum plate. In reality, the payloads experience contact in a direction slightly off from the ideal normal due to hardware limitations. The orientation data for the end-effector can be used in combination with position data to adjust the calculated normal displacement. Also, although it is assumed that the orientation of the force plate (and hence the orientation of the force plate reference frame) remains constant during contact, in reality, tilting (movement) occurs during contact. However, the present inability to accurately record these orientation changes during the experiments makes it necessary to assume a constant orientation of the force plate.

3.2.5 Single Point Toolbox Parameter Estimation Results

As first mentioned in Chapter 1 for the single point contact problem, only stiffness and damping parameter estimation is considered. A summary of the parameter estimation results is presented here. For a complete set of contact stiffness and damping estimates for each of the STVF payloads, refer to Appendix B.

Toolbox Algorithm Inputs

In Chapter 2, each of the estimation algorithms was described, including the input information required of the user. For the STVF payload experiments the initial guesses for stiffness and damping were typically 1e6 N/m and 50 kg/s, respectively. The RLS and ILS algorithms required the definition of a matrix P_0 and a scalar λ, which were part of the parameter estimate update scheme. P_0 was normally chosen as 1e5*I, with I being the identity matrix; λ was chosen to be 0.98, a typical value [19]. The IA algorithm required a gain matrix to be defined, typically specified as:

$$\Gamma = \begin{bmatrix} 2e9 & 0 \\ 0 & 2.5e3 \end{bmatrix}$$

This gain matrix was chosen by observing the convergence rate of the parameter estimates and thus finding appropriate values to reach convergence within the data available. The frequency domain algorithms require the user to specify 'frequencies of interest' based on an analysis of the frequency spectrum of the input and output signal. These values varied between experiments.

Damping Estimation

As noted in Chapter 1, Erickson [19] and Weber [22] concluded that accurate estimation of contact damping was unlikely without persistent excitation in the robotic motion. It was noted, however, that some estimation of contact damping was possible during the transient response at the initial phases of contact if the convergence rate of the algorithm was sufficiently fast [19, 21, 22]. On this basis, contact damping estimation was attempted for the STVF experiments. Table 3-1 shows the contact damping estimation results obtained with nine single point estimation algorithms for one set of the STVF payload experiments during the transient response phase.

Table 3-1 STVF payload experiments - contact damping estimates during transient phase (kg/s)

Payload	Estimation Algorithm								
	RLS	ILS	IA	Kalman	GLS	ETFE	OEM	EEM	GMLE
Al half-sphere	497.61	5403.82	18.82	3548.13	3695.61	81.24	1612.20	50026.80	3970.54
Pl half-sphere	5.13	0.00	3.19	4038.94	1107.44	1141.48	621.69	1419.53	635.22
Pl cone	0.00	303.64	2.55	1090.99	387.32	-1339.90	-1773.09	-18999.70	-1214.02
Pl pyramid	12.05	0.00	2.79	1478.19	944.49	24.97	-156.83	-10955.40	-190.06
Pl prism	0.00	0.00	2.17	3466.44	1345.63	251.83	-472.20	-62918.20	1587.48
Pl cube	0.01	11767.20	1.86	5791.16	0.00	-1139.52	-1073.70	-1527.55	-1093.38

The damping estimates are inconsistent across the different algorithms, and the negative contact damping quantities are particularly anomalous. The Kalman Filter estimation algorithm is the only algorithm that provides "believable" results, where all the damping estimates are positive and have the same order of magnitude for all payloads. However, since there is no simple method by which these damping estimates of the SMT and payload system can be verified, and considering the already apparent damping estimation problems, further investigation into contact damping estimation for the single point STVF contact experiments is not considered in this research.

Stiffness Estimation

As discussed in Section 3.2.3, the contact stiffness estimates generated by the Single Point Toolbox represent the stiffness estimates for the combined SMT and payload system. Table 3-2 shows the contact stiffness estimates for the first plastic half-sphere STVF experiment. The 'Load Level' column refers to the approximate reaction force recorded at each of the steps in the force level. The linear contact stiffness estimates for this payload are very consistent across the nine estimation algorithms for each load level. It is also noted that as the load level increases, so does the linear contact stiffness estimate. Since there is some expected non-linearity in the stiffness of the SMT and payload system, this behaviour is not unexpected.

Table 3-2 Plastic half-sphere STVF contact experiment #1: contact stiffness estimates (N/m)

Load level (N)	RLS	ILS	IA	Kalman	GLS	ETFE	OEM	EEM	GMLM
50	1.38E+06	1.38E+06	1.38E+06	1.40E+06	1.40E+06	1.41E+06	1.40E+06	1.40E+06	1.39E+06
100	1.69E+06	1.69E+06	1.69E+06	1.63E+06	1.63E+06	1.64E+06	1.64E+06	1.64E+06	1.64E+06
150	1.72E+06	1.72E+06	1.72E+06	1.75E+06	1.75E+06	1.76E+06	1.77E+06	1.77E+06	1.77E+06
200	1.85E+06	1.85E+06	1.85E+06	1.87E+06	1.87E+06	1.86E+06	1.86E+06	1.86E+06	1.86E+06
250	1.95E+06	1.95E+06	1.95E+06	1.92E+06	1.92E+06	1.93E+06	1.93E+06	1.93E+06	1.93E+06
300	1.94E+06	1.94E+06	1.94E+06	1.96E+06	1.96E+06	1.97E+06	1.97E+06	1.97E+06	1.96E+06

The behaviour shown in Table 3-2 is replicated for the STVF experiments with the aluminum half-sphere, the plastic cone and the plastic pyramid. The results, however, for the plastic triangular prism and the plastic cube do not follow the same general pattern. Table 3-3 shows the contact stiffness results for the first plastic cube experiment. Although the estimates are fairly consistent across all nine algorithms, the stiffness estimates at first decrease with increasing load, then subsequently show an increase beginning at the 300 N load level. Compared with the behaviour for the other specimens, these results are unexpected.

Table 3-3 Plastic cube STVF contact experiment #1: contact stiffness estimates (N/m)

Load level (N)	RLS	ILS	IA	Kalman	GLS	ETFE	OEM	EEM	GMLM
50	8.05E+05	8.05E+05	8.05E+05	9.10E+05	9.13E+05	9.79E+05	9.43E+05	9.43E+05	9.58E+05
100	8.29E+05	8.29E+05	8.29E+05	9.16E+05	9.17E+05	9.46E+05	9.41E+05	9.41E+05	9.44E+05
150	7.75E+05	7.75E+05	7.76E+05	8.35E+05	8.35E+05	8.61E+05	8.61E+05	8.61E+05	8.60E+05
200	6.74E+05	6.74E+05	6.74E+05	7.54E+05	7.54E+05	7.66E+05	7.65E+05	7.65E+05	7.64E+05
250	5.90E+05	5.90E+05	5.89E+05	6.22E+05	6.22E+05	6.35E+05	6.31E+05	6.31E+05	6.31E+05
300	6.68E+05	6.68E+05	6.69E+05	6.67E+05	6.67E+05	6.61E+05	6.64E+05	6.64E+05	6.63E+05
350	7.41E+05	7.41E+05	7.40E+05	7.40E+05	7.41E+05	7.43E+05	7.43E+05	7.43E+05	7.43E+05

Further investigation of the contact force and displacement data for the plastic cube payload indicates an anomaly. Figure 3-8 shows a sample portion (~100 N load) of one of the STVF cube payload experiments. The displacement plot shows a steady increase in end-effector position while the force plot indicates a nearly constant load (standard deviation ~0.6 N). In the experiments for the half-spheres, the cone and the pyramid, a

constant load level generated a constant position reading. The STVF cube payload experiments show behaviour as that seen in Figure 3-8 for all the load levels up to 250 N. For the higher load ranges (300 – 350 N), the displacement results behave in a manner roughly similar to that of the other payloads. The results from the STVF prism payload experiments, however, appear normal for the lower 50 N and 100 N load levels, but exhibit the behaviour of Figure 3-8 for all higher load levels – nearly opposite of the cube results. The reason for this anomalous behaviour has not been established at this time.

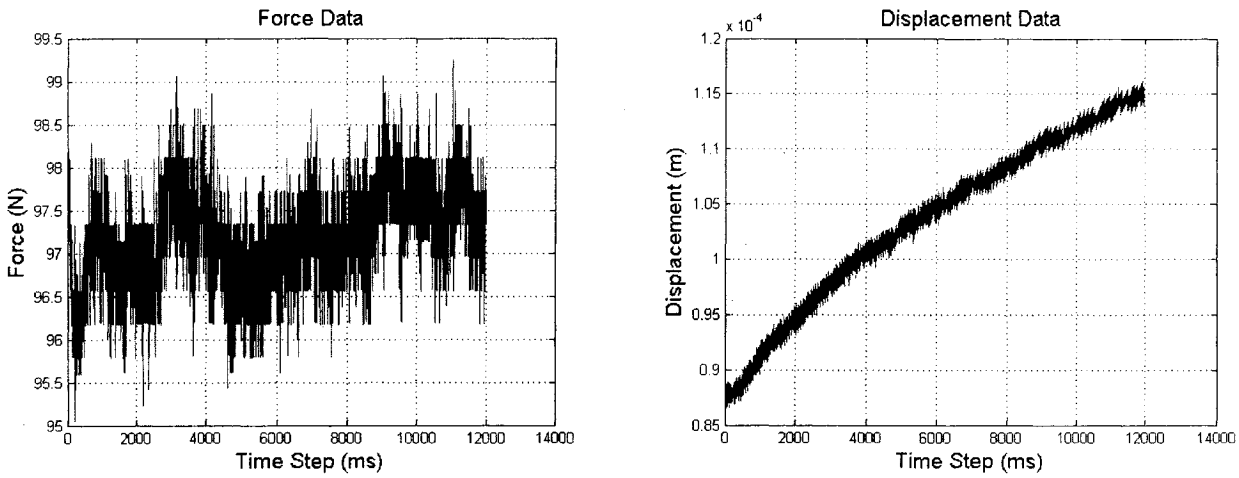

(a) (b)

Figure 3-8 Sample results from STVF plastic cube experiment #1

Table 3-4 shows a summary of the stiffness estimation results for the first experiment with each of the STVF payload experiments. The results given are averages of the results for the nine estimation algorithms for load levels up to 300 N. The complete set of parameter estimates for the experiments is found in Appendix B.

The stiffness estimates listed here are considered to be the $k_{SMT+payload}$ estimates defined in Section 3.2.3. The following two sections will provide information on the SMT stiffness and the payloads' stiffness obtained from independent experiments. We will then use this information to assess the capability of determining the stiffness of the payloads from the $k_{SMT+payload}$ experiments.

Table 3-4 Average stiffness estimates (N/m) of STVF payload experiment set #1

Approximate Load Level (N)	Aluminum half-sphere	Plastic half-sphere	Plastic cone	Plastic pyramid	Plastic prism	Plastic cube
50	1.99E+06	1.39E+06	7.93E+05	5.75E+05	1.02E+06	8.95E+05
100	2.51E+06	1.66E+06	9.61E+05	6.68E+05	1.24E+06	8.99E+05
150	2.59E+06	1.75E+06	1.08E+06	7.25E+05	1.21E+06	8.26E+05
200	2.70E+06	1.86E+06	1.12E+06	7.61E+05	1.03E+06	7.32E+05
250	2.75E+06	1.94E+06	1.16E+06	7.86E+05	1.04E+06	6.16E+05
300	2.79E+06	1.96E+06	1.16E+06	7.96E+05	1.10E+06	6.65E+05

3.3 Contact Parameter Estimation of the SMT

The purpose of this section is to estimate the stiffness, k_{SMT}, of the SMT, separately from the contact payloads. No damping estimation is considered, as per the decision to neglect damping in Section 3.2.5. As mentioned earlier, the SMT refers to the combination of the STVF robot and the worksite force plate.

3.3.1 Experimental and Estimation Procedure

The tests conducted here are similar to those carried out with the contact specimens of Section 3.2, but without the payloads. In these experiments, the micro-fixture, to which the payloads were interfaced in the earlier STVF experiments, is bolted directly to the aluminum plate, approximately at the same location as in the experiments of Section 3.2.

Reaction forces in the range of 50 to 250 N were recorded, with step size increments of approximately 50 N. Figure 3-9 (a) shows the logged force data and Figure 3-9 (b) shows the end-effector position data for the first of two SMT test-bed stiffness experiments. The test was carried out twice to ensure repeatability.

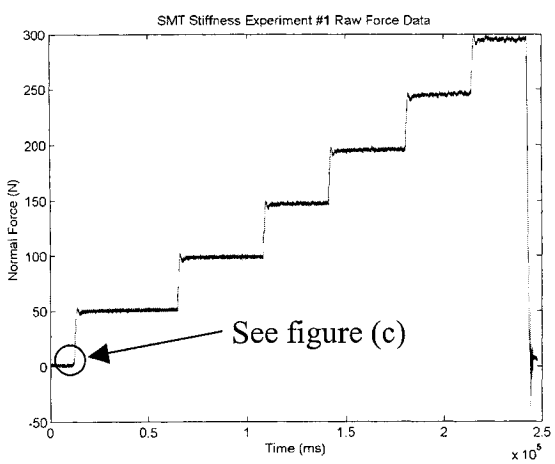

(a)

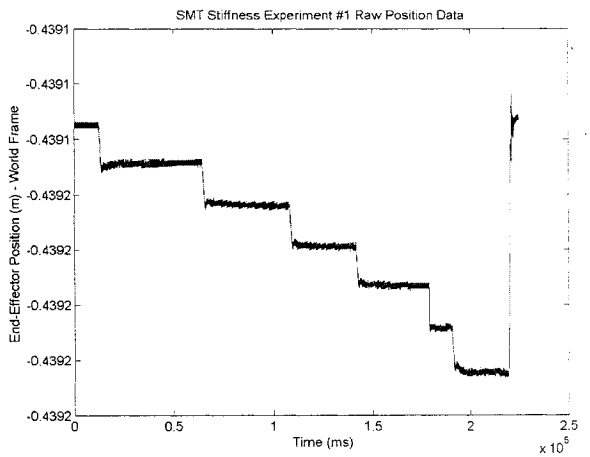

(b)

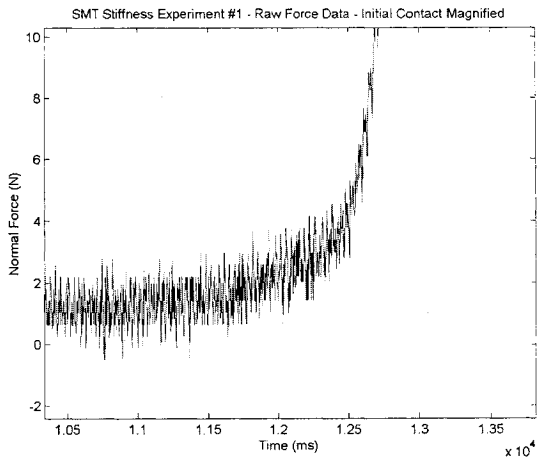

(c)

Figure 3-9 Reaction force and end-effector position data for SMT test-bed stiffness experiments

As seen in Figure 3-9 (a), the stepwise increment in the contact load is clearly evident. Recalling the SMT payload experiments in Section 3.2, the displacement was calculated by considering the current end-effector position with respect to the end-effector position at the instant of initial contact. In that case, the instant of initial contact was determined by locating the first 'spike' in the load reading. Close inspection of the force plot, Figure 3-9 (c), reveals that this method of displacement calculation is not possible for these experiments as there is no clear 'spike' in the load to indicate the instant of initial contact that was present in Figure 3-7. This is likely a result of the need to have the STVF robot grip the bolted micro-fixture prior to the onset of the experiment – the force plate is

already recording a small load and there is no sudden contact recorded. Since we cannot determine an initial instant of contact with confidence in this case, the SMT stiffness estimates are determined through analysis of the load-position plots, instead of using the Single Point Toolbox.

3.3.2 SMT Stiffness Estimation Results

Figure 3-10 shows the load-position plots for the first of the SMT stiffness experiments. The thick, grey 'line' in the figure actually depicts the individual data points from the experiment. Inspection of the plot reveals a nearly linear relationship between the force measurements and the end-effector position measurements. A linear best-fit was determined through the data points – the line representing this best-fit is included in the figure. The slope of the best-fit line represents the stiffness estimate for the SMT.

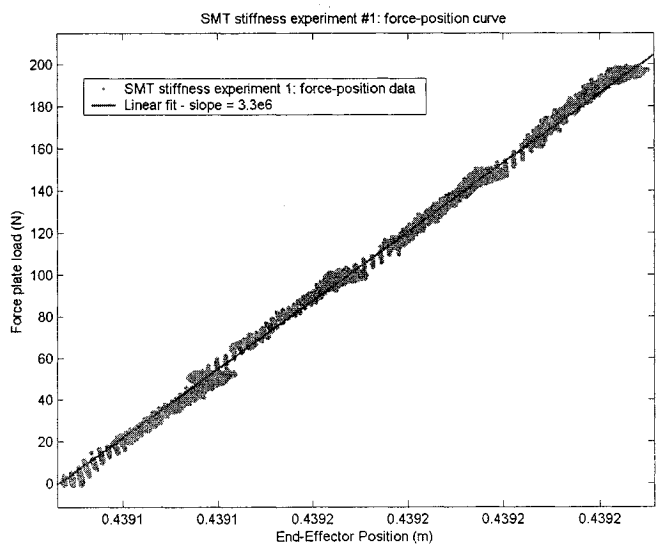

Figure 3-10 Load-position plots for SMT test-bed stiffness experiments

The SMT test-bed stiffness estimates, k_{SMT}, for the two experiments were determined to be 3.3e6 N/m and 3.6e6 N/m, respectively[2]. These stiffness results are used in Section 3.5 together with the estimates for $k_{SMT+payload}$ to calculate payload stiffness from the STVF payload experiments.

[2] Goodness of fit: Experiment #1: $R^2 = 0.9983$, $RMSE = 2.423$, Experiment #2: $R^2 = 0.9978$, $RMSE = 4.261$

3.4 Payload Contact Parameter Estimation

As discussed in Section 3.2.3, the stiffness estimates generated by the toolbox represent the stiffness of a multi-component system. In order to be able to use the STVF payload experiment estimates productively, knowledge of the stiffness of each of the individual components in the multi-component system is required. The purpose of this section is to estimate the stiffness, $k_{payload}$, of the different simple geometry payloads used in the STVF experiments in Section 3.2. Three methods are considered for estimating $k_{payload}$:

- Material testing with an Instron test facility
- Theoretical calculations
- Finite Element Analysis with ABAQUS

Each of these methods is presented in this section, along with the stiffness estimates that they produce. The load-displacement relationships obtained with the three methods are used to generate linear stiffness estimates for the payloads. In Section 3.5, these are used to verify the linear estimates of the payloads produced by the STVF experiments.

3.4.1 Instron Testing for Linear Stiffness Estimates

Experimental Test Facility and Conditions

An Instron Material Testing machine in the Chemical Engineering Department at McGill University was employed to carry out the independent contact specimen stiffness experiments. The Instron machine used was hardware model 1123R, controlled by Model 4500 software (Figure 3-11 (a)). The tower console mounts a moveable crosshead. The load cell is mounted on the crosshead and secured in place with a pair of bolts. The tests used a 5 kN Tension-Compression load cell, which has an accuracy of ± 0.002% of the load cell capacity (or ~ 1 N) or ± 0.5% of the load reading (whichever is greater). This accuracy level applies to the range of 0.4% to 100% of full capacity (~20 N – 5 kN).

Compression testing with the Instron machine is done using two hardened steel compression platens, as seen in Figure 3-11 (b). The upper compression platen is attached to the crosshead, while the base of the machine supports the lower compression platen.

The lower compression platen remains stationary during testing, while the user-specified velocity of the crosshead controls the motion of the upper compression platen.

The Instron machine has the capability of recording reaction forces and crosshead extension (displacement) - the data required to generate characteristic load-displacement curves for the contact specimens. The tower console crosshead extension measurement resolution is ± 0.001 mm or ± 0.1% of the reading (whichever is greater). The tower console has a speed range of 0.001-1000 mm/min.

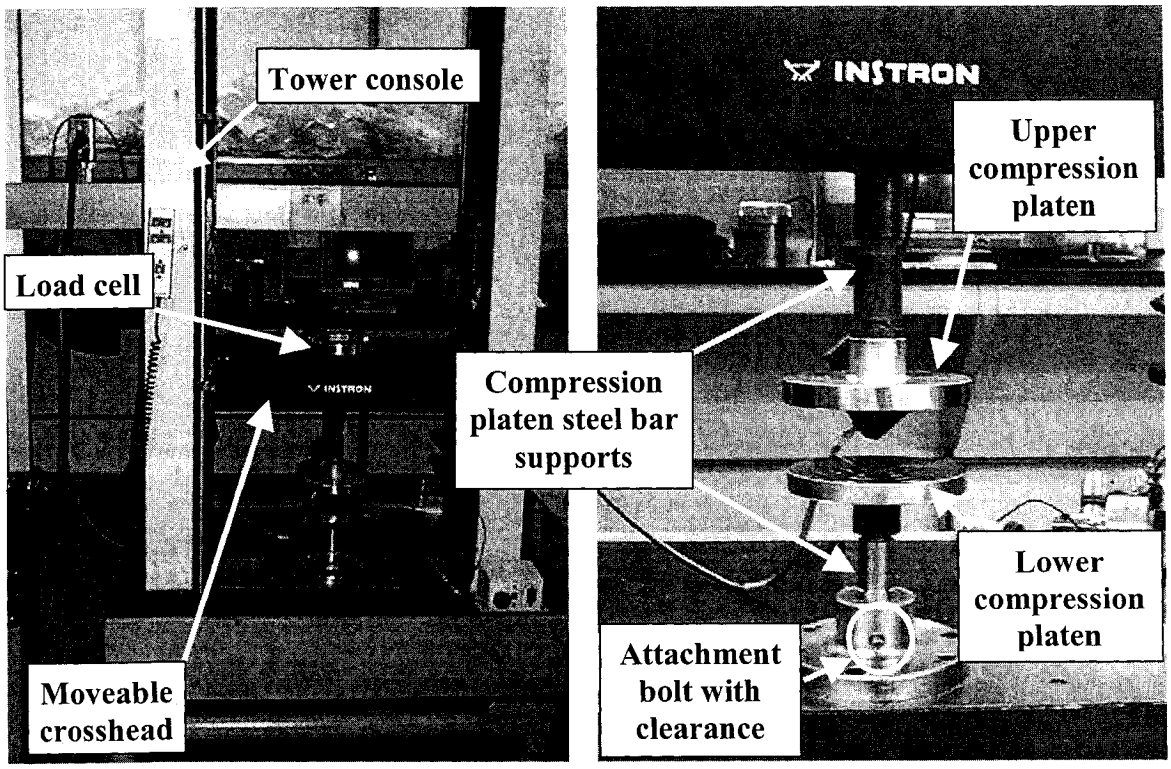

Figure 3-11 Instron material testing machine

Machine Compliance

In addition to the load cell and extensometer resolution limitations, it is expected that a degree of error will be present in the test results due to the compliance of the machine. The most obvious source of compliance is the mechanism used to attach the lower compression platen to the base of the Instron machine. The lower compression platen, which is supported by a steel bar, is held in place by a bolt that connects the steel bar to

the base mounting interface, as shown in Figure 3-11 (b). There is significant clearance between the bolt and the walls of the hole in which the bolt is inserted. We can also predict that compliance is present in the platen support bars and the attachment interfaces between the platens and the bars, as the pieces are only bolted together.

The upper platen and support bar are connected to the load cell. The load cell is bolted to the top of the crosshead. Without these bolts holding the load cell into its receptacle in the crosshead, compression tests would cause the load cell to rise out of its receptacle. Compliance may be present due to this manner of attaching the load cell to the crosshead.

Experimental Procedure

A series of ten quasi-static experiments were conducted on each of the six contact specimens described in Section 3.2.2. Before the tests were conducted, the load cell and extensometer were calibrated. The contact specimens were placed at the centre of the lower compression platen. The upper compression platen was lowered at a constant velocity of 0.0083 mm/s, coming into contact with the top of the contact specimen. This low velocity was used for the testing in order to assume quasi-static loading. The tests were automatically concluded once a reaction force of 400 N was detected. The moderate 400 N load was selected as the cut-off load for material testing since the STVF experiments were limited to 400 N loads by the FMA control scheme.

A series of five quasi-static tests were also conducted with no test specimen between the compression platens. These experiments are referred to as the *compliance tests* and were used to help assess the effect of machine compliance on the contact specimen test results. The raw data extracted from all Instron tests includes reaction load readings and crosshead displacement measurements.

Machine Compliance Experiment Results

As expected, the compliance tests showed some compliance in the Instron test machine under small loads. Figure 3-12 is a sample load-position plot generated using the raw output load and crosshead displacement data from one compliance test. Initial contact between the two platens is assumed to occur at the instant where the load reading exhibits

a rapid increase. As seen in Figure 3-12, this occurs after the crosshead (and hence upper platen) has moved by approximately 1.3 mm. The load reading then leveled out between 40 and 50 N until the crosshead moved a further 0.5 mm. At this instant a rapid load increase is seen over a very small change in crosshead displacement. Most likely, much of the compliance during the period from 1.3 mm to 1.8 mm is due to the clearance surrounding the attachment bolt for the lower compression platen.

The results of these compliance tests are used to estimate a load level at which one can assume that machine compliance is no longer a significant factor. Based on the five compression tests, an average cut-off load was determined to be 48.5 N. For simplicity, it is assumed that the test machine is rigid beyond this cut-off load.

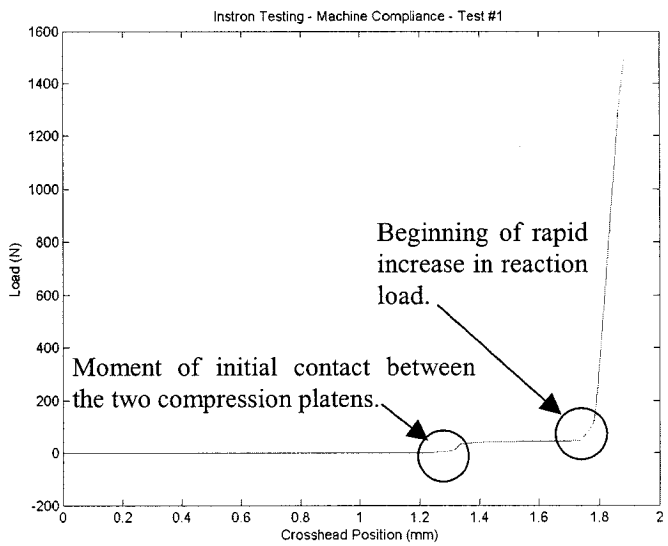

Figure 3-12 Instron machine compliance test sample result

Contact Specimen Experimental Results

Figure 3-13 (a) is a sample set of raw data from one of the ten plastic half-sphere compression tests. As seen in this figure, the compliant behaviour of the Instron machine, as first seen in the compliance test results of Figure 3-12, is replicated in the contact specimen tests. Between the period of initial contact between the compression platen and

the half-sphere and the beginning of rapid load increase, there is significant displacement measured by the moving crosshead.

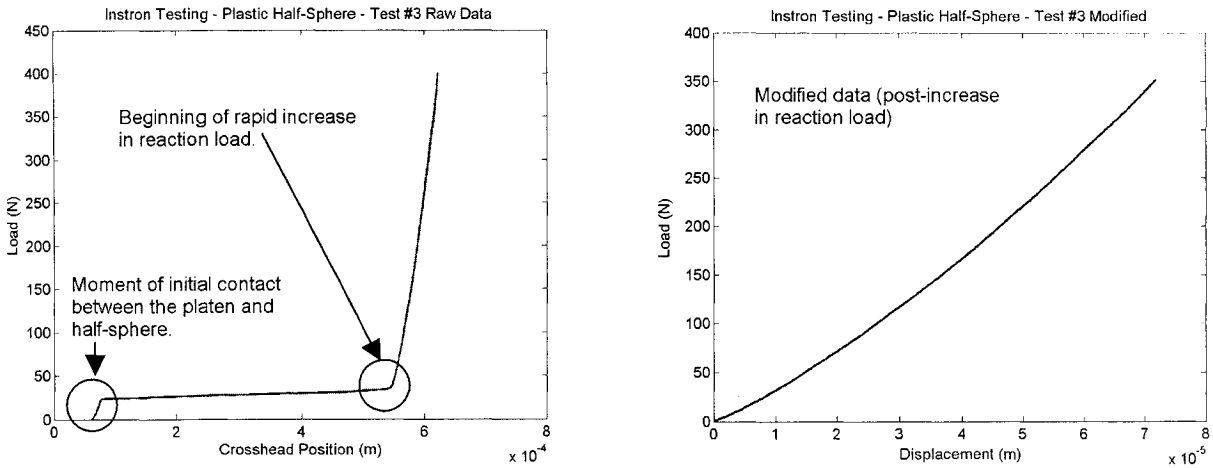

(a) (b)

Figure 3-13 Plastic half-sphere sample Instron test raw data

From the raw test results it is necessary to extract the data related to the displacement of the top point of the contact specimen. Using the bias load determined from the machine compliance tests, only the load data and the corresponding displacement data above this bias (or cut-off) load value are used for further analysis. After discarding the data associated with loads below the cut-off, the load and displacement data are shifted such that the first load-displacement data point occurs at the origin, (0,0), as seen in Figure 3-13 (b). One problem associated with this method of modifying the raw data is that it assumes that no compression of the contact specimen occurs when the reaction load is below the cut-off value. However, this modified data is what we use to find a load-displacement characteristic equation for the contact specimen.

It is evident from Figure 3-13 (b) that the relationship between the load and the displacement is not linear. As such, fitting the data to the linear relationship $F = k\delta$ to find a linear stiffness estimate may not provide the best value to describe the system at a particular load. In light of the non-linearities, the data will first be described by a non-linear relationship, as is described next. Thereafter, linear stiffness estimates will be approximated for the 'Load Levels' mentioned in the STVF experiments in Section 3.2.5.

Load-Displacement Characteristic Equation

The sought non-linear load-displacement relationship for the payloads is of the form:

$$F = k\delta^n \tag{3.1}$$

where k is the non-linear stiffness and n is exponent representing the degree of non-linearity between the load and the displacement of the contact point on the specimen. The Matlab curve fitting toolbox was used to find the optimum k and n values for each of the Instron experiments. Figure 3-14 plots the best-fit curve alongside the experimental data points. The latter comes from the raw data originally shown in Figure 3-13 and corresponds to one of the ten plastic half-sphere Instron tests. A good fit to the data is found, with k = 5.24e7 N/m^n and n = 1.249.

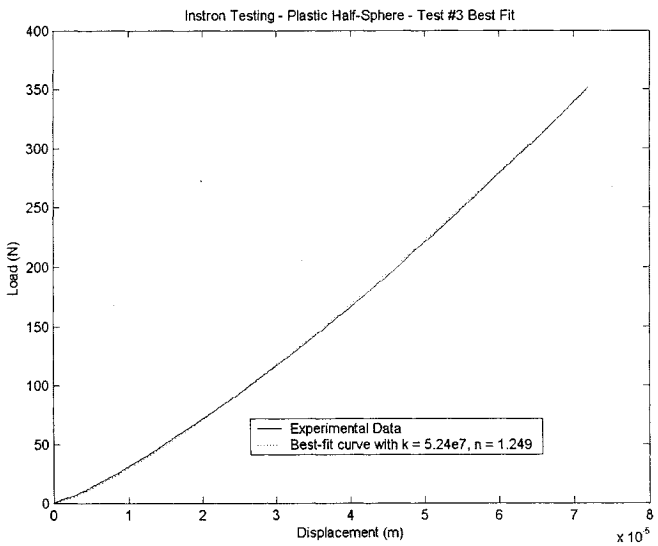

Figure 3-14 Plastic half-sphere test #3 best-fit curve

Curve-Fitting Results

Figure 3-15 shows the load-displacement curves for all the test specimens using the optimum k and n values. From these results, it is determined that the aluminum half-sphere is the stiffest object, followed by the plastic cube, plastic prism, plastic half-sphere, plastic cone and plastic pyramid. The aluminum payload was expected to be stiffer than all the plastic payloads, as the plastic material is more compliant than aluminum (noted by handling the material). For the plastic specimens, the larger contact

areas of the cube and triangular prism provide good reasoning for why these two payloads are the stiffest of the plastic payloads. Inspection of the plastic pyramid and the plastic cone reveal that the slightly more rounded tip on the plastic cone could be sufficient to explain why the cone is stiffer than the pyramid.

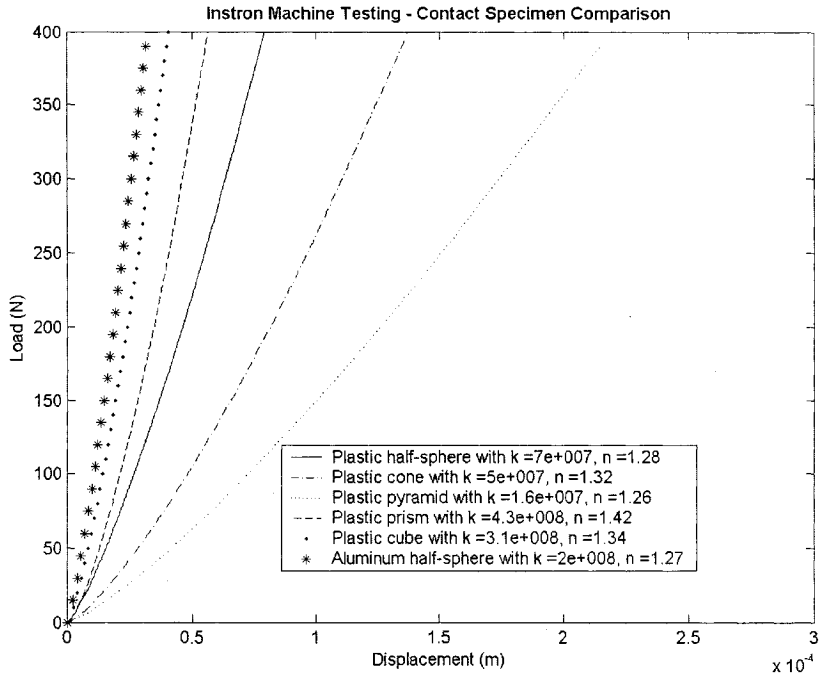

Figure 3-15 Load-deflection characteristic curve comparison between contact specimens

The results of the curve-fitting analysis, averaged over the ten Instron experiments, are shown in Table 3-5. As expected, the load-displacement behaviour of the contact specimens is non-linear (i.e. the exponent n is not equal to unity).

Table 3-5 Curve-fitting results of Instron material tests

Contact Specimen	n	Non-linear stiffness k (N/m^n)
Aluminum half-sphere	1.27	2.01E+08
Plastic half-sphere	1.28	7.00E+07
Plastic cone	1.32	4.98E+07
Plastic pyramid	1.26	1.57E+07
Plastic triangular prism	1.42	4.34E+08
Plastic cube	1.34	3.08E+08

3.4.2 Comparison of Instron Results with Hertz's Theory and Finite Element Analysis

The purpose of this section is to consider two other alternatives for estimating linear stiffness values for the payloads and to compare these results to those generated from the Instron machine testing. In this section we first conduct a theoretical analysis of two of the payloads, the half-spheres, using Hertz's theory of contact. Theoretical stiffness values are not provided for the other contact specimens. In general, the analysis conducted with basic principles of contact mechanics applies to rigid contact specimens indenting a soft environment [42, 43]. However, in this research, the contact specimens are considered the 'soft' material and the environment is considered rigid. This difference puts in question the applicability of the existing contact theory. In light of this, we consider only the half-sphere specimens for theoretical analysis.

This section also presents a finite element analysis of the aluminum and plastic half-sphere as a third alternative for generating linear stiffness estimates of the payloads. The finite element analysis is conducted using ABAQUS/CAE software.

Hertz Stiffness for half-sphere specimens

Hertz's theory of contact suggests that for a half-space coming into contact with a sphere of radius R (Figure 3-16), the interference (displacement) δ of the sphere caused by a particular contact load, F, can be described by the following expression [44, 45]:

$$\delta = \left(\frac{9F^2}{16RE^{*2}} \right)^{\frac{1}{3}} \tag{3.2}$$

Or alternatively, writing F as a function of δ:

$$F = \left(\frac{16}{9} \right)^{\frac{1}{2}} R^{\frac{1}{2}} E^* \delta^{\frac{3}{2}}$$
$$F = k^* \delta^{\frac{3}{2}} \tag{3.3}$$

In the above equations E^* is the equivalent modulus of elasticity of the half-space and the spherical body system [44]. Hertz theory suggests that the applied load is proportional to

$\delta^{3/2}$, related by the factor k^*. Upon substitution of the respective material properties[3] into the aforementioned equations, the theoretical factor relating the applied load and the displacement for the aluminum half-sphere was calculated to be $1.3e^{10}$ N/m$^{3/2}$, while the corresponding factor of the plastic half-sphere was calculated to be 7.0e8 N/m$^{3/2}$. In a later sub-section, these results will be compared with the load-displacement relationships generated from Instron machine testing and finite element analysis.

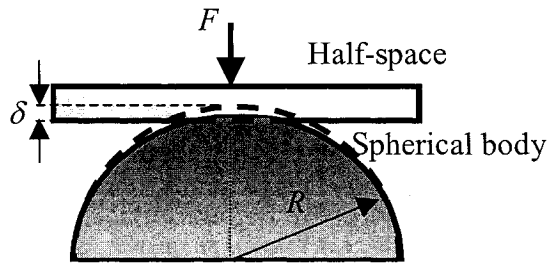

Figure 3-16 Contact deformation with half-space and spherical body

ABAQUS Load-Displacement Curves for the Half-Sphere Contact Specimens

As another alternative for generating load-displacement curves for the half-sphere payload specimens, and subsequently obtaining linear stiffness estimates, an axi-symmetric finite element model was developed in ABAQUS for both the aluminum and plastic half-spheres. To generate a load-displacement relation, the problem was modelled as a half-sphere being loaded by a rigid plane. The plane, like the upper compression platen in the Instron experiments, was lowered at a slow, constant velocity to make contact with the top point of the half-sphere. From ABAQUS, the reaction load and the displacement of a reference node on the rigid plane were recorded for each time step during the simulation. The results of the ABAQUS analyses are shown in Figures 3-17 and 3-18, with the Hertz and Instron testing load-displacement curves for the aluminum and plastic half-spheres included for comparison. Conducting a best-fit analysis of the ABAQUS results yields load-displacement relationship of the form $F = k\delta^n$ with n = 1.55, k = 3e10 N/m$^{3/2}$ for the aluminum half-sphere, and n = 1.49 and k = 6.55e8 N/m$^{3/2}$

---

[3] $R = 0.0287m$ and $E^* = \left(\frac{1-\nu_{hsphere}^2}{E_{hsphere}} + \frac{1-\nu_{half-space}^2}{E_{half-space}} \right)$, with $\nu_{half\text{-}space}$=0.29, $E_{half\text{-}space}$=200e9 Pa, Aluminum half-sphere: $\nu_{hsphere}$=0.33, $E_{hsphere}$=70e9 Pa, Plastic half-sphere: $\nu_{hsphere}$=0.3, $E_{hsphere}$=2.75e9 Pa.

for the plastic half-sphere. Some work was necessary to find a good fit to the aluminum half-sphere data, as the results of the fit were very sensitive to the initial guess for k.

Comparison of Half-Sphere Estimation Results

The three load-displacement profiles obtained with Instron testing, Hertz theory and ABAQUS finite element analysis are displayed in Figure 3-17 for the aluminum half-sphere and in Figure 3-18 for the plastic half-sphere.

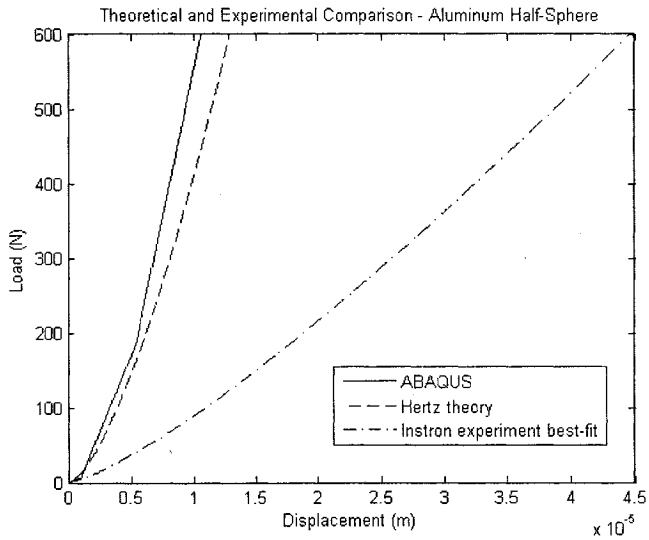

Figure 3-17 Theoretical and experimental comparison of aluminum half-sphere stiffness

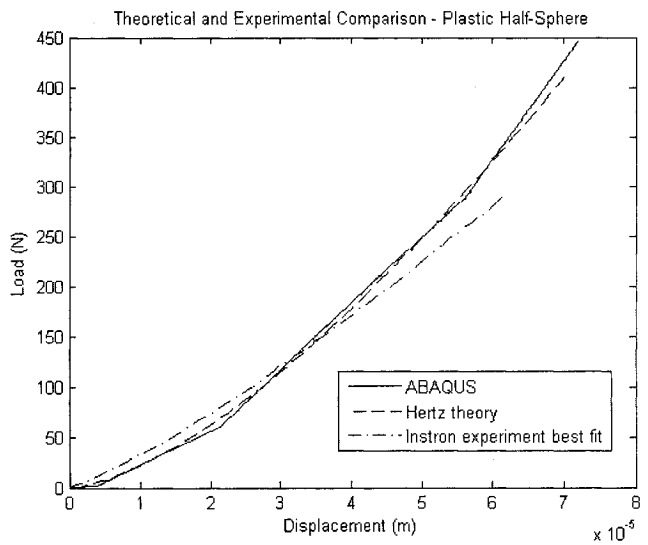

Figure 3-18 Theoretical and experimental comparison for plastic half-sphere stiffness

The ABAQUS simulation results match closely with the Hertz theoretical calculation for the plastic half-sphere, but show some disagreement with the aluminum half-sphere results for loads above 200 N, though the reason for the disagreement is not clear. In Figure 3-17 and Figure 3-18, one can observe small slope discontinuities in the ABAQUS simulation results. These were investigated but no explanation was found. Of more significance, however, is the fact that the experimental results for the aluminum half-sphere are substantially different from the theoretical expectations (Hertz or FEA). The *plastic* half-sphere experimental results, however, show much better correlation with the theoretical and FEA analyses. The lack of success with the aluminum half-sphere experimental results may be partially due to the compliance in the testing machine combined with the relatively high stiffness of the aluminum half-sphere.

Table 3-6 Comparison of load-displacement relationships of the form $F = k\delta^n$

Method	Aluminum half-sphere		Plastic half-sphere	
	n	k	n	k
Instron	1.27	2.01E+08	1.28	7.00E+07
Hertz	1.50	1.30E+10	1.50	7.00E+08
ABAQUS	1.55	3.00E+10	1.49	6.55E+08

The results of Table 3-6 indicate that numerically, the Hertz and ABAQUS predictions are quite similar. The Instron testing suggests much softer properties of the specimens than the other two methods. However, we will make use of the Instron testing results, and the linear stiffness estimates generated from those load-displacement relationships, for the remainder of the analysis. There are several reasons leading to this decision:

1. Consistency: all payload specimens can be analyzed and described using the same method, whereas ABAQUS and theoretical contact mechanics results are not available for all payloads.
2. Discontinuities in the ABAQUS results, combined with inexperience in finite element analysis, suggest taking another route.
3. Both the theoretical and ABAQUS load-displacement relationships assume ideal payloads and ideal loading conditions. Since it is clear that the payloads are not perfect (for example, the plastic cone and pyramid have slightly rounded tips and

not perfect points as one would assume in theory), Instron results may produce better practical results, especially for the plastic payloads.

3.4.3 Payload Linear Stiffness Approximations using Instron Results

As first addressed in Section 3.2.3, the stiffness values of the contact payloads are part of a system, the compliance of which we have assumed can be described by springs in series. We assume that each component of the system can be described by a linear spring. Thus, we can obtain a closed-form expression for payload stiffness using the linear stiffness estimates from the STVF experiments. In addition, the Single Point Toolbox carries out estimation by using a linear stiffness model for the contact force. The implication of this linear assumption is that the non-linear relationships found for the contact specimens need to be used to find linear stiffness values. This subsection introduces one method to accomplish this task.

One simple way of generating a linear stiffness estimate from the non-linear load-displacement curves is to construct a number of lines each representative of the linear stiffness at a particular load-displacement combination. This construction allows us to define a *secant stiffness* that refers to the linear stiffness estimated from the slope of the line joining the origin to the load-displacement point of interest, as shown in Figure 3-19.

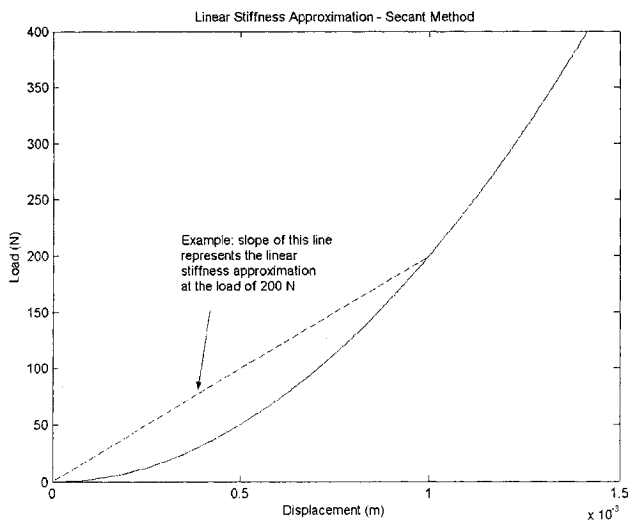

Figure 3-19 Secant linear stiffness approximation from non-linear load-displacement curve

In Table 3-7 we summarize the payload linear stiffness estimates generated using the secant methodology. The mean value of the contact load from the STVF payload experiments was used to calculate the secant estimate. The corresponding displacement required for the secant calculation was determined using the Instron results of Table 3-5, which defined the non-linear $F = k\delta^n$ relationship for each payload. Dividing the mean contact load by this calculated displacement value yielded the secant linear stiffness estimate. The first column in the table is labeled 'Load Level' and is only an approximation of the load at which the secant estimates were generated, as the mean contact load is slightly different for each STVF payload experiment. Similar results were obtained for the second set of the experiments and a summary table is given in Appendix C. Also included in this appendix are secant stiffness tables for the individual payloads where the specific (mean) loads used for approximation of the secant stiffness are listed explicitly.

Table 3-7 Payload linear stiffness (N/m) approximations using secant stiffness

Load Level (N)	Aluminum half-sphere	Plastic half-sphere	Plastic cone	Plastic pyramid	Plastic prism	Plastic cube
50	7.99E+06	3.17E+06	1.76E+06	1.16E+06	3.87E+06	5.83E+06
100	9.20E+06	3.67E+06	2.06E+06	1.33E+06	4.70E+06	6.90E+06
150	1.00E+07	4.00E+06	2.27E+06	1.44E+06	5.29E+06	7.64E+06
200	1.06E+07	4.25E+06	2.43E+06	1.52E+06	5.75E+06	8.22E+06
250	1.11E+07	4.47E+06	2.57E+06	1.60E+06	6.13E+06	8.70E+06
300	1.16E+07	4.64E+06	2.68E+06	1.66E+06	6.48E+06	9.12E+06

We note that though alternative methods of estimating a linear stiffness were considered, such as calculating the slope of a tangent at the load-displacement point of interest, it was decided that the secant approach would be used. The concept of taking the total load and total displacement to find the linear stiffness approximation appears to be a better match considering that the STVF experiments include only periods of contact at a constant load.

3.5 Payload Estimation Using STVF Experiments

In this section, the results of Sections 3.2, 3.3 and 3.4 are used together to estimate the stiffness of the contact payloads and assess the success of the estimation. In Section 3.2,

we determined the stiffness for the SMT and payload combined, which we called $k_{SMT+payload}$. In Section 3.3 we estimated the stiffness of the STVF robot and force plate without the payload, calling this k_{SMT}. In Section 3.4 we determined linear stiffness estimates for the payloads separately, these values labeled $k_{payload}$.

Tables 3-8 and 3-9 list the payload linear stiffness estimation results obtained using the STVF experiments of Sections 3.2 and 3.3 and compare these to the independent payload stiffness estimates $k_{payload}$ from the Instron experiments described in Section 3.4. In particular, the first column in these tables lists the load level of interest, while the second and third columns list the $k_{SMT+payload}$ and k_{SMT} values used to calculate the payload linear stiffness, which itself is listed in the fourth column. This calculated payload stiffness, k_{calc}, is obtained based on the following expression that relates the equivalent stiffness of a system to its components, as per the simplified model of the system in Figure 3-5:

$$k_{calc} = \left(\frac{1}{k_{SMT+payload}} - \frac{1}{k_{SMT}} \right)^{-1} \tag{3.4}$$

The fifth column of the tables, labeled $k_{payload}$, includes the linear stiffness estimates for the payloads generated in Section 3.4 with the Instron experiments. The final column of the table presents the percentage error in k_{calc} from the independently determined $k_{payload}$ values calculated as:

$$error = \left(\frac{k_{payload} - k_{calc}}{k_{payload}} \right) \times 100 \tag{3.5}$$

Detailed payload stiffness estimation tables for the remaining contact payloads and experiments are found in Appendix D. Table 3-10 summarizes the percentage errors in payload stiffness estimation for all contact payloads as obtained from the first set of STVF experiments.

Table 3-8 Payload stiffness estimation from STVF aluminum half-sphere experiment #1

Load Level (N)	$k_{SMT+payload}$ (N/m)	k_{SMT} (N/m)	Calculated payload stiffness, k_{calc} (N/m)	$k_{payload}$ (N/m)	Error (%)
50	1.99E+06	3.46E+06	4.69E+06	7.99E+06	41.30
100	2.53E+06	3.46E+06	9.39E+06	9.20E+06	2.06
150	2.57E+06	3.46E+06	9.97E+06	1.00E+07	0.44
200	2.70E+06	3.46E+06	1.22E+07	1.06E+07	14.85
250	2.78E+06	3.46E+06	1.40E+07	1.11E+07	25.98
300	2.80E+06	3.46E+06	1.46E+07	1.16E+07	26.41

Table 3-9 Payload stiffness estimation from STVF plastic half-sphere experiment #1

Load Level (N)	$k_{SMT+payload}$ (N/m)	k_{SMT} (N/m)	Calculated payload stiffness, k_{calc} (N/m)	$k_{payload}$ (N/m)	Error (%)
50	1.39E+06	3.46E+06	2.33E+06	3.17E+06	26.47
100	1.66E+06	3.46E+06	3.17E+06	3.67E+06	13.54
150	1.75E+06	3.46E+06	3.52E+06	4.00E+06	11.94
200	1.86E+06	3.46E+06	4.01E+06	4.25E+06	5.68
250	1.94E+06	3.46E+06	4.39E+06	4.47E+06	1.61
300	1.96E+06	3.46E+06	4.50E+06	4.64E+06	2.98

Table 3-10 Percentage error in payload estimation using the first set of STVF experiments

Load Level (N)	Aluminum half-sphere	Plastic half-sphere	Plastic cone	Plastic pyramid	Plastic prism	Plastic cube
50	41.3	26.5	41.4	40.5	62.7	79.3
100	2.1	13.5	35.6	37.5	58.9	82.4
150	0.4	11.9	31.2	36.3	64.7	85.8
200	14.8	5.7	31.5	36.0	74.5	88.7
250	26.0	1.6	32.4	36.3	75.7	91.4
300	26.4	3.0	35.0	37.6	74.6	90.0

Payload estimation for the aluminum half-sphere and the plastic half-sphere showed low errors, below 15%, except for 50 N load level and the 150 N load level for the aluminum half-sphere. The payload estimation error for the plastic cone and the plastic pyramid remained roughly between 30 and 40% for all load levels. Payload estimation was the worst for the plastic prism and the plastic cube in these sets of STVF experiments. It

should be noted that the estimation results for the aluminum half-sphere using the second set of STVF experimental data gives large payload estimation error, on the order of 100%. In general, it appears that the success of estimation of the payload stiffness reduces the stiffer the payload.

The results of this section address the main goal of this chapter, which was to attempt to identify the stiffness of simple geometry contact payloads using experiments with the STVF robot and a force plate. From the results presented here, it is evident that estimation of the payload linear stiffness is possible using the SMT. Considering the relatively high stiffness of these payloads (on the order of 1e6 N/m), errors of 50% are acceptable as determining the order of magnitude of the payload stiffness may be sufficient for modelling purposes.

However, some of the error can be attributed to certain factors. First, there is a degree of uncertainty in the Instron measurements as a consequence of the machine compliance. In addition, the method by which linear stiffness estimates were generated from the Instron results is an approximation. Hence, we are comparing a calculated payload stiffness estimate against a value that also carries a degree of uncertainty. The Instron results clearly show non-linear load-displacement relationships for all payloads and approximating this with a linear stiffness (secant stiffness in our case) is problematic. In addition, each of the SMT payload and SMT stiffness experiments were conducted only twice. Increased confidence in the results would be gained if a larger number of experiments were conducted.

Additionally, Section 3.2.5 showed that the data from the STVF experiments for the plastic prism and plastic cube payloads was unreliable. In these experiments, it was noted that a constant force reading corresponded with a continually increasing end-effector position reading. The toolbox estimation results are thus questionable, and may explain partially the larger errors shown for stiffness estimation of these two payloads. Strangely, the Instron experiments suggested that the aluminum half-sphere was stiffer

than the plastic triangular prism and cube, yet the same estimation problems were not apparent. Further investigation into this issue would be recommended.

3.6 Error Analysis of Payload Stiffness Estimation

As seen in the results in this chapter, payload stiffness estimation was poor particularly for the plastic triangular prism and the plastic cube. It was hypothesized that the poor results stemmed from STVF hardware limitations and Instron machine compliance. In this section, we discuss some of the sources of error in payload stiffness estimation.

The usefulness of the estimates generated by the toolbox depends on the degree of confidence we have in their accuracy. There are several sources of error in the contact parameter estimation procedure employed here. Some of the errors are related to the estimation procedure, while others are related to hardware limitations. The sources of error can be separated into two general groups, which will be referred to here as *procedural errors* and *hardware errors*.

3.6.1 Procedural Error

The errors that are associated with the contact parameter estimation procedure are referred to as *procedural errors*. Two examples of procedural error are investigated here. The first example of a user-related procedural error includes the situation when the user is selecting the instant of initial contact. Mistakes in this step lead to skewed displacement values, directly affecting the stiffness estimates generated. The second source of user-related procedural error arises when the user makes poor choices for algorithm input values, such as specifying unreasonable initial stiffness and damping guesses, high tolerances, and limiting bounds on parameter estimates. Changes in algorithm input values have an effect on algorithm convergence.

In addressing the issue of error associated with the selection of the instant of initial contact, a brief study was conducted. A particular reference time index (here referred to as the *base index*) was selected as the best choice for the instant of initial contact (recall the environment datum selection process that was shown in Figure 3-7). Several indices

were chosen in the proximity of the base index, simulating typical user 'error' in index selection. Stiffness estimates were generated using these 'incorrect' indices and were compared to the base stiffness estimate. Results of the analysis indicated that the error in the stiffness estimate was approximately linearly related to the error in the displacement, implying that a misjudgment of 10% in the environment datum location would generate nearly the same degree of error in the stiffness estimate. It should be noted, however that the accuracy in determining the true environment datum through the procedure of Figure 3-7 is limited by the sampling rate of the data (as we might not record the position at the *true* instant of first contact).

To address the second main source of user-related procedural error, a brief investigation into the error associated with poor algorithm input value selections was carried out for one of the single point contact parameter estimation algorithms, specifically the Instantaneous Least Squares (ILS) algorithm, an algorithm which has several input parameters where user error can be introduced. Using experimental data where the expected contact stiffness estimate was on the order of 1e6 N/m, the initial stiffness estimate provided to the ILS algorithm as an input was varied from 0 N/m to 1e12 N/m. The results revealed that up to a stiffness value of 1e10 N/m, error in the contact stiffness estimate was less than 0.5 %. For an initial stiffness value of 1e11 N/m, the error jumped to 4.5 % and subsequently 45 % for an initial stiffness value of 1e12 N/m. Based on these results, it was surmised that the contact stiffness estimates are very accurate even if the initial guess proved by the user is off by several orders of magnitude.

3.6.2 Hardware errors

The errors that correspond to measurement limitations are here referred to as *hardware errors*. As mentioned previously in this chapter, the STVF robot relative position accuracy is 0.2 mm and the force plate resolution is ±0.5 N. These hardware limitations affect the usefulness of the stiffness estimates. It is acknowledged that the position accuracy is the main contributor to error, especially in the work done here where system stiffness is on the order of 1e6 N/m yet the maximum possible load is 400 N.

To get a sense of magnitude of the hardware error introduced to the stiffness estimate generated by the Single Point Toolbox, we consider the simple stiffness relationship $k = F/x$. The contact load F and displacement x readings both contain error. To assess the effect both errors have on the stiffness, k, we combine the perturbations in the displacement and force measurements using the following relationship [46]:

$$\frac{\Delta k}{k} = \sqrt{\left(\frac{\Delta x}{x}\right)^2 + \left(\frac{\Delta F}{F}\right)^2} \tag{3.5}$$

For our purposes here, we assume that the contact stiffness of the system is 1e6 N/m. Under a load of 400 N, the displacement would be 0.4 mm. Based on the hardware limitations mentioned previously, we arrive at:

$$\frac{\Delta k}{k} = 0.5 \tag{3.6}$$

This implies that the percentage error in the stiffness estimate of the SMT/payload combination would be around 50%. This error is dominated by the displacement error. A similar error would be present for the stiffness estimate of the SMT alone. As seen in equation (3.4) the payload estimate is dependent on both the stiffness of the SMT/payload and the SMT alone, thus the error from these two elements combines to introduce error into the payload stiffness estimate.

Throughout this chapter, many sources of error for the payload stiffness estimates were mentioned. Not all of the error was quantifiable, and even though we can produce numerical estimates for some sources of error, we cannot account for all the errors present. However, despite some of the error percentages being numerically large, the estimation of the order of magnitude of the payload stiffness is still possible. For example, obtaining a stiffness estimate of 1.5e6 N/m when the true stiffness is 1e6 N/m, indicates an error in the estimate of 50%. Though 50% at first appears to be a significant discrepancy, the order of magnitude of the stiffness estimate is quite accurate. As previously demonstrated in [47], estimating the proper order of payload stiffness is sufficient for modelling purposes, and we can conclude that the SMT facility can be successfully used for this purpose.

Chapter 4

Multiple Point Contact Parameter Estimation Toolbox

In Chapters 2 and 3, the single point contact parameter estimation problem was considered. The fundamental assumption in those chapters was that the contacting bodies had simple geometries and interacted at a single point only. Chapter 2 focused on the development of a software toolbox that incorporated a selection of single point contact parameter estimation algorithms, each capable of providing contact parameter estimates given experimental data. Chapter 3 included the analysis of single point contact experiments and parameter estimation using the STVF manipulator at the Canadian Space Agency.

In a large number of practical robotic contact tasks, however, it is more likely that the contacting bodies will have complex geometries rather than the simple geometries assumed in Chapters 2 and 3. The bodies with complex geometries are presumably involved in complicated contact situations where contact occurs simultaneously at multiple points. Thus, a Multiple Point Contact Parameter Estimation Toolbox (or *Multiple Point Toolbox*) was developed in parallel with the Single Point Toolbox.

In this chapter the development and implementation of the Multiple Point Toolbox is described. The main motivation in developing this toolbox is similar to that of the Single Point Toolbox motivation: to generate a user-friendly, well-documented Graphical User Interface (GUI) incorporating existing multiple point contact parameter estimation algorithms into a software package that works for various different data file formats.

Again, one important objective is that the software be able to specifically process STVF experimental data generated at the CSA.

The development of the Multiple Point Toolbox is discussed in several stages. The first section presents the underlying identification algorithm, which includes the contact model and the contact parameter identification solution. The original formulation for the identification procedure was presented in [22, 25]. The second section discusses the implementation of the toolbox, in terms of the software and the design, and provides some screen shots of the final product.

4.1 Identification Algorithm

The multiple point contact parameter identification algorithm used in the toolbox provides estimates for the contact stiffness k, the contact damping b and the coefficient of sliding friction μ at the contact points. In providing these estimates the toolbox uses the following information: the interference distance and rate at each contact point, normal and tangential vectors at each contact point, the total number of contact points, and the total force acting on the body. In practical experiments this detailed contact point data is generally not available, especially for complex contact geometries. Hence, the toolbox realistically assumes that only the following data is available from experimental measurements (or simulation) of the contacting bodies and from geometric models:

- The resultant contact force between payload and environment (payload berth).
- The resultant moment on the payload.
- The geometry of the payload and the environment.
- The position and orientation, and their rates, of the payload and environment during contact.

The user is expected to be able to provide the above-listed information if they wish to successfully use the Multiple Point Toolbox. If the user is analyzing experimental data with the toolbox, force and moment sensors on the robot typically provide the load information. In the case of the STVF manipulator, force and moment information can be obtained from a Force/Torque sensor on the robot end-effector assembly or from the

force plate, which supports the payload berth. The kinematics of the payload can be established from robot kinematics, while the position and orientation of the payload berth can be ascertained from external, independent measurements. If the user is running a simulated contact event in the toolbox (such as a battery box gravity drop), then he/she must indicate only the initial position, rate and orientation of the payload and its berth, assuming the simulation provides all subsequent kinematic and dynamic data. The geometric details of the payload and its mating fixture are available from design data.

The following section describes in brief the formulation of the contact parameter identification problem upon which the toolbox parameter estimation routine is based. For a complete derivation of the multiple point contact problem, details can be found in [22, 23, 25]. The next two sections will also indicate to the user how the data that he/she supplies is used to generate the final contact parameter estimates in the toolbox.

4.1.1 Multiple Point Contact Parameter Identification Problem

Figure 4-1 depicts a two-dimensional typical interaction between a robot end-effector, its payload and the payload berth. The end-effector and payload exert a force on the environment through the multiple contacting points. Since the robotic contact tasks are assumed to occur at slow operating speeds, it is assumed that the force measured by the wrist force/torque sensor is equivalent to the resultant contact force. Hence, the resultant force acting on the environment due to the end-effector is:

$$\vec{F}_R = \sum_{i=1}^{N} \vec{F}_i \tag{4.1}$$

where $\vec{F}_i$ is the contact force at contact point i and N is the total number of contact points. $\vec{F}_i$ is divided into the normal and tangential force components at contact point i:

$$\vec{F}_i = F_{n_i}\vec{n}_i + F_{t_i}\vec{t}_i \tag{4.2}$$

where $\vec{n}_i$ is the unit normal vector at contact point i, and $\vec{t}_i$ is the unit vector opposite to the relative tangential velocity at contact point i.

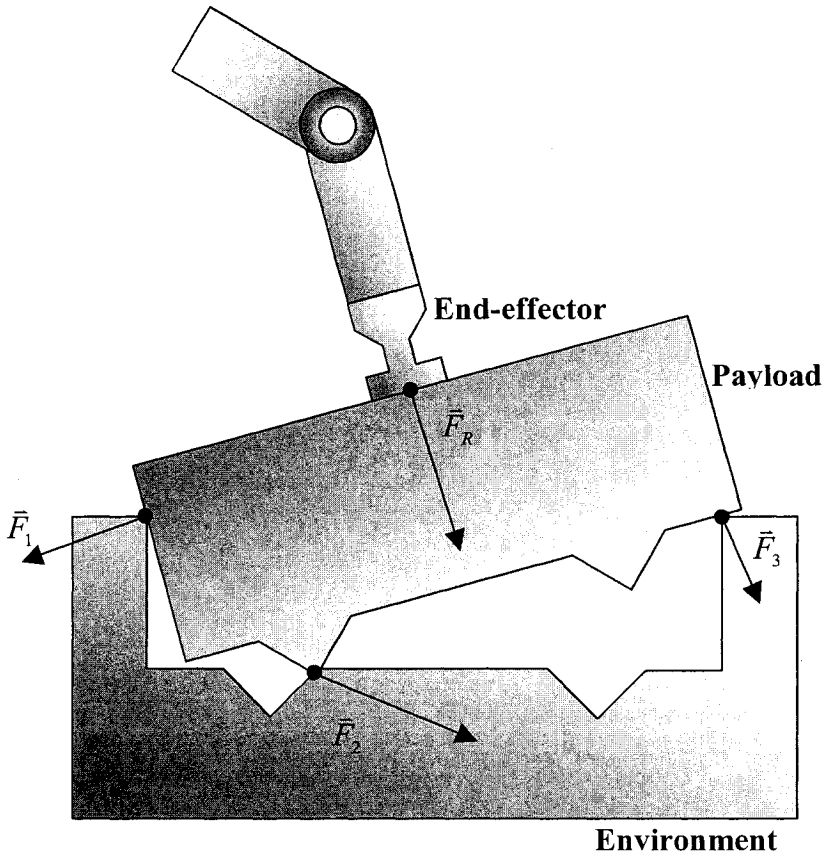

Figure 4-1 Typical multiple point contact

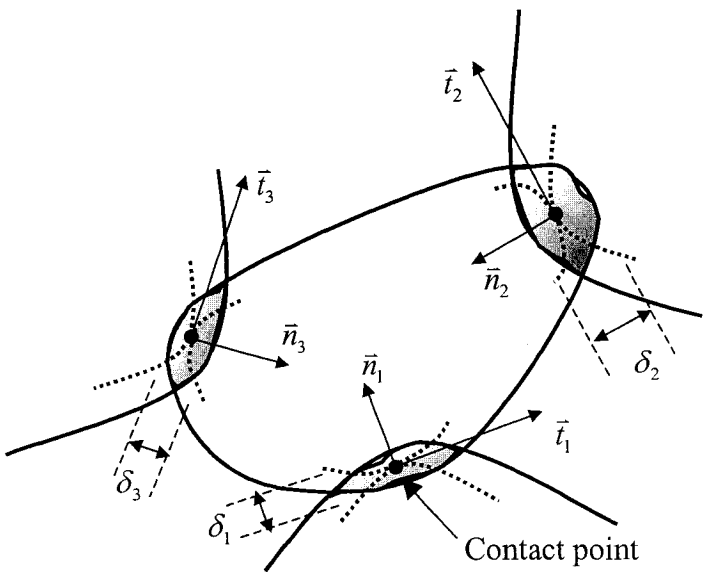

Figure 4-2 Typical multiple point contact interference

As was the case for the single point contact model in Chapter 2, the contact force model in the Multiple Point Toolbox is a linear spring-dashpot model for the normal force at each contact point:

$$F_{n_i} = k\delta_i + b\dot{\delta}_i \tag{4.3}$$

It is assumed that the contact stiffness, k, the contact damping, b, and the coefficient of sliding friction, μ, are identical at each of the contact points. In the multiple point context, δ_i is referred to as the interference distance at contact point i, and $\dot{\delta}_i$ is the interference rate at contact point i. Figure 4-2 indicates some of these model properties (such as the interference and normal and tangential vectors at the contact points) for a general multiple point contact scenario. The tangential force at each contact point is modelled based on Coulomb's law for sliding, assuming that all contact points are sliding[4]:

$$F_{t_i} = \mu_i F_{n_i} = \mu_i k_i \delta_i \tag{4.4}$$

The subsequent substitution of equations (4.3) and (4.4) into equation (4.2) and, finally, equation (4.1) results in the following contact parameter identification problem (refer to [22, 23, 25] for details):

$$\vec{F}_R = \sum_{i=1}^{N} \begin{bmatrix} \delta\vec{n}_i & \dot{\delta}\vec{n}_i & \delta\vec{t}_i \end{bmatrix} \cdot \begin{bmatrix} k \\ b \\ \mu k \end{bmatrix} \tag{4.5}$$

The above represents a linear system of equations for the parameters k, b and μ, which can be solved by using the same techniques as employed for single point contact parameter identification. The parameter identification formulation of equation (4.5) can also be constructed to include moment data. In this situation, equation (4.5) would be augmented and appear as follows:

$$\begin{bmatrix} \vec{F}_R \\ \vec{M}_R \end{bmatrix} = \sum_{i=1}^{N} \begin{bmatrix} \delta\vec{n}_i & \dot{\delta}\vec{n}_i & \delta\vec{t}_i \\ \delta\vec{r}_i \times \vec{n}_i & \dot{\delta}\vec{r}_i \times \vec{n}_i & \delta\vec{r}_i \times \vec{t}_i \end{bmatrix} \cdot \begin{bmatrix} k \\ b \\ \mu k \end{bmatrix} \tag{4.6}$$

[4] damping term $b\dot{\delta}_i$ neglected for sliding

When the moment data is used for analysis, knowledge of the positions of the contact points is required ($\vec{r}_i$). In the context of the toolbox, both parameter identification problems presented in equations (4.5) and (4.6) are options for analysis. In fact, the toolbox user is ultimately able to select between three parameter identification formulations: 1) using force data only, 2) using moment data only, and 3) using both force and moment data.

4.1.2 Toolbox Identification Procedure

The systems of linear equations in (4.5) and (4.6) are used as the basis for the identification procedure implemented in the toolbox. The procedure, which provides a solution for k, b and μk, is described here. The toolbox estimation algorithm considers equation (4.5) (similarly equation (4.6)) formulated in the form of a standard linear identification problem:

$$\vec{F}_R = \sum_{i=1}^{N} \begin{bmatrix} \delta\vec{n}_i & \dot{\delta}\vec{n}_i & \delta\vec{t}_i \end{bmatrix} \cdot \begin{bmatrix} k \\ b \\ \mu k \end{bmatrix} = \phi^T \theta \tag{4.7}$$

At each instant, equation (4.7) is a system of three equations in three unknowns. A standard recursive technique is applied in the Multiple Point Toolbox to determine the parameters at each instant, providing the user with a time history of the local estimates. Furthermore, the toolbox assembles the equations in the form of (4.7) for all time steps into a single global overdetermined system:

$$\vec{F} = \tilde{\Phi}^T \theta \tag{4.8}$$

from which the unknown parameters, θ, are solved using the standard least-squares technique:

$$\theta = (\tilde{\Phi}\tilde{\Phi}^T)^{-1} \tilde{\Phi}\vec{F}_R \tag{4.9}$$

assuming that $\tilde{\Phi}$ is of full rank. Hence, the toolbox also provides a single global estimate for k, b and μk, where μ is directly calculated as $\mu k/k$.

Inspection of equations (4.5) and (4.6) reveals that the toolbox identification procedure as described requires knowledge of several pieces of *geometric* information for contact parameter estimation. This geometric information is not supplied directly by the user and includes the following items:

- the interference distance δ_i at each contact point;
- the interference rate $\dot{\delta}_i$ at each contact point;
- the normal vector $\vec{n}_i$ at each contact point;
- the tangential vector $\vec{t}_i$ at each contact point;
- the total number of contact points, *N;*
- the position of the contact points $\vec{r}_i$;

As mentioned at the beginning of Section 4.1, detailed contact point data (as listed above) is generally not available for practical experiments. However, each of the above-mentioned variables depends strictly on the geometry of the contacting bodies and as such, can be determined through simulation. The simulation software used within the Multiple Point Toolbox is a software library developed by MD Robotics called the Contact Dynamics Toolkit (CDT). CDT is capable of simulating physical phenomena such as impact, bouncing, sliding, rolling, spinning, sticking and jamming for arbitrary geometries and multiple contacts occurring simultaneously [48]. An essential component of CDT is the interference distance determination routine *mindist*, which was developed at the University of Victoria [49]. For a given position and velocity of the robot end-effector (x_R, v_R), a nominal location of the environment (x_E), and the knowledge of the geometry of the contacting bodies, *mindist* solves the interference problem by using an optimization approach. Therefore, it can determine the interference distance, the interference rate, the number and location of contact points, and the normal and tangential unit vectors at each contact point for a given contact scenario, using only the geometric and kinematics data of the contacting bodies. Figure 4-3 illustrates the role of the *mindist* routine within the context of the parameter estimation algorithm in the toolbox.

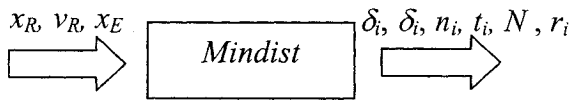

Figure 4-3 Illustration of *mindist* use within toolbox parameter estimation algorithm

The user is required to supply the data listed to the left of the *mindist* box in Figure 4-3, as well as the contacting body geometric data. In addition, the user must provide the following information for parameter estimation: initial guesses for the contact parameters k and μ, an initial guess for the damping ratio and the masses of the contacting bodies. The initial guess for contact damping b is calculated using the damping ratio, contact stiffness and equivalent mass of the contacting bodies. The contact parameter identification routine described here has been thoroughly validated in previous work by using simulated results [22, 23].

4.2 Toolbox Integration and Implementation

In Chapter 2, the implementation of the Single Point Toolbox was described. Similar techniques and software were employed in the development of the Multiple Point Toolbox.

4.2.1 Toolbox Software Implementation

As with the Single Point Toolbox, the Multiple Point Toolbox was developed in the Matlab 6 Release 13 environment, using the GUIDE design tool described in Section 2.3.1. Again, a major advantage of creating the GUI to run the simulation and estimation routine is the encapsulation of the details of the algorithms from the user.

Unlike the Single Point Toolbox, the Multiple Point Toolbox uses Simulink as part of the simulation and estimation routine. Simulink is a popular software package, linked to Matlab, which is used for modelling and simulating dynamic systems. Using Simulink is necessary for the Multiple Point Toolbox because the CDT library used at the CSA comes in the form of a Simulink block. Recall that the core of the estimation algorithm requires the contact kinematics output from *mindist* of CDT to calculate the contact

parameters. Accordingly, the toolbox interfaces between the Matlab scripts and the Simulink blocks. The original implementation of the estimation algorithm was coded in Matlab script. In order to interface the algorithm with the GUI and with the CDT Simulink block, certain modifications were required. No modifications, however, were required to be made to the core calculations. Additionally, CSA made some minor modifications to the CDT software package in order to allow for the extraction of the detailed contact point information from the *mindist* (Figure 4-3) routine. The toolbox *Help* documentation was implemented using Hyper Text Mark-up Language (HTML) and integrated with standard Matlab Help.

4.2.2 Toolbox Architecture and Functionality

The general architecture of the Multiple Point Toolbox is shown in Figure 4-4. Upon inspection of the figure, it is possible to note the variety of options available to the user when using the toolbox. At the beginning of this chapter, a few general goals for the toolbox were given. While addressing these goals, consideration was given to providing additional flexibility in multiple point contact simulations and parameter estimations.

The flexibility of the toolbox appears in the form of allowing the user to:

- perform a multiple point contact parameter estimation only, or
- perform contact kinematics calculation only (i.e. using CDT *mindist*), or
- perform both a contact kinematics calculation and a parameter estimation in one step

The first option ("Estimation" only) given above is used when all the required dynamic and kinematic data are available for the multiple point contact estimation algorithm. Specifically, this means that the user has properly formatted load data and contact kinematics data (the interference distance, the interference rate, the number and location of contact points, and the normal and tangential unit vectors at each contact point). By entering this data into the "Estimation" option in the toolbox, the user obtains contact parameter estimates. The second option given ("Contact kinematics calculation" only) allows the user to generate contact kinematics data for a particular contact event, making

use of the *mindist* routine in CDT. As mentioned previously, the *mindist* routine requires geometric data of the contacting bodies as well as kinematic data. The user either supplies experimental kinematic data of the contacting bodies or simulates the contact event in the toolbox using CDT to generate the body kinematic data. The output from this second option includes all the contact kinematics data required for using the multiple point contact estimation routine in the "Estimation" only option. The third option given combines the other two options into one step.

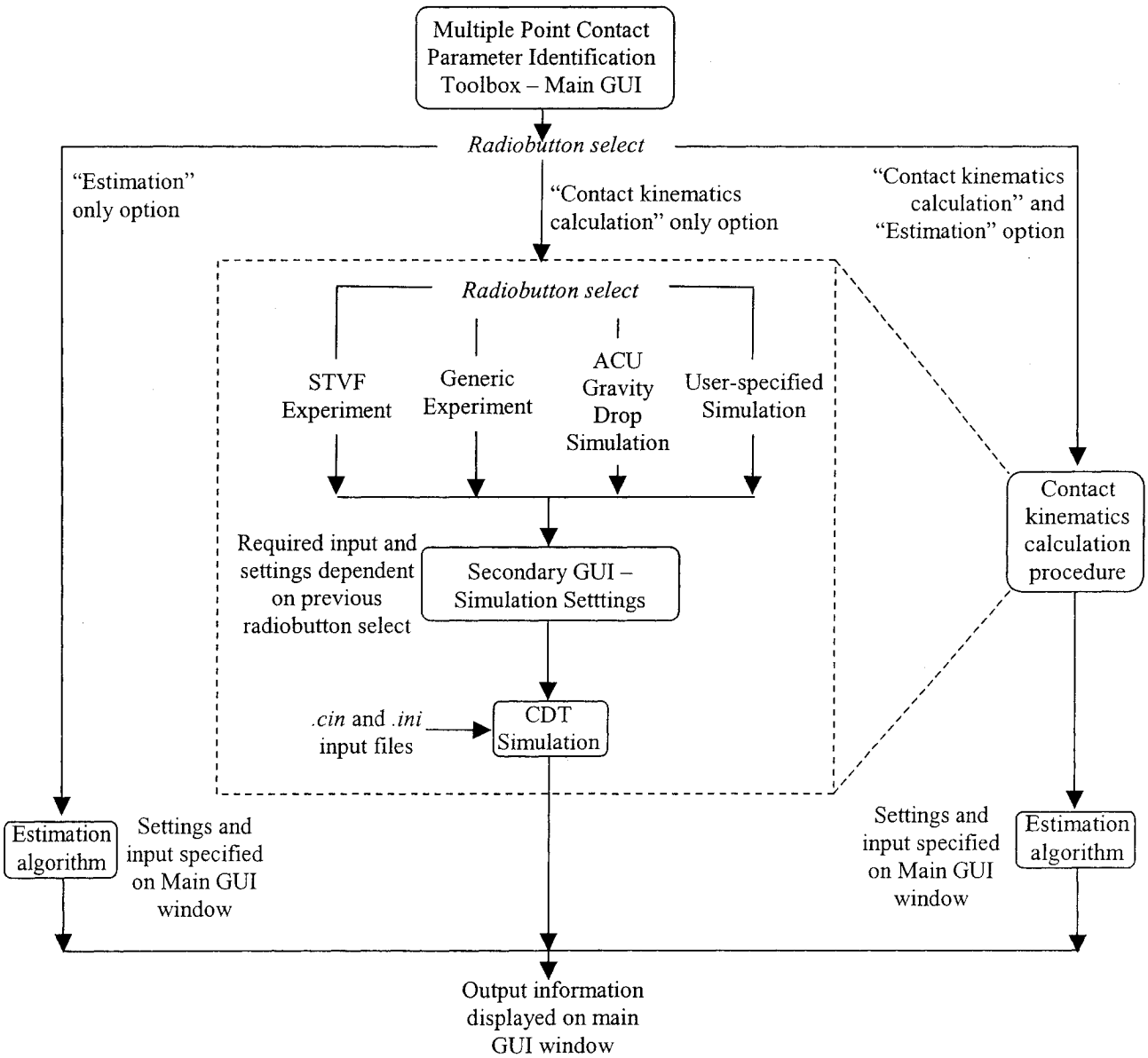

Figure 4-4 General toolbox architecture

Furthermore, the user has several choices regarding the type of experiment that he/she can use for contact kinematics calculation and parameter estimation. The current options in the toolbox include:

- contact kinematics calculation or parameter estimation with STVF experimental data;
- contact kinematics calculation or parameter estimation with general experiments (generic input format required);
- simulation and contact kinematics calculation or parameter estimation for the *ACU Gravity Drop Simulation;*
- simulation and contact kinematics calculation or parameter estimation for a user-specified simulation (i.e. should the user wish to create a contact simulation).

The first two options listed above assume that the kinematic data of the payload and environment (i.e. position and velocity of the robot end-effector and nominal location of the environment) is provided before using the toolbox. The third option refers to a standard simulation scenario used for analysis in this thesis and at CSA. The *ACU Gravity Drop Simulation* represents the small drop of an Arm Computer Unit (ACU) into its receptacle. The ACU represents a real ISS payload to be operated by the SPDM. The details about the *ACU Gravity Drop Simulation* are described in detail in Chapter 5. For this particular case, the kinematic data (the position, velocity and orientation of the falling ACU body) is generated with a Simulink model of the gravity drop included within the toolbox. The fourth and final option indicates the toolbox's capability of integrating an *original, user-specified* Simulink model into the estimation procedure. If the user wants to simulate specific motion of the contacting bodies, the toolbox instructs the user how to integrate their Simulink model with the *mindist* and estimation routines in the toolbox. The toolbox *Help* documentation includes detailed demonstrations on using each of these options. A screen shot of the documentation is shown in Figure 4-5.

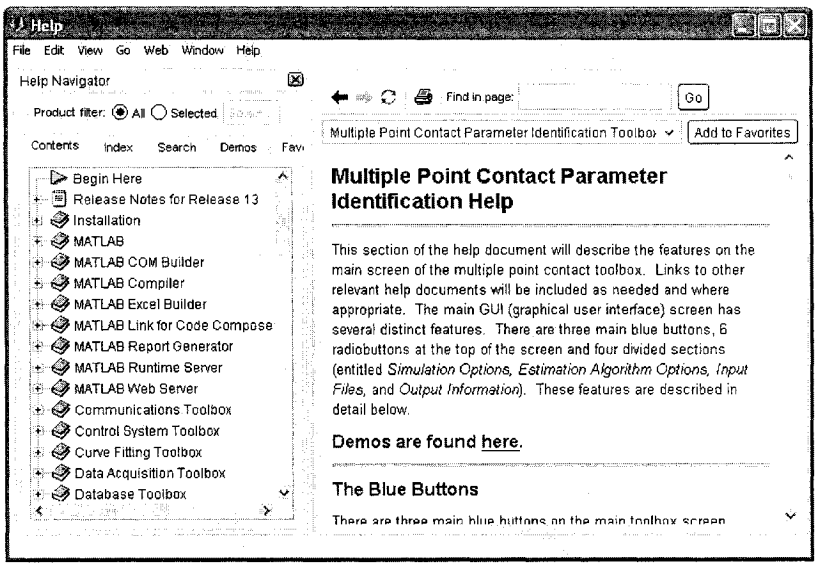

Figure 4-5 Toolbox help documentation screen shot

All estimation algorithm parameters are set on the main toolbox GUI window. Detailed input parameter information essential to the CDT simulations is specified on a secondary GUI window, accessed from the main window. It is in this portion of the toolbox where the user is able to choose the required CDT input files. The user specifies the geometry data file for the contact files, which has a *.cin* extension, and the simulation settings file, which has an *.ini* extension. The *.cin* files are generally created using 3D Studio and CD Modeller software. CD Modeller allows for the input of contact dynamic parameters and can be used to generate the *.ini* file. Both of these files, however, can be generated independently of specific software provided the user adheres to the proper format. Screen shots of the main GUI window and the secondary settings GUI window is given in Figure 4-6. The user also has some control over what output data plots are generated, and can specify their output preferences on the main GUI for estimation and on the secondary GUI for contact kinematics calculation and simulation. The parameter estimates are displayed on the main GUI window following estimation.

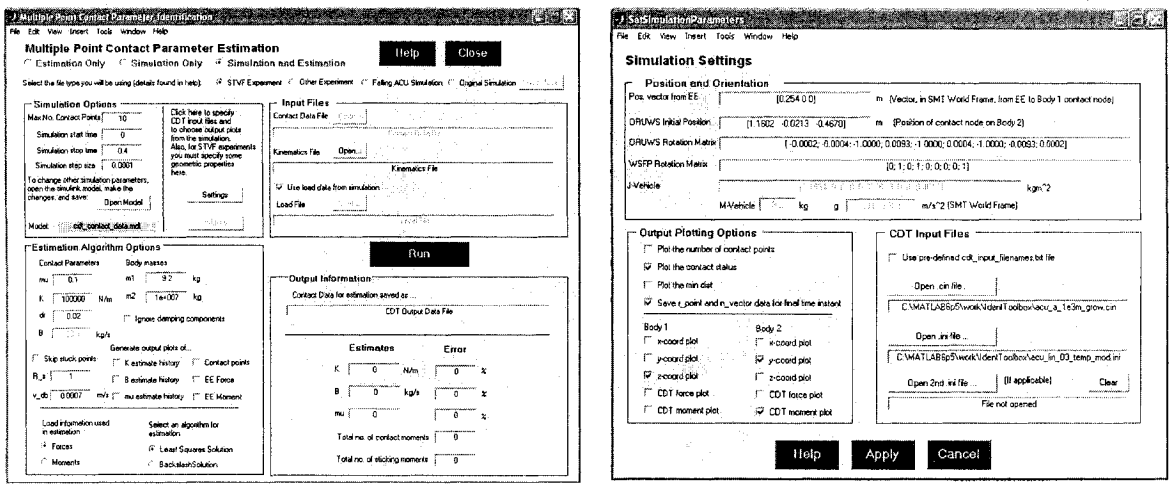

Figure 4-6 Main toolbox GUI

As discussed with the Single Point Toolbox, the Multiple Point Toolbox allows only for *offline* contact parameter estimation. When running an estimation routine, the user is provided with a global least squares estimate for the parameters. If they choose, the user can also view a time history plot of the least squares solution to the parameter estimation problem at each time step. Similarly, the toolbox has also been programmed with a number of error checking features. Furthermore, to save processing time, the toolbox is designed to save data at various operating stages. For example, when a user runs a CDT simulation using the toolbox, the data that would be used for a parameter estimation routine is automatically saved to a file in the proper input format. This automatically generated file can later be used directly for parameter estimation, without requiring the user to re-run the CDT simulation. Finally, as with the Single Point Toolbox, the Multiple Point Toolbox was integrated in CSA's modelling environment in the form of a Simulink block.

Chapter 5

Multiple Point Contact Parameter Estimation

In Chapter 4 the development of a software toolbox, which included a simulation-validated multiple point contact parameter estimation algorithm, was presented. In this chapter the Multiple Point Toolbox is used to study multiple point contact parameter estimation in experimentation and simulation. More specifically, this chapter has two main focuses. The first focus is multiple point contact parameter estimation using experimental data. The results of these experiments are presented and the feasibility of multiple point contact parameter estimation with the existing algorithm and hardware is discussed. The contact parameter estimation results come from a series of experiments that were carried out using the SMT. In these experiments, an Arm Computer Unit (ACU) mock-up was inserted into its receptacle (or berth) following a pre-defined trajectory [41]. The second focus of this chapter involves using a simulated ACU insertion to shed some light on the reasons for poor estimation from experimental data. In particular, attention is given to the sensitivity of the estimation algorithm to mismatches in geometry between the physical ACU unit and the toolbox ACU model geometry files.

5.1 STVF Contact Experiments with the ACU Payload

In this section, multiple point contact experiments and the contact parameter estimation results from these experiments are presented. We first introduce the payload used in the experiments and describe the experimental procedure before presenting the estimation results and the subsequent discussion of said results.

5.1.1 Arm Computer Unit Mock-up Payload

On the International Space Station (ISS) the ACU is a typical Orbital Replacement Unit (ORU). The ACU is a main control element of the SSRMS. For on-Earth validation of on-orbit ACU insertion tasks, a mock-up of the ACU assembly is used in experimentation. The ACU mock-up is used specifically in the development and planning of contact related tasks, particularly the insertion and extraction of ORUs. Figure 5-1 shows the ACU mock-up and its docking receptacle. The ACU v-guides and their mating guides are indicated in the figure.

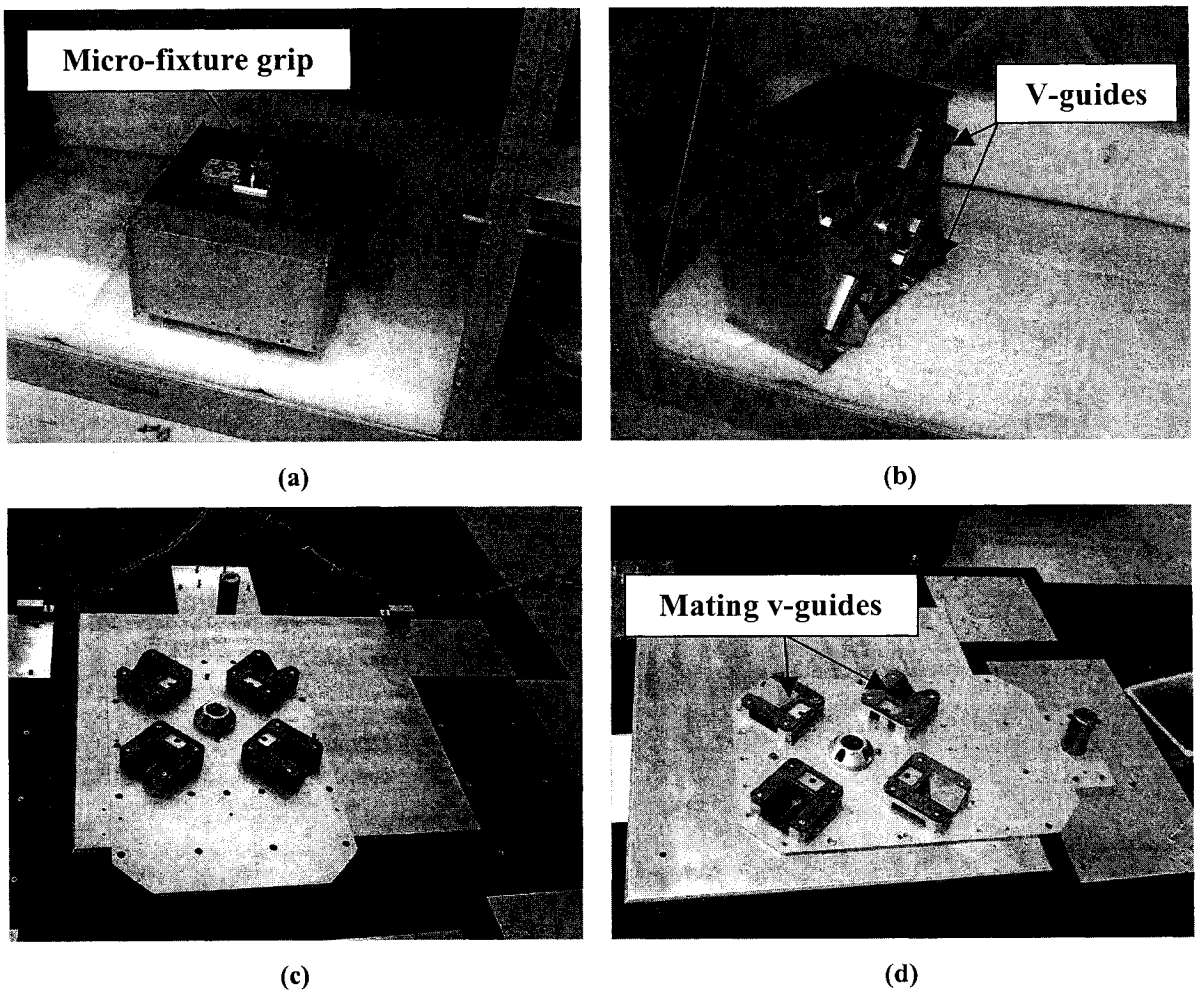

Figure 5-1 ACU (a, b) and ACU berth (c, d) mock-ups

The ACU mock-up has a mass of 9.2 kg and the external dimensions of the body are 33.78 cm x 19.15 cm x 31.57 cm. The ACU mock-up is designed to have the same exterior dimensions as the real unit to be used in orbit. In Figure 5-1 (a) the micro-fixture gripping attachment is visible on top of the ACU. The STVF robot manipulates the ACU payload by gripping this micro-fixture, which is the same micro-fixture used in the single point contact experiments in Chapter 3. The ACU berth, shown in Figure 5-1 (c) and (d) is mounted on the aluminum plate atop the force plate. Due to the complex geometry, the insertion of the ACU into its berth will result in many points of contact between them, the number and locations of which will vary during the insertion task.

5.1.2 Experiment Conditions and Estimation Procedure

The ACU multiple point contact experiments, originally described in [41], were carried out using the STVF robotic facility described in Chapter 3. Two different ACU insertion trajectories were used in our experiments. Each begins with the ACU inserted into its receptacle to establish a reference position and orientation, thus allowing for subsequent relative motion positioning. The subsequent trajectories are described below. The directions refer to the SMT World Frame specified in Chapter 3.

- *Experiments 1a & b:* the ACU is raised ~ 27 mm by the STVF in the $+z$ direction and moved sideways ~ 27 mm in the $+x$ direction. A $-z$ motion is used to reinsert the ACU into its receptacle.
- *Experiments 2a & b*: the ACU is raised ~27 mm by the STVF in the $+z$ direction and rotated ~0.1° about the $+z$ axis. A $-z$ motion is used to reinsert the ACU into its receptacle.

In all experiments, the insertions are performed at a relatively slow speed of 2 mm/s.

In Figure 5-2, we recall the contact parameter estimation procedure for multiple point contact experiments with the STVF facility. The Multiple Point Toolbox incorporates all the steps of the estimation procedure outlined in Figure 5-2, however we have to be sure to provide the correct kinematic and load data. The toolbox requires the kinematic data

of both of the contacting bodies, expressed in a specific reference frame on each of the bodies. This information, together with the geometry of the bodies is input into the CDT *mindist* routine. The ACU *receptacle* position and orientation were determined before the experiments were conducted. Although the ACU receptacle does move once contact begins with the ACU body, the available hardware does not allow accurate determination of the receptacle's pose during contact. Therefore, the position and orientation of the receptacle's reference frame were assumed to remain constant during parameter estimation. The position, orientation, velocity, and angular velocity of the ACU reference frame were determined from end-effector data. Since the ACU reference frame is offset from the end-effector frame, a transformation was required to transform end-effector kinematic data into the kinematic data of the ACU reference frame. Figure 5-3 indicates the reference frames in question.

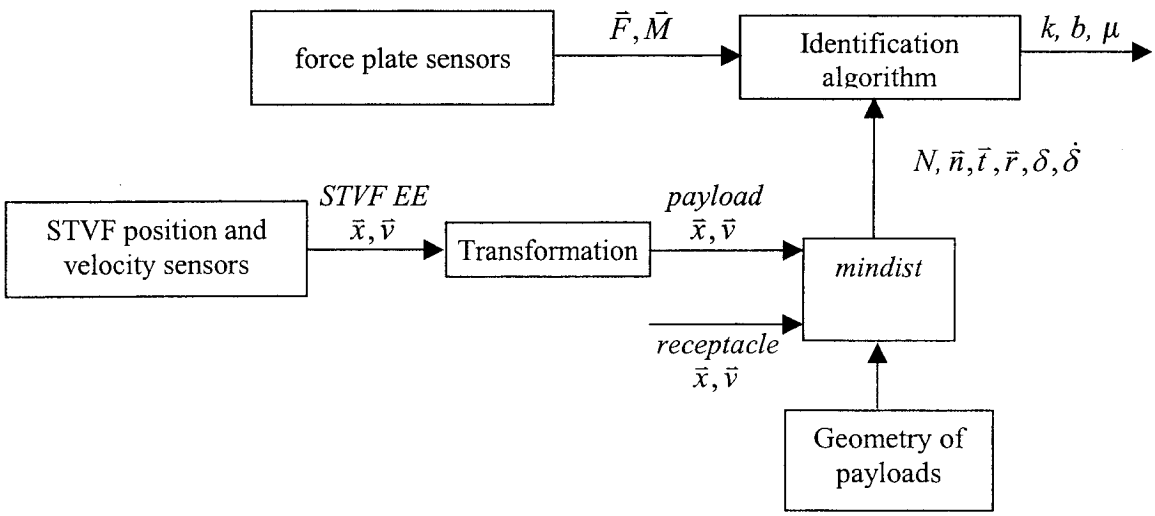

Figure 5-2 Multiple point contact parameter estimation

Figure 5-2 also indicates the need to provide force and moment information for the estimation algorithm in the Multiple Point Toolbox. This information is obtained from the force plate data and, through the use of the toolbox, is expressed in the ACU receptacle reference frame. Based on the results of Patel's work [23] where it was determined that using moment information has little effect on the accuracy of estimation,

we do not use moment data to generate contact parameter estimates. Provided that the position, velocity, geometry and force information are sufficiently accurate, based on previous simulation work by Patel [23], we expect realistic contact stiffness, damping and friction estimates.

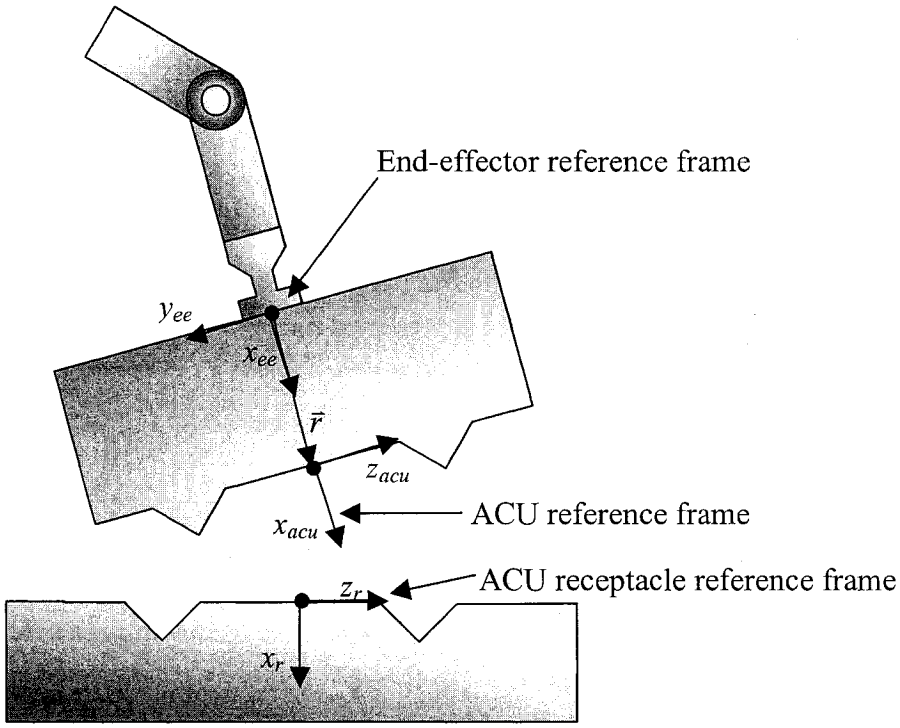

Figure 5-3 ACU and receptacle reference frames

5.1.3 Parameter Estimation Results for ACU Experiments

From each of the four sets of experiments (*Experiment 1a* through *Experiment 2b*), the kinematic and force data used for estimation corresponded to the ACU re-insertion phase (approximately 40-50 seconds of experimental data). As an example of the data obtained from the experiments, Figure 5-4 and Figure 5-5 show Cartesian position information of the end-effector and worksite force-plate measurements, respectively, for *Experiment 1a*. Figure 5-4 shows the time period when the ACU was lifted from the receptacle, shifted, and then lowered towards the receptacle. Data between 30 and 80 seconds of the experiment was used for estimation and represents the re-insertion portion of the experiment.

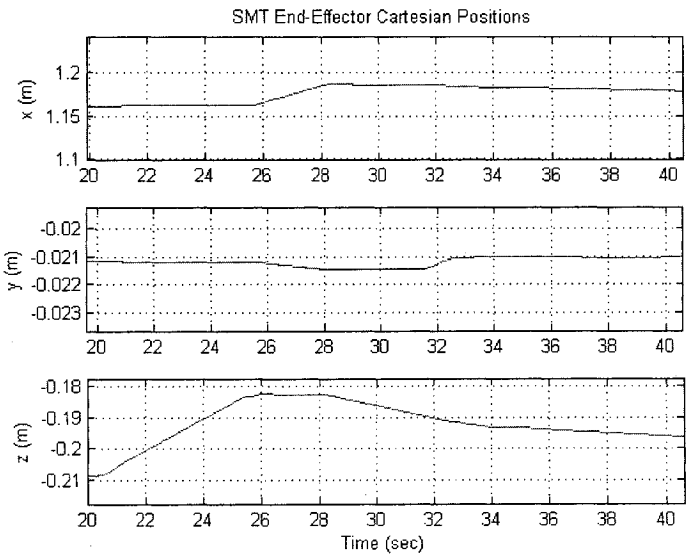

Figure 5-4 Cartesian position of the end-effector for ACU *Experiment 1a*

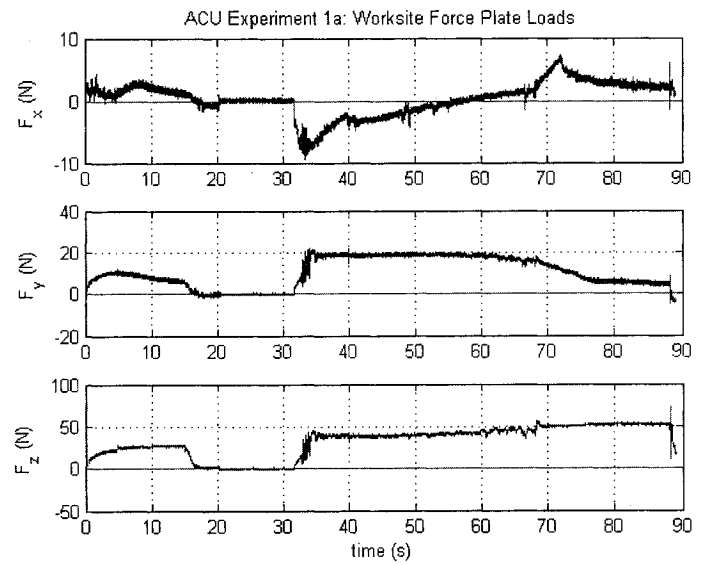

Figure 5-5 Worksite force-plate measurements for ACU *Experiment 1a*

The contact parameter estimation results from the four experiments are listed in Table 5-1, obtained with the global least squares estimation algorithm incorporated in the *Multiple Point Toolbox*. Figures 5-6 (a) through (d) show the estimation results over time for ACU *Experiment 1a,* which correspond to the estimation results in Table 5-1.

Table 5-1 Contact parameter estimation results for ACU experiments

	Stiffness Estimate, k (N/m)	**Damping Estimate, b (kg/s)**	**Coefficient of Friction Estimate, μ**
Experiment 1a	0.00	0.00	Inf
Experiment 1b	3918.36	0.00	0.00
Experiment 2a	3625.65	0.00	0.00
Experiment 2b	1141.23	0.00	0.00

A quick review of results in Table 5-1 clearly indicates that the contact parameters are not estimated properly. The estimates for friction and damping predicted by the global least-squares procedure in the *Multiple Point Toolbox* are zero and clearly incorrect. The *Multiple Point Toolbox* does produce a stiffness estimate for three out of four experiments although, as discussed further on, the predicted value is three orders of magnitude lower than expected.

Inspection of Figures 5-6 (a) through (c) indicates that some contact parameter estimation occurs at many of the time steps. For example, the stiffness estimates (Figure 5-6 (a)) during the first five seconds of the experiment were on the order of 1e9 N/m. However, during a period where there was only one point of contact between the bodies, the stiffness and friction estimates were negative. Figure 5-6 (b) is cropped as some of the damping estimates exceeded 1e6 kg/s. The coefficient of friction estimates over time ranged from being negative to being on the order of 1e3. These results confirm that the multiple point estimation is not working properly for the ACU STVF experiments.

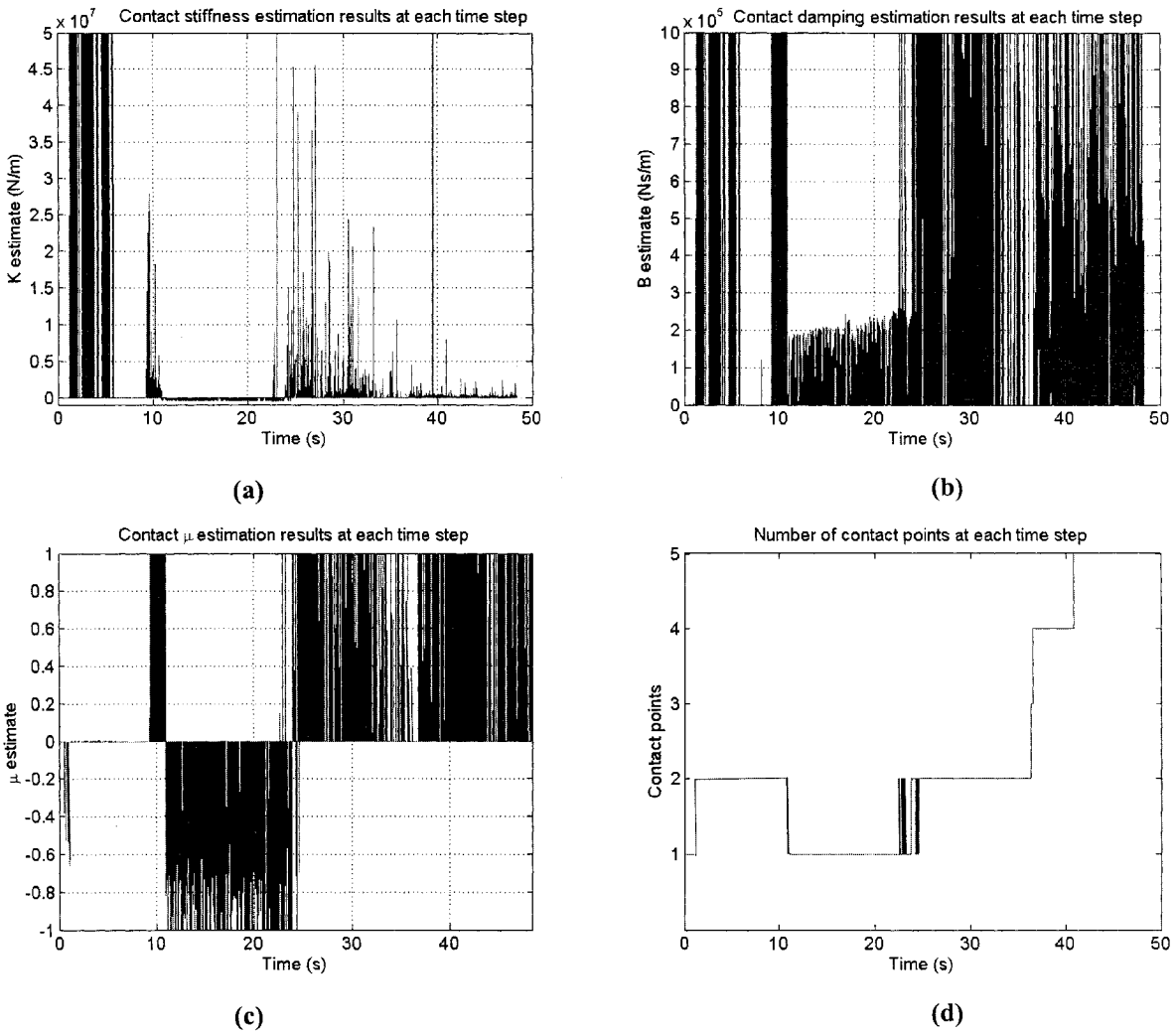

Figure 5-6 Contact parameter estimation results for ACU *Experiment 1a*

Figure 5-6 (d) shows the number of contact points at each instant during the insertion procedure, as determined by *mindist*. At the end of the insertion procedure, it was determined that there were five final contact points, which is a reasonable number considering the construction of the ACU payload and the receptacle. Figure 5-7 shows the location of the final resting points with respect to the location of the v-guides. There is no way to confirm the number and location of the contact points with the ACU experiments. We will see later in this chapter, however, that using simulated experiments, the number of final resting contact points is eight, with two contact points per v-guide. We also note that results for *Experiments 1b, 2a* and *2b* (not shown here) are very similar to those presented here for *Experiment 1a.*

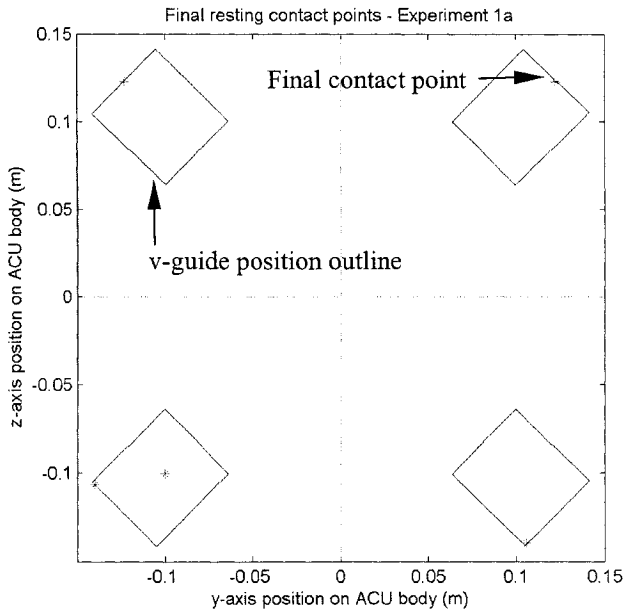

Figure 5-7 Location of final contact points for ACU *Experiment 1a*

5.1.4 Discussion of Results and Estimation Issues

In Chapter 3, we determined that the *Single Point Toolbox* estimates were representative of the stiffness of the entire SMT and payload system due to the nature of the input data. Similarly, the estimation results in this chapter from the *Multiple Point Toolbox* are also representative of contact parameters of a combination of elements. In this case, we can obtain a general idea of an expected stiffness estimate using data from an SMT and ACU experiment different from those used for contact parameter estimation with the toolbox. In this additional SMT and ACU experiment originally described in [41], the STVF manipulator grasped the ACU body by the micro-fixture, inserted the ACU into its receptacle and applied increasing loads. The force plate load data and the end-effector position data from this experiment suggested an effective linear stiffness of the SMT and ACU payload of approximately 1.7e6 N/m [41]. Although this does not represent an estimate for contact stiffness at individual contact points, one might expect the contact stiffness results from the toolbox to be of the same order of magnitude. Comparing these results to those in Table 5-1 clearly shows that the stiffness estimation results are in error by three orders of magnitude.

Furthermore, the poor estimation results for the ACU multiple point contact experiments are not entirely unexpected. In Chapter 3, we became aware that damping estimation would not be possible for the single point contact case, thus we should not expect to obtain reasonable damping estimates for the multiple point contact case. In addition, there are a number of factors related to the experimental facility that could be largely responsible for the estimation difficulties. Uncertainty is present in the following areas:

- As touched upon in Chapter 3, the limited resolution of the end-effector position data (0.2 mm) limits the identification capabilities of the experimental hardware set-up. Small loads and relatively large position inaccuracies are particularly significant in an estimation routine that makes use of interference distances of a very small magnitude at a number of contact points to calculate the contact parameter estimates. This issue is expected to be one of the most significant sources of error.
- The ACU receptacle is assumed to remain stationary in location and orientation during the contact experiments (an assumption that directly affects the *mindist* outputs). However, the receptacle is mounted on the force plate which itself moves during contact experiments. As a result, if the force plate is located or oriented in a manner different from the assumed initial position, the ideal contact point data generated from *mindist* is unlikely to match the contact point data for the real contact bodies. This issue could contribute significant error to the estimation results, as small differences in pose would, like the first issue mentioned, greatly affect an estimation routine that relies on interference distances.
- The *mindist* routine makes use of *.cin* files, which contain information on the geometries of the contacting bodies. These *.cin* files are generated from the manufacturer drawings of the payloads. In reality, the ACU payload and receptacle are constructed from several components screwed together. The v-guide pieces, for example, are screwed to the main ACU body, itself being a composite of four plates. Examination of these components showed that, for example, the v-guides could be moved by a couple of millimeters due to

clearances. The mismatch in actual geometry and the geometry in the *.cin* files can result in significant discrepancies in contact estimation. Also, the *.cin* files assume the v-guides have 'sharp' edges, whereas in reality the v-guide edges are rounded. Again, since we are dealing with very small interference distances for estimation, modest geometric mismatches could significantly affect the estimates.

- As mentioned in Chapter 4, the estimation algorithm in the Multiple Point Toolbox assumes the same contact stiffness, damping and friction at each contact point. Based on the work in Chapter 3, it was determined that different shapes and contacting surfaces result in different contact stiffness estimates. As a result, this assumption in the algorithm may not be suitable for practical multiple point contact experiments. This source of uncertainty, however, is less significant than the previous sources listed here as the results in Chapter 3 showed that stiffness estimates, although different, were mostly of the same order of magnitude for the different shapes.
- The linear model assumed in the toolbox estimation algorithm may not satisfactorily describe the actual physical phenomena of contact. A more complicated model may better describe the contact situation.
- Noisy end-effector position and velocity data can affect the performance of the identification algorithm, as determined in an investigation by Patel [23], where the sensitivity of the estimation algorithm was assessed using 'simulated' noise. It was shown that filtering significantly improves the quality of the stiffness and damping estimates, but not the friction estimates.

To provide some evidence in support of the above hypotheses for poor estimation results for the ACU experiment, in the following section we present a numerical sensitivity study of the contact parameter estimation algorithm. In particular, we address the third item in the above listing: the mismatch between the geometry files and the physical model and its effect on estimation.

5.2 Parameter Estimation with Simulated ACU Insertion

This section begins by describing the simulated ACU insertion scenario. The sensitivity of the estimation algorithm to ACU geometry modifications is then considered.

5.2.1 Simulated ACU Insertion Test Case

In Chapter 4 we mentioned the *ACU Gravity Drop Simulation* as a component of the Multiple Point Toolbox. The toolbox was designed to have an option to deal with this specific test case. The *ACU Gravity Drop Simulation* represents a small drop under gravity of the ACU payload into its stationary receptacle. The ACU payload is initially positioned 5 mm above its receptacle. The simulation runs for 0.4s, allowing the body to settle into the receptacle. In this case, the force exerted by the fixture on the falling ACU is used to emulate the total end-effector force used in the identification procedure described in Chapter 4. No gravity drop experiments were done with the ACU due to an inadequate release mechanism on the robot and to avoid harming the ACU mock-up.

Simulations of this test case carried out within the Multiple Point Toolbox environment require the specification of the contact parameters in the *.ini* files. The performance of the identification algorithm is assessed by comparing the calculated contact parameters with those specified as inputs to the simulation. The particular values for contact parameters used in the present study are:

- stiffness, $k = 1e5$ N/m
- damping, $b = 38.37$ kg/s
- coefficient of friction, $\mu = 0.10$

Note that the stiffness used in these simulations is likely lower than the expected contact stiffness for the real ACU.

5.2.2 ACU Payload Model Geometry Modifications

In Chapter 4, it was explained that a *.cin* file, containing the geometric data of the contacting bodies, is required as input into the Multiple Point Toolbox for contact

parameter estimation. For the ACU and receptacle, the *.cin* files were generated with software programs 3D Studio Max and CD Modeller using data from the CAD drawings. The Multiple Point Toolbox (and CDT) expects that the contacting bodies be described using convex shapes. In the case of the ACU and receptacle, both bodies are described as a combination of several sub-bodies constructed solely from planes.

Figures 5-8 (a) and (b) show the ACU payload and receptacle as defined by the *.cin* geometry files. In Figure 5-8 (a), the ACU and receptacle are shown together in their inserted position. Figure 5-8 (b) shows that the ACU payload is a composite of five sub-bodies. These sub-bodies include a main 'box' and four 'tent-shaped' v-guides.

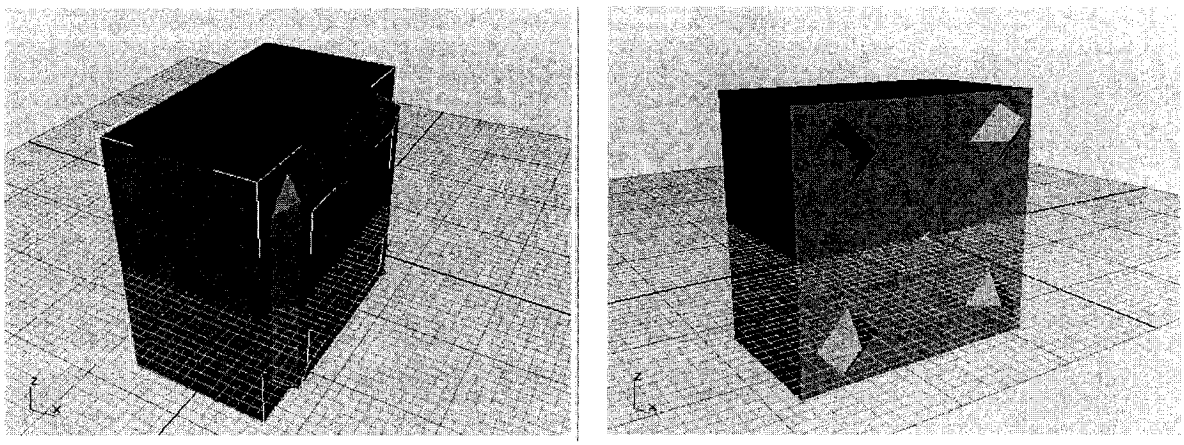

(a) (b)

Figure 5-8 Geometric models of ACU mated with its receptacle (a) and ACU alone (b)

The physical construction of the ACU was based on the same CAD drawings that were used to generate the *.cin* files. Inspection of the physical ACU unit revealed that some of the dimensions and sizing of the actual ACU differ marginally from the original specifications. This slight mismatch between CAD specifications and the physical model imply that there would be a difference between the physical model and the *.cin* geometry specifications.

For the investigation here, emphasis is placed primarily on the v-guide dimensions and positioning, as contact between the two bodies occurs almost exclusively between the v-guides and their mating berths. Investigation of the physical ACU and its receptacle showed that some of the v-guide dimensions are in error by one or two millimeters from

their expected dimensions. The position of the v-guides on the ACU body was also determined to be variable due to the nature of the construction of the ACU and its receptacle. The v-guides are screwed to the main surface of the ACU 'box', but due to relatively generous clearance in the attachment holes, the position and orientation of the v-guides can be adjusted by loosening the screws, shifting the body and re-tightening the screws. As such, the v-guides can be easily shifted by one mm and rotated slightly.

V-Guide Modification Definition

Here we label the v-guide sub-bodies and outline the proposed v-guide geometry modifications used in this simulation study. Figure 5-9 shows a 'bottom-up' view of the ACU body, and the numbering system assigned to the four v-guides for our research. Subsequent result tables will refer to the v-guides according to this numbering guideline.

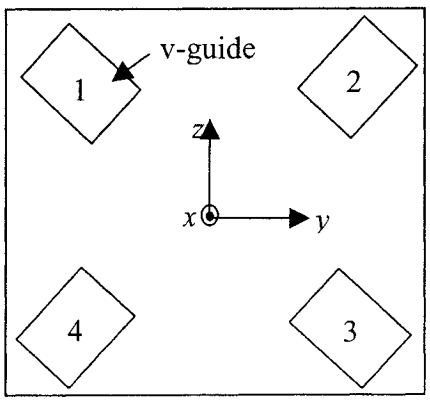

Figure 5-9 ACU v-guide numbering guideline

Figure 5-10 depicts the type of modifications that are considered for the ACU v-guides in the present investigation. In particular, position shifts (forward, backwards and sideways), size increases and rotations of the v-guide sub-bodies were considered. In Figure 5-10, the shape drawn with the solid line represents the original v-guide position or size (v-guide 1, for example), while the proposed modification is shown with the

dotted line. Subsequent discussion identifies the v-guide modifications using the names listed below each of the figures.

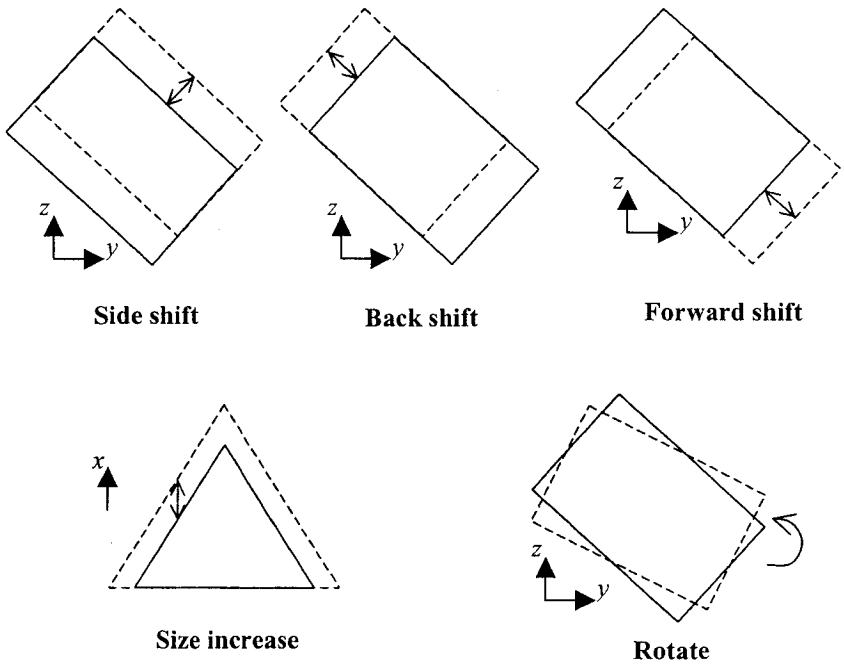

Figure 5-10 ACU v-guide geometry modifications

The *side*, *back* and *forward* shifts use the original centre line of the v-guide sub-body as the reference for what direction is implied by *side*, *back* and *forward*. For example, a *forward* shift of a v-guide implies shifting the body closer to the centre point of the ACU, along the original centre line of the v-guide.

Sensitivity Analysis Procedure

The first step in the procedure for assessing the estimation algorithm sensitivity to geometry mismatches involves determining a method by which to modify the *.cin* files. To generate the changes in the geometry files, the planes describing the v-guide sub-bodies of the ACU had to be redefined. A Matlab script was created to automatically generate *.cin* files allowing the user to specify the desired geometry modifications, in agreement with those defined in Figure 5-10. Figures 5-11 (a) and (b) show a modified

ACU model where exaggerated changes (for ease of viewing) in v-guide size, location and orientation have been made.

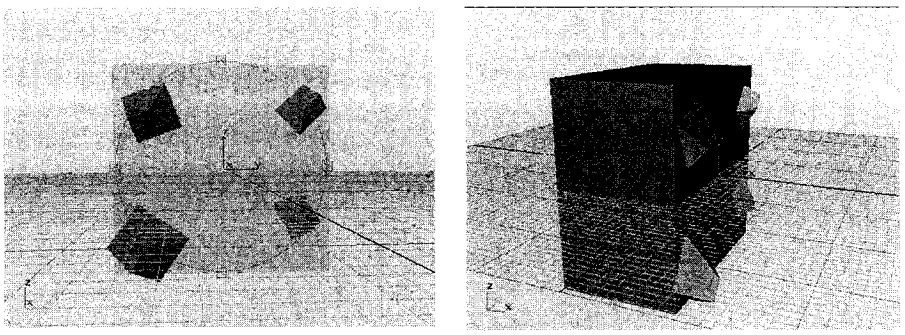

(a) (b)

Figure 5-11 ACU geometric model with exaggerated v-guide modifications

To assess the effect of using a modified geometry file on contact parameter estimation, we use the load data from an *unmodified* geometry ACU gravity drop simulation together with the contact point data associated with the *modified .cin* file in the estimation algorithm. The modified contact point data is determined using the *mindist* routine with the original payload trajectory. This process is expressed graphically in Figure 5-12.

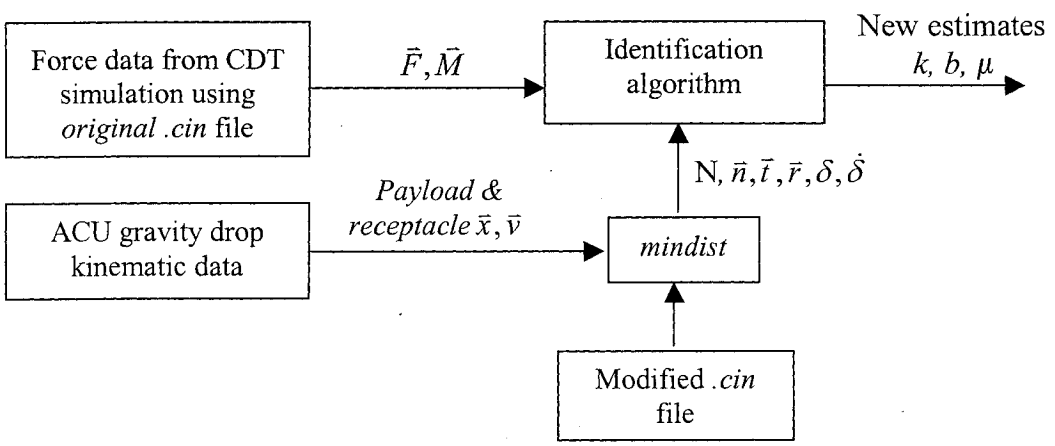

Figure 5-12 Procedure for assessing estimation algorithm sensitivity to geometry changes

5.2.3 ACU Gravity Drop Simulation Estimation Results with Modified Geometry

We begin by presenting the estimation results for the ACU gravity drop when *no* modifications to the geometry files are made. In this case, we expect the contact parameters estimated with the Multiple Point Toolbox to come very close to the values specified as inputs to the simulation. Figure 5-13 (a) shows the number of contact points at each time instant, while Figure 5-13 (b) shows the z-coordinate of the falling ACU. Figures 5-13 (c) through (e) show the time history of the contact stiffness, damping and coefficient of friction parameter estimates. Figure 5-13 (f) shows the location of the final eight resting points of the ACU body after it has settled into its receptacle. The first line in Table 5-2 specifies the input contact parameters, while the second line presents the global least squares calculated estimates for this unmodified simulation case. The discrepancies between these are in accordance with previously obtained results for a slightly different ORU test case [23].

We also present a summary of the global least squares estimates obtained for different geometry modifications to the ACU. In particular, Table 5-2 presents a selection of estimation results where only one v-guide, in this case v-guide 1, has been modified. Table 5-3 presents some representative results when all four v-guides underwent the same modification, along with a couple results for random modifications to all four v-guides. The modifications listed in these tables are representative of plausible geometry mismatches between the actual ACU payload and its *.cin* geometry definition file.

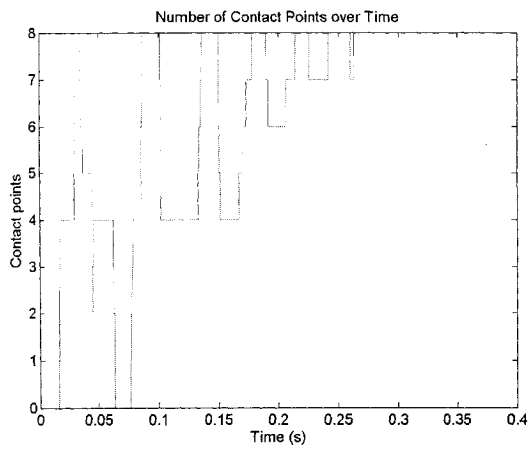

(a)

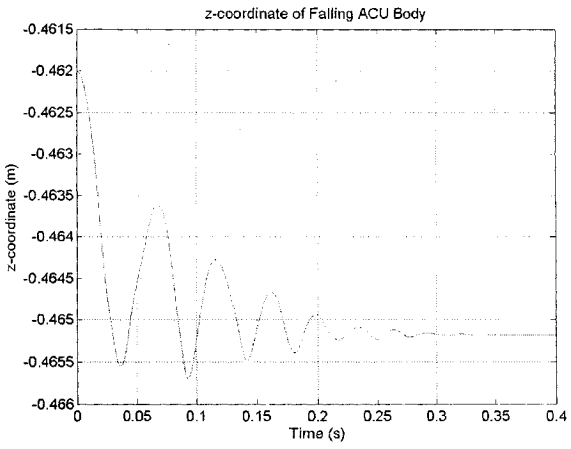

(b)

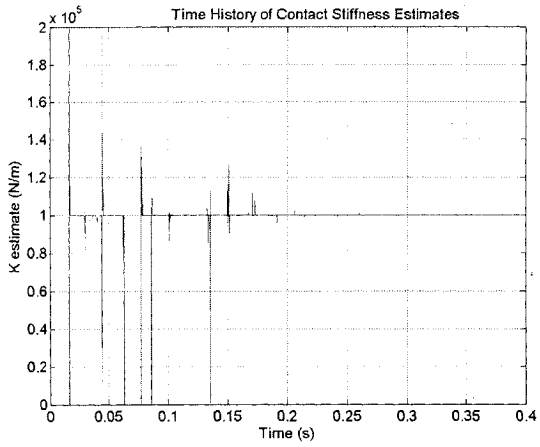

(c)

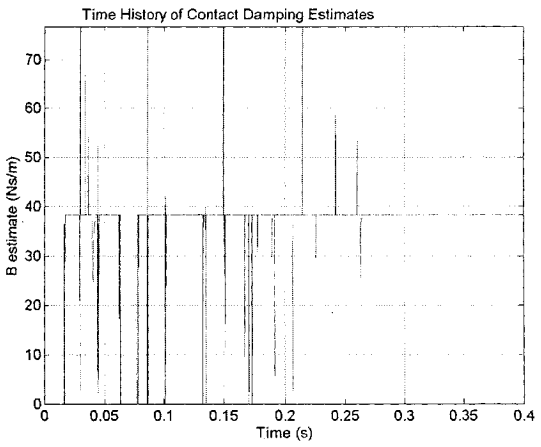

(d)

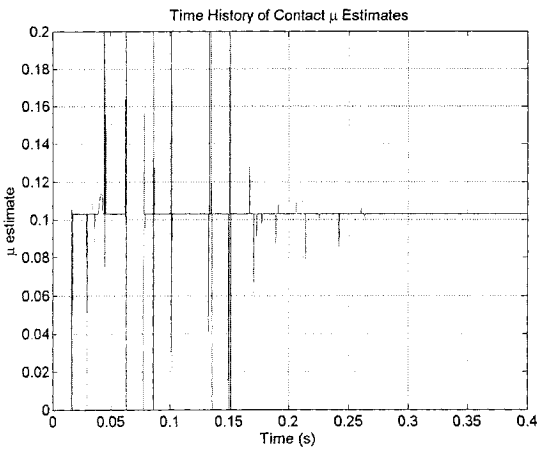

(e)

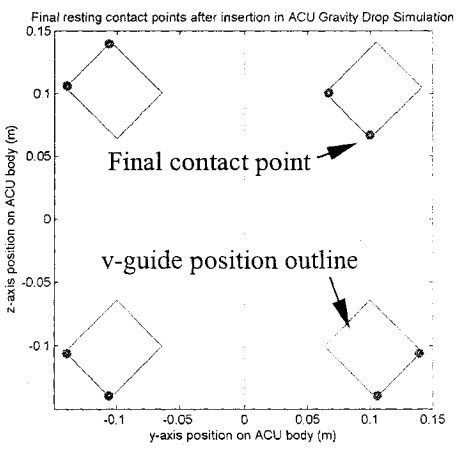

(f)

Figure 5-13 Parameter estimation results for ACU gravity drop - no geometry modifications

Table 5-2 ACU simulation contact parameter estimates - v-guide 1 modifications

Modification	Stiffness		Damping		Coeff. of Friction	
	Value (N/m)	Error (%)	Value (kg/s)	Error (%)	Value (N/m)	Error (%)
Input parameter values	100000.0	--	38.37	--	0.1000	--
No geometry modifications	99992.7	0.01	37.54	2.16	0.1028	2.80
v-guide 1: 1e-3 m back shift	99984.3	0.02	37.4	2.48	0.1029	2.94
v-guide 1: 2e-3 m back shift	100004	0.00	37.48	2.31	0.1029	2.88
v-guide 1: 5e-3 m back shift	100061.0	0.06	37.63	1.92	0.1027	2.72
v-guide 1: 1e-6 m forward shift	99992.6	0.01	37.54	2.16	0.1028	2.80
v-guide 1: 1e-5 m forward shift	99996.1	0.00	37.54	2.15	0.1028	2.80
v-guide 1: 1e-4 m forward shift	100047.0	0.05	37.55	2.13	0.1026	2.65
v-guide 1: 3e-4 m forward shift	100435.0	0.44	36.05	6.03	0.0961	3.86
v-guide 1: 6e-4 m forward shift	98779.9	1.22	33.60	12.43	0.1080	8.03
v-guide 1: 1e-3 m forward shift	91641.5	8.36	31.10	18.94	0.1028	2.77
v-guide 1: 2e-3 m forward shift	61565.7	38.43	33.47	12.77	0.1190	18.95
v-guide 1: 3e-3 m forward shift	43298.5	56.70	32.49	15.32	0.1206	20.62
v-guide 1: 1e-6 m side shift	99988.9	0.01	37.50	2.26	0.1028	2.82
v-guide 1: 1e-5 m side shift	99943.2	0.06	37.12	3.26	0.1029	2.85
v-guide 1: 1e-4 m side shift	98825.8	1.17	34.29	10.62	0.1026	2.60
v-guide 1: 1e-3 m side shift	65561.1	34.44	29.03	24.34	0.0697	30.31
v-guide 1: 1 deg rotation	70606.4	29.39	35.99	6.19	0.0670	33.04
v-guide 1: 2 deg rotation	52173.9	47.83	38.02	0.90	0.0500	49.98
v-guide 1: 5 deg rotation	24710.8	75.29	45.42	18.39	0.0160	84.04
v-guide 1: 1e-3 m size increase	50135.6	49.86	36.58	4.67	0.0447	55.28
v-guide 1: 2e-3 m size increase	29421.5	70.58	42.94	11.91	0.0137	86.32

Table 5-2 indicates that back shifting v-guide 1 had little effect on estimation. Forward shifting of v-guide 1 begins to become important once it has been moved by at least 1 mm. However, in the most extreme (and more unlikely) case of forward shifting the v-guide (3 mm) resulted in a maximum error of 57% in stiffness estimation. Modest rotations and size increases of the v-guides cause significant error in the stiffness and friction estimation, with 1 – 2° rotations and 1 – 2 mm size increases causing errors of one order of magnitude. Damping estimation was less affected by geometry mismatches of one v-guide.

The results in Table 5-3 further indicate that minor differences in payload and geometry file definition can create large parameter estimation errors. As expected, moving all of the ACU v-guides had a greater impact on estimation than moving just one v-guide. Back shifting all v-guides over a range of 1 mm to 5 mm showed little effect on estimation. This result makes sense as no interference or major change is introduced into the manner in which the v-guide and its mating guide fit together – the v-guide merely contacts the mating guide further back.

Forward shifting of all v-guides is expected to present greater problems in estimation. Friction estimation begins to become significantly affected once the v-guides are shifted forward by only 0.3 mm, with an error greater than 44%. Damping estimation shows significant error in the estimates once the v-guides are moved by 0.6 mm. Stiffness estimation begins to deteriorate with a 1 mm forward shift of all the v-guides, showing an error of one order of magnitude.

Side shifting of all v-guides is also expected to present estimation problems. In Table 5-3, estimation of the contact parameters is successful for all side shifts of 0.1 mm and less, with the exception of the damping estimate deteriorating at 0.1 mm (39% error). Side shifts of 1 mm precluded damping estimation and introduced a large error (62%) into the stiffness estimate.

Table 5-3 ACU simulation contact parameter estimates – modifications for all v-guides

Modification	Stiffness		Damping		Coeff. of Friction	
	Value (N/m)	Error (%)	Value (kg/s)	Error (%)	Value (N/m)	Error (%)
Input parameter values	100000.0	--	38.37	--	0.1000	--
No geometry modifications	99992.7	0.01	37.54	2.16	0.1028	2.80
All v-guides: 1e-3 m back shift	100037.0	0.04	36.97	3.64	0.1029	2.86
All v-guides: 2e-3 m back shift	100127.0	0.13	37.12	3.25	0.1027	2.70
All v-guides: 5e-3 m back shift	100365.0	0.37	37.87	1.28	0.1018	1.85
All v-guides: 1e-6 m forward shift	99992.6	0.01	37.54	2.16	0.1028	2.80
All v-guides: 1e-5 m forward shift	99996.9	0.00	37.57	2.08	0.1028	2.81
All v-guides: 1e-4 m forward shift	100112.0	0.11	37.72	1.69	0.1020	1.99
All v-guides: 3e-4 m forward shift	101895.0	1.90	35.18	8.29	0.1444	44.39
All v-guides: 6e-4 m forward shift	96536.3	3.46	20.80	45.79	0.1889	88.94
All v-guides: 1e-3 m forward shift	76498.9	23.50	12.97	66.19	0.1178	17.79
All v-guides: 2e-3 m forward shift	30795.7	69.20	32.17	16.15	0.0773	22.70
All v-guides: 3e-3 m forward shift	18313.3	81.69	27.76	27.64	0.0766	23.45
All v-guides: 1e-6 m side shift	99968.8	0.03	37.40	2.51	0.1028	2.81
All v-guides: 1e-5 m side shift	99742.5	0.26	36.22	5.61	0.1028	2.77
All v-guides: 1e-4 m side shift	96226.0	3.77	23.39	39.03	0.1001	0.15
All v-guides: 1e-3 m side shift	37870.4	62.13	0.00	100.00	0.0997	0.35
All v-guides: 1 deg rotation	37741.2	62.26	34.90	9.03	0.0333	66.66
All v-guides: 2 deg rotation	21983.8	78.02	32.51	15.26	0.0226	77.39
All v-guides: 5 deg rotation	8199.7	91.80	33.15	13.60	0.0000	100.00
All v-guides: 1e-3 m size increase	19837.4	80.16	29.38	23.41	0.0557	44.35
All v-guides: 2e-3 m size increase	9368.0	90.63	34.88	9.08	0.0000	100.00
Random v-guide modifications[5]	126422	26.42	60.13	56.73	0.0151	84.93
Random v-guide modifications[6]	201599	101.60	0.05	99.88	0.0469	53.08

In particular, these results show that rotational misalignments and size discrepancies of 1-2° and 1 - 2 mm, respectively, result in stiffness and friction estimates an order of magnitude in error. The last two lines of Table 5-3 give two examples of random modifications to the four v-guides. The second case, in particular, demonstrates the

[5] v-guide 1 (1 deg. rot.), v-guide 2 (1 mm side shift), v-guide 3 (1 mm for. shift), v-guide 4 (2 mm size inc.)
[6] v-guide 1 (1 deg. rot., 1 mm for. shift), v-guide 2 (1 mm side shift), v-guide 3 (1 deg. rot., 1 mm for. shift), v-guide 4 (1 mm size inc. & side shift)

significant effect that geometry mismatches can have on the estimation of each of the contact parameters.

In summary, mismatches between the physical unit and the geometry file can create significant errors in the estimation results for the ACU experimental case. Despite the mismatches, however, estimation was still mostly possible (i.e. there were no '0' estimates for the parameters, with the exception of one case in damping estimation). From this observation, we can conclude that geometry mismatches, though introducing significant error in some scenarios, do not fully explain the inability to obtain damping and friction estimates from our ACU experimental data. The remaining sources of error identified in Section 5.1.4, which we have not quantified here, are thus assumed to be the cause of being unable to identify *any* damping and friction estimates in experimentation. Geometry mismatches do, however, explain a large part of the error in the experimental stiffness estimation results, though it is expected that the other sources of error also contribute.

Chapter 6

Conclusions and Recommendations

The primary objectives of this research were:

1. to develop a user-friendly Single Point Toolbox incorporating nine time- and frequency-domain single point contact parameter estimation algorithms;
2. to validate and use the Single Point Toolbox with STVF contact experiments, having stiff environments and payloads;
3. to determine the feasibility of estimating payload stiffness using experimental data from the SMT facility at the Canadian Space Agency;
4. to develop a user-friendly Multiple Point Toolbox based upon the previously developed multiple contact parameter estimation algorithm;
5. to use the Multiple Point Toolbox to perform multiple point contact parameter estimation for SMT experiments with an ACU payload.

6.1 Summary

In Chapter 2 the development of the Single Point Toolbox containing nine parameter estimation algorithms for the single point contact problem was presented. The estimation algorithms included both time- and frequency-domain algorithms. The functionality of the toolbox was described and screen shots of the final product were presented.

Chapter 3 presented details on CSA's SMT facility and described the six payloads used in a series of single point contact experiments. Results of contact stiffness and damping estimation for the SMT and payload system were given for each of the nine estimation algorithms in the Single Point Toolbox. The stiffness of the SMT without a payload was determined through independent experiments. This result was used with the combined

SMT and payload stiffness results from the toolbox to calculate the stiffness of the payloads. Instron experiments provided independent values for payload stiffness. The Instron linear stiffness estimates were used to assess the success of estimating payload stiffness using the SMT experiments. A number of limitations and sources of error in the results were discussed.

In Chapter 4 the development of the Multiple Point Toolbox was presented. A description was provided of the contact model and the contact parameter estimation algorithm for complex contacting geometries. This was followed by a discussion of the integration of the algorithm into a user-friendly toolbox. Details on the functionality incorporated into the toolbox were given, along with screenshots of the final product.

Chapter 5 presented contact parameter estimation results generated by the Multiple Point Toolbox for SMT ACU insertion experiments. Sources of uncertainty and error for the estimation results were identified. The sensitivity of the identification algorithm to geometry mismatches between the ACU unit and its geometry file definition were investigated by using the simulated gravity drop test.

6.2 Results

The Single Point Toolbox was employed in Chapter 3 to process data from STVF experiments with six different payloads. During this process, the toolbox was used comprehensively and many of the error-checking features were validated. Single Point Toolbox estimation results from the SMT contact experiments showed that the nine algorithms provide consistent stiffness estimates. The contact damping estimates generated from the transient phases of contact were inconsistent between the algorithms and in many cases obviously incorrect. The Kalman Filter algorithm was the only one to produce "believable" damping estimates.

In addressing the goal of using the SMT to determine payload stiffness, the experimental facility was modelled as a simple series of linear springs. It was determined that the toolbox estimates were representative of the parameters for the combined SMT and

payload system. Under this assumption, stiffness estimates for the SMT and payload combination, along with stiffness estimates for the SMT alone, were used to calculate the payload stiffness, k_{calc}. In particular, STVF experiments without payloads showed that the combined stiffness of the robot and the force plate (SMT) is approximately 3.5e6 N/m. With the stiffness estimates obtained for the STVF/payload system, the calculated payload stiffness values varied from 4.8e5 N/m for the plastic cube to 2.5e7 N/m for the aluminum half-sphere.

Independent testing of the payloads with an Instron machine indicated a non-linear relationship between the contact load and the deformation for all considered payloads. The aluminum half-sphere was observed to be the stiffest payload, followed by the plastic cube, prism, half-sphere, cone and pyramid. Linear (secant) stiffness estimates for the payloads were determined from the non-linear relationship and were varying from 1.2e6 N/m for the plastic pyramid to 1.2e7 N/m for the aluminum half-sphere.

Comparing the independently determined $k_{payload}$ stiffness estimates with the calculated payload stiffness estimates, k_{calc}, revealed that some payload stiffness estimation was possible using SMT experiments. The aluminum half-sphere stiffness estimates showed a wide range of error, spanning from less than 1% to more than 100%. Plastic half-sphere stiffness estimation was more successful, with stiffness estimation errors ranging from 2% to 38%. Stiffness estimation errors for the plastic cone and pyramid ranged from 18% to 41% while the errors for the plastic prism and cube ranged from 58 – 95%. The error analysis indicated that the errors in estimation results were dominated by the resolution of the end-effector position.

The Multiple Point Toolbox was used extensively for the work in Chapter 5. Several of the features of the toolbox were tested and validated through this comprehensive use. Additional error checking opportunities were identified and implemented, improving the robustness of the toolbox.

The Multiple Point Toolbox generated some contact parameter estimates for SMT ACU insertion experiments. While contact stiffness estimates were determined for three of the four ACU experiments, the identification algorithm failed to provide any estimate for contact damping and friction. Contact stiffness estimates ranged from 1141 N/m to 3918 N/m. It was determined that the toolbox contact stiffness estimates for ACU insertion experiments were in error by three orders of magnitude. The toolbox predicted that at the conclusion of insertion the ACU was in contact with its receptacle at five contact points, this deemed a reasonable number.

Several sources of error explaining the inability to determine reasonable contact parameter estimates from the ACU insertion experiments were identified. The primary errors include: limited resolution of the experimental hardware, mismatches between actual payload geometry and the payload geometry used in the calculation of contact kinematics, and uncertainty in the pose of the force plate upon which the ACU receptacle rests. Secondary sources of error are the assumption that the contact parameters are identical at all contact points, and the differences between the actual physical phenomena occurring and those expected by the linear contact model assumed. The specific issue of mismatching geometry was investigated as to how it affects the quality of estimation for complex contact geometries. The results from this sensitivity study demonstrated that small payload geometry mismatches can have a substantial effect on stiffness and friction estimation, with estimates an order of magnitude in error. Though large estimation errors were present in the sensitivity study, some estimation was possible, indicating that geometry mismatches on their own do not explain why at least friction estimates from ACU insertion experiments could not be found. These results did provide some explanation for the poor stiffness estimates from the ACU insertion experiments.

6.3 Recommendations for Further Research

Based on the work presented in this thesis, several areas of focus for future research can be suggested. These include:

- Further validation of the Multiple Point Toolbox estimation algorithm with experimental data is recommended. An attempt should be made to address the

primary sources of error in the ACU experiments to diminish their effect on the quality of estimation.

- In light of the observation of non-linear stiffness behaviour of the simple geometry payloads, research into non-linear contact models and corresponding parameter estimation algorithms is desirable for improved application to practical situations.
- Further attention should be given to addressing the principal sources of error and issues identified during the parameter estimation procedure for simple geometry payloads. In this respect, some of the future work could include:
    - investigation into the questionable experimental results for the plastic cube and plastic prism payloads;
    - addressing the uncertainty corresponding to the use of linear 'secant' stiffness approximations for the payloads;
    - developing reliable ABAQUS/FEA models to obtain stiffness characteristics for all payloads.

References

[1] P. Eykhoff, *System Identification: Parameter and State Estimation.* Toronto: John Wiley & Sons, 1974.

[2] K. W. Lo, B. G. Ferguson, Y. Gao and A. Maguer, "Aircraft Flight Parameter Estimation Using Acoustic Multipath Delays," *IEEE Transactions On Aerospace And Elecronic Systems*, vol. 39, no. 1, pp. 259-268, January 2003.

[3] H. Roux, D. Raclot, D. Dartus and C. Puech, "Hydraulic Parameter Identification using Aerial Photographs," in *IEEE Proc. Geoscience and Remote Sensing Symposium (IGARSS '03)*, vol. 2, 21-25 July 2003, pp. 1172-1174.

[4] J. O. Hahn and R. Rajamani, "GPS-Based Real-Time Identification of Tire-Road Friction Coefficient," *IEEE Transactions on Control Systems Technology*, vol. 10, no. 3, pp. 331-343, May 2002.

[5] J.O. Hahn, R. Rajamani, S.H. You and K.I. Lee, "Real-Time Identification of Road-Bank Angle Using Differential GPS," *IEEE Transactions on Control Systems Technology*, vol. 12, no. 4, pp. 589-599, July 2004.

[6] J. Wang, J. D. Wang, N. Daw and Q.H. Wu, "Identification of Pneumatic Cylinder Friction Parameters Using Genetic Algorithms," *IEEE/ASME Transactions on Mechatronics*, vol. 9, no. 1, pp. 100-107, March 2004.

[7] H. B. Karayaka, A. Keyhani, G. T. Heydt, B. L. Agrawal and D. A. Selin, "Synchronous Generator Model Identification and Parameter Estimation From Operating Data," *IEEE Transactions on Energy Conversion*, vol. 18, no. 1, pp. 121-126, March 2003.

[8] J. W. Kim, S. J. Kim and S. W. Kim, "Parameter Identification of Induction Motors Using Dynamic Encoding Algorithm for Searches (DEAS)," in *IEEE Proc. Industrial Electronics Society IECON*, vol. 1, 2-6 Nov. 2003, pp. 150-155.

[9] Y. Li, Y. Liu, X. Liu and Peng, Z. "Parameters Identification and Vibration Control for Modular Manipulators," in *Proc. of the 2003 IEEE International Conference on Robotics and Automation*, 14-19 September, 2003, Taipei, Taiwan.

[10] T. Lefebrve, H. Bruyninckx and J. De Schutter, "Active Sensing for the Identification of Geometrical Parameters during Autonomous Compliant Motion," in *Proc. of the 2003 IEEE International Conference on Robotics and Automation*, 14-19 September, 2003, Taipei, Taiwan.

[11] J. De Carufel, E. Martin and J.-C. Piedbouf, "Control Strategies for Hardware-in-the-loop Simulation of Flexible Space Robots," *IEE Proceedings on Control Theory Applications*, vol. 147, no. 6, pp. 569-579, November 2000.

[12] I. Han and B. J. Gilmore, "Multi-Body Impact Motion with Friction Analysis, Simulation and Experimental Validation," *Journal of Mechanical Design*, vol. 115, pp. 412-422, 1993.

[13] Y. Hurmuzlu and D. B. Marghitu, "Rigid Body Collision of Planar Kinematic Chains with Multiple Contact Points," *The International Journal of Robotics Research*, vol. 13, no. 1, pp. 82-92, 1994.

[14] O. Ma, K. Buhariwala, N. Roger, J. MacLean and R. Carr,. "MDSF: A Generic Development and Simulation Facility for Flexible, Complex Robotic Systems," *Robotica*, vol. 15, pp. 49-62, 1997.

[15] M. K. Vukobratovic and V. Potkonjak, "Dynamics of Contact Tasks in Robotics. Part I: General Model of Robot Interacting with Environment," *Mechanism and Machine Theory*, vol. 34, pp. 923-942, 1999.

[16] G. Gilardi and I. Sharf, "Literature Survey of Contact Dynamics Modelling," *Journal of Mechanism and Machine Theory*, vol. 37, pp. 1213-1239, 2002.

[17] S. Singh and D. Popa, "An analysis of some fundamental problems in adaptive control of force and impedance behavior: Theory and Experiments," *IEEE Transactions on Robotics and Automation*, vol. 11, no. 6, pp. 912-921, 1995.

[18] H. Seraji and R. Colbaugh, "Force Tracking in Impedence Control," *The International Journal of Robotic Research*, vol. 16, issue 1, pp. 97-117, 1997.

[19] D. Erickson, "Contact Stiffness and Damping Estimation for Constrained Robotic Systems," Master's thesis, University of Victoria, Victoria, Canada, 2000.

[20] L. Love and W. Book, "Environment estimation for enhanced impedance control," in *Proc. of the IEEE International Conference on Robotics and Automation*, pp. 1854-1859, 1995.

[21] D. Erickson, M. Weber and I. Sharf, "Contact Stiffness and Damping Estimation for Robotic Systems," *International Journal of Robotics Research*, vol. 22, no. 1, pp. 41-47, 2003.

[22] M. Weber, "Contact Parameter Identification for Constrained Robotic Tasks with Known Geometry," Master's thesis, University of Applied Sciences FH Ravensburg-Weingarten, 2001.

[23] K. Patel, "Frequency and Time Domain Contact Parameter Estimation for Space Robotic Operations," Master's thesis, McGill University, 2003.

[24] I. Sharf, G. Gilardi and C. Crawford, "Identification of Friction Coefficient for Constrained Robotic Tasks," *Journal of Dynamics Systems, Measurement, and Control*, ASME, Vol. 124, pp. 529-538, 2002.

[25] M. Weber, O. Ma and I. Sharf, "Identification of Contact Dynamics Model parameters from constrained robotic operations," *ASME 2002 Design Engineering Technical Conferences and Computers and Information in Engineering Conference*, 2002.

[26] L. Ljung, *System Identification: Theory for the user.* Englewood Cliffs, NJ: Prentice-Hall, 1987.

[27] J.J. Slotine and W. Li, *Applied Nonlinear Control.* Englewood Cliffs, NJ: Prentice-Hall, 1987.

[28] K. Ogata, *Discrete-Time Control Systems.* Englewood Cliffs, NJ: Prentice-Hall, 1987.

[29] R. G. Brown and P. Y. C. Hwang, *Introduction to Random Signals and Applied Kalman Filtering.* New York, NY: John Wiley and Sons, Inc., 1997.

[30] R. Pintelon and J. Schoukens, *Systems Identification, A Frequency Domain Approach.* New York: IEEE Press, The Institute of Electrical and Electronics Engineers, Inc., 2001.

[31] G. Gopalratnam and J. Raol, "Analysis of Stabilised Output Error Methods," *IEE Proceedings – Control Theory Applied*, vol. 143, no. 2, pp. 209-216, March 1996.

[32] N. Sinha and B. Kutsza, *Modeling and Identification of Dynamics Systems*. Van Nostrand Reinhold, April, 1983.

[33] H. Dai and N. Sinha, "A Robust Off-line Output Error Method for System Identification," *IEEE Transactions on Industrial Electronics*, vol. 39, no. 4, August 1992.

[34] J. Mendel, *Discrete Techniques for Parameter Estimation – The Equation Error Formulation*. New York: Marcel Dekker Inc., 1973.

[35] E. Morelli, "Real-Time Parameter Estimation in the Frequency Domain," *American Institute of Aeronautics and Astronautics*, pp. 1-11, 99-4043, 1999.

[36] V. Klein, "Aircraft Parameter Estimation in Frequency Domain," *American Institute of Aeronautics and Astronautics*, pp. 140-147, 78-1344, 1978.

[37] R. Mehra, "Synthesis of Optimal Inputs for Multi-input/Multi-output (MIMO) Systems With Process Noise," *System Identification: Advances and Case Studies*, edited by Mehra, R. and Lainiotis, D. Academic Press, 1976.

[38] J.-C. Piedboeuf, J. de Carufel, F. Aghili and E. Dupuis, "Task Verification Facility for the Canadian Special Purpose Dextrous Manipulator," in *Proc. of the 1999 IEEE International Conference on Robotics and Automation*, vol. 2, Detroit, Michigan, 10-15 May 1999, pp. 1077-1083.

[39] O. Ma, J. Wang, S. Misra and M. Liu, "On the validation of SPDM Task Verification Facility," *Journal of Robotic Systems*, vol. 21, no. 5, pp. 219-235, 2004.

[40] W. Zhu, J.-C. Piedboeuf and Y. Gonthier, "Emulation of a Space Robot using a Hydraulic Manipulator on the Ground," in *Proc. of the 2002 IEEE International Conference on Robotics and Automation*, Washington, D.C. May 2002.

[41] C. Lange and Y. Gonthier, "Experimental contact parameter estimation using a 6-DOF robot," in *Proc. of the 15th CISM-IFToMM Symposium on Robotics Design, Dynamics and Control (Romansy 2004)*, Montreal, Canada, June 2004

[42] H. D. Conway and K. A. Farnham, "The Relationship Between Load and Penetration for a Rigid, Flat-Ended Punch of Arbitrary Cross Section," *International Journal of Engineering Science*, vol. 6, pp. 489-496, 1968.

[43] C. E. Truman, A. Sackfield and D. A. Hills, "Contact Mechanics of Wedge and Cone Indenters," *International Journal of Mechanical Science*, vol. 37, no. 3, pp. 261-275, 1995.

[44] K. L. Johnson, *Contact Mechanics*. Cambridge, U.K.: Cambridge University Press, 1985.

[45] A. C. Fischer-Cripps, *Introduction to Contact Mechanics*. New York: Springer-Verlag New York Inc., 2000.

[46] B J. Brinkworth, *An Introduction to Experimentation*. New York: American Elsevier Publishing Company, Inc., 1968.

[47] J. Van Vliet, I. Sharf and O. Ma. "Experimental Validation of Contact Dynamics Simulation of Constrained Robotic Tasks," *International Journal of Robotics Research*, vol. 19, no. 12, pp. 1203-1217, December 2000.

[48] O. Ma, "Contact Dynamics Toolkit (CDT) User's Guide," Version CDT_98, Release 4, Document MDSAR TN. R&D-1999.93, Macdonald Dettwiler Space and Advanced Robotics Ltd., Ontario, Canada, 1999.

[49] M. Nahon, "Determination of the Interference Distance between Two Objects using Optimization Techniques," in *Proc. of the 1994 ASME Design Automation Conference*, vol. 69-1, pp. 1-6, Delaware, 1994.

Appendix A Payload specifications

Included in this appendix are the technical construction details for the contact specimens (payloads) of Chapter 3. The drawings were made in AutoCAD LT 2000 (Educational version). Employees of the Canadian Space Agency manufactured the pieces from aluminum (6061) and plastic (Acetron GP Acetal) in their on-site machine shop.

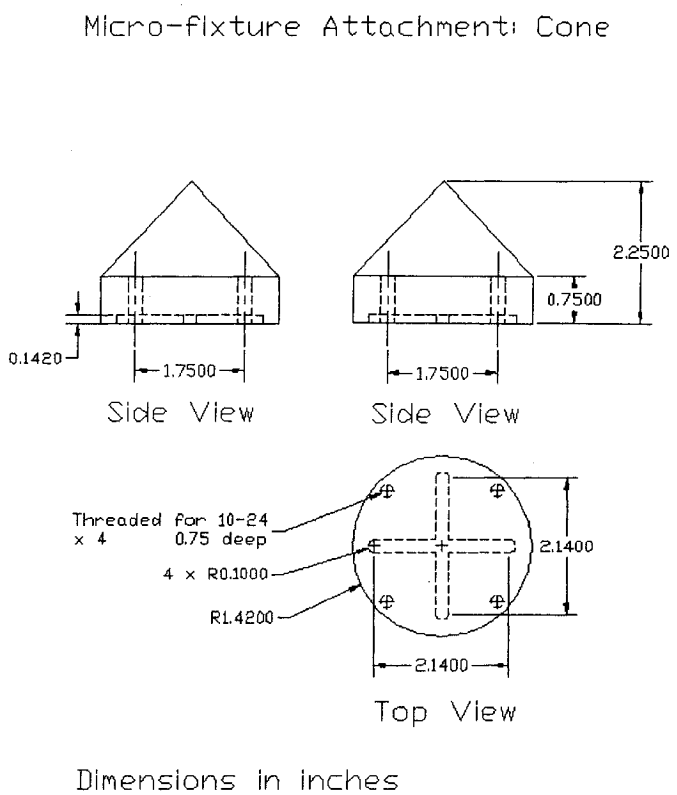

Figure A-1 Payload specifications: cone

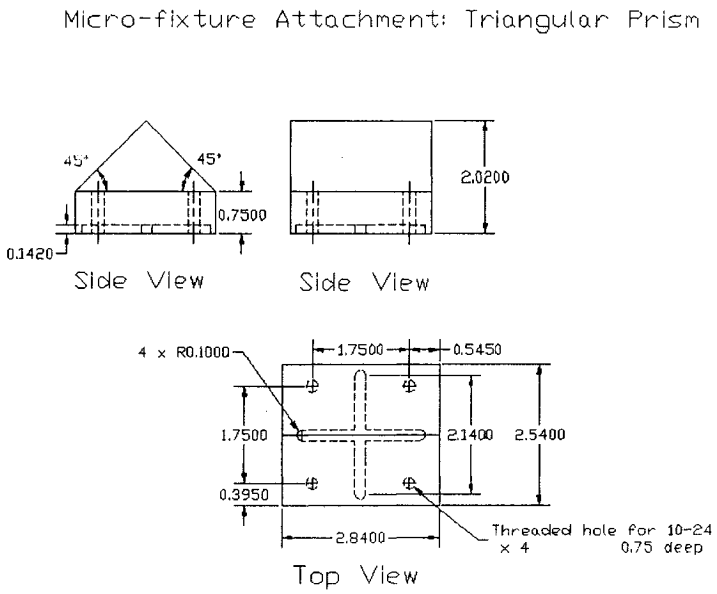

Figure A-2 Payload specifications: triangular prism

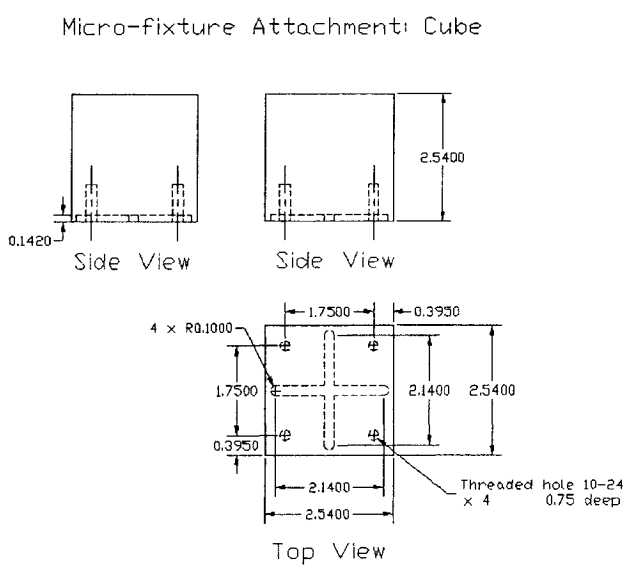

Figure A-3 Payload specifications: cube

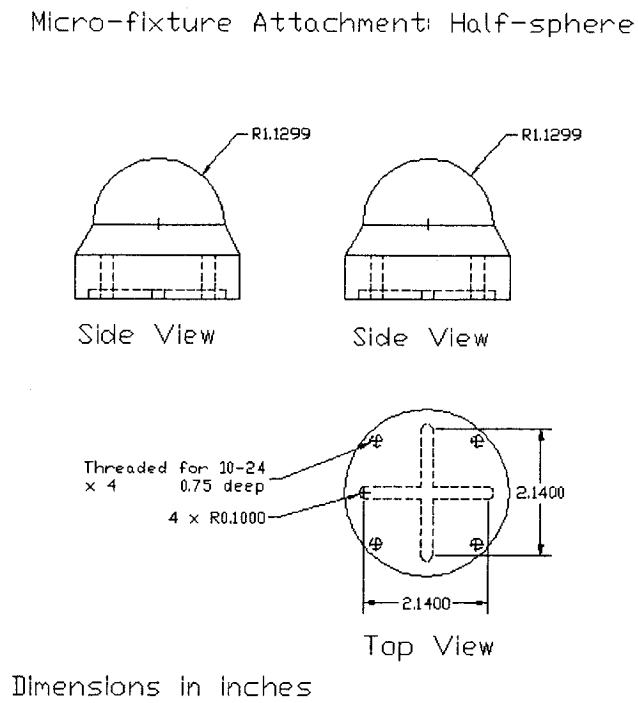

Figure A-4 Payload specifications: half-sphere

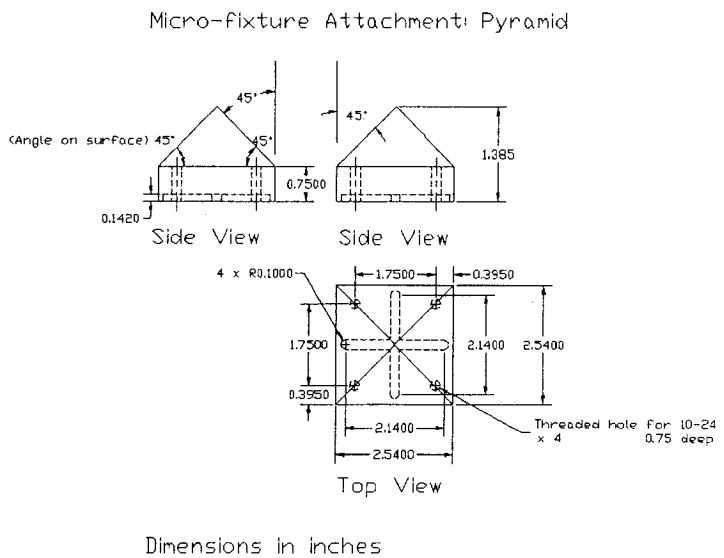

Figure A-5 Payload specifications: pyramid

Appendix B Toolbox Estimation Results

Included in this appendix are the stiffness and damping estimation results generated by the Single Point Contact Parameter Identification Toolbox for the STVF experiments described in Chapter 3. Some of the results were previously presented in Chapter 3. In each of the results tables, there is a column entitled 'Load Level.' As described in Chapter 3, the STVF single point contact experiments were conducted such that there was a stepwise increase in applied load. The 'Load Level' values listed refer to approximate contact load associated with the estimates listed in the columns to the right.

Legend

RLS – Recursive least squares algorithm

ILS – Instantaneous least squares algorithm

IA – Indirect adaptive algorithm

Kalman – Kalman filter algorithm

GLS – Global least squares algorithm

ETFE – Empirical transfer function estimator

OEM – Output error method

EEM – Equation error method

GMLM – Generalized maximum likelihood method

Table B-1 Plastic half-sphere stiffness estimates (N/m) - experiment #1

Load level (N)	RLS	ILS	IA	Kalman	GLS	ETFE	OEM	EEM	GMLM
50	1.38E+06	1.38E+06	1.38E+06	1.40E+06	1.40E+06	1.41E+06	1.40E+06	1.40E+06	1.39E+06
100	1.69E+06	1.69E+06	1.69E+06	1.63E+06	1.63E+06	1.64E+06	1.64E+06	1.64E+06	1.64E+06
150	1.72E+06	1.72E+06	1.72E+06	1.75E+06	1.75E+06	1.76E+06	1.77E+06	1.77E+06	1.77E+06
200	1.85E+06	1.85E+06	1.85E+06	1.87E+06	1.87E+06	1.86E+06	1.86E+06	1.86E+06	1.86E+06
250	1.95E+06	1.95E+06	1.95E+06	1.92E+06	1.92E+06	1.93E+06	1.93E+06	1.93E+06	1.93E+06
300	1.94E+06	1.94E+06	1.94E+06	1.96E+06	1.96E+06	1.97E+06	1.97E+06	1.97E+06	1.96E+06

Table B-2 Plastic half-sphere damping estimates (kg/s) - experiment #1

Load level (N)	RLS	ILS	IA	Kalman	GLS	ETFE	OEM	EEM	GMLM
50	75.94	0.00	-0.53	-5712.35	0.00	3752.88	3714.55	19067.00	4151.29
100	59.60	0.00	-0.57	-6561.00	0.00	-3200.43	-2255.95	-19159.10	-2391.62
150	0.00	0.00	-0.60	-6945.01	0.00	4721.97	3718.82	15495.00	3416.83
200	0.00	0.00	-0.56	-7569.92	0.00	-1844.01	-2372.87	-7059.20	-3341.07
250	0.00	0.00	-0.74	-7916.62	0.00	-1834.37	-1822.10	-7188.04	-2187.83
300	0.00	0.00	-0.32	-7533.79	0.00	1595.21	1585.17	3954.30	1703.80

Table B-3 Plastic half-sphere stiffness estimates (N/m) - experiment #2

Load level (N)	RLS	ILS	IA	Kalman	GLS	ETFE	OEM	EEM	GMLM
50	1.32E+06	1.32E+06	1.32E+06	1.34E+06	1.34E+06	1.35E+06	1.36E+06	1.36E+06	1.36E+06
100	1.58E+06	1.57E+06	1.57E+06	1.60E+06	1.60E+06	1.62E+06	1.62E+06	1.62E+06	1.62E+06
150	1.74E+06	1.74E+06	1.74E+06	1.76E+06	1.76E+06	1.74E+06	1.75E+06	1.75E+06	1.75E+06
200	1.83E+06	1.83E+06	1.83E+06	1.85E+06	1.85E+06	1.84E+06	1.86E+06	1.86E+06	1.85E+06
250	1.90E+06	1.90E+06	1.90E+06	1.92E+06	1.92E+06	1.93E+06	1.93E+06	1.93E+06	1.93E+06
300	1.97E+06	1.97E+06	1.97E+06	1.99E+06	1.99E+06	1.99E+06	1.99E+06	1.99E+06	1.99E+06

Table B-4 Plastic half-sphere damping estimates (kg/s) - experiment #2

Load level (N)	RLS	ILS	IA	Kalman	GLS	ETFE	OEM	EEM	GMLM
50	8.23	0.00	-1.08	-5682.56	0.00	6765.73	6827.86	25848.20	7589.12
100	0.00	0.00	-0.98	-6693.02	0.00	4937.65	4115.64	28672.80	3995.92
150	0.00	0.00	-0.68	-7531.75	0.00	603.61	580.41	7655.04	661.43
200	0.00	0.00	-1.07	-7618.73	0.00	-5688.91	-6741.70	-36561.20	-10878.20
250	0.00	0.00	-0.85	-7848.25	0.00	-955.56	-1024.27	-3967.82	-1065.98
300	0.00	0.00	-0.40	-8255.91	0.00	450.59	443.79	1437.94	668.47

Table B-5 Aluminum half-sphere stiffness estimates (N/m) - experiment #1

Load level (N)	RLS	ILS	IA	Kalman	GLS	ETFE	OEM	EEM	GMLM
50	2.00E+06	2.00E+06	2.00E+06	1.98E+06	1.99E+06	2.00E+06	1.99E+06	1.99E+06	1.99E+06
100	2.60E+06	2.60E+06	2.61E+06	2.46E+06	2.46E+06	2.46E+06	2.46E+06	2.46E+06	2.47E+06
150	2.57E+06	2.57E+06	2.57E+06	2.57E+06	2.57E+06	2.62E+06	2.61E+06	2.61E+06	2.61E+06
200	2.68E+06	2.68E+06	2.68E+06	2.72E+06	2.73E+06	2.70E+06	2.70E+06	2.70E+06	2.70E+06
250	2.77E+06	2.77E+06	2.77E+06	2.78E+06	2.79E+06	2.72E+06	2.71E+06	2.71E+06	2.71E+06
300	2.82E+06	2.82E+06	2.82E+06	2.77E+06	2.77E+06	2.78E+06	2.78E+06	2.78E+06	2.78E+06

Table B-6 Aluminum half-sphere damping estimates (kg/s) - experiment #1

Load level (N)	RLS	ILS	IA	Kalman	GLS	ETFE	OEM	EEM	GMLM
50	0.00	0.00	-0.49	-7380.01	0.00	-890.13	-956.14	-16365.90	-1424.29
100	0.00	0.00	-1.46	-8567.09	0.00	13123.60	16977.60	93469.50	18719.70
150	0.00	0.00	-0.93	-8769.15	0.00	-547.22	-556.35	-109435.00	-531.65
200	160.07	0.00	-1.17	-9856.00	0.00	1791.69	1857.19	5027.67	2245.88
250	22.85	0.00	-1.16	-10528.50	0.00	1302.09	1233.62	10620.70	584.54
300	13.78	0.00	-0.61	-11330.30	0.00	-0.65	-59.61	-71142.60	-97.27

Table B-7 Aluminum half-sphere stiffness estimates (N/m) - experiment #2

Load level (N)	RLS	ILS	IA	Kalman	GLS	ETFE	OEM	EEM	GMLM
50	2.63E+06	2.62E+06	2.63E+06	2.66E+06	2.71E+06	2.76E+06	2.78E+06	2.78E+06	2.78E+06
100	3.00E+06	3.00E+06	3.02E+06	2.85E+06	2.85E+06	2.81E+06	2.81E+06	2.81E+06	2.81E+06
150	3.00E+06	3.00E+06	2.99E+06	2.93E+06	2.94E+06	2.90E+06	2.91E+06	2.91E+06	2.90E+06
200	2.99E+06	2.99E+06	2.99E+06	3.03E+06	3.04E+06	2.99E+06	2.98E+06	2.98E+06	2.99E+06
250	3.02E+06	3.02E+06	3.02E+06	3.03E+06	3.03E+06	2.99E+06	2.98E+06	2.98E+06	2.98E+06
300	3.03E+06	3.03E+06	3.03E+06	3.05E+06	3.05E+06	3.00E+06	3.00E+06	3.00E+06	3.00E+06

Table B-8 Aluminum half-sphere damping estimates (kg/s) - experiment #2

Load level (N)	RLS	ILS	IA	Kalman	GLS	ETFE	OEM	EEM	GMLM
50	0.00	0.00	-1.12	-11720.10	0.00	17671.70	17372.90	44674.00	17328.80
100	0.00	0.00	-1.05	-11769.90	0.00	-6562.79	-1262.77	-593370.00	-449.04
150	0.00	0.00	-1.25	-10983.90	0.00	-2492.79	-2608.98	-9261.34	-2256.25
200	0.00	0.00	-0.92	-11117.00	0.00	-1195.61	-2213.67	-17844.60	-1975.46
250	46.72	0.00	-1.04	-10214.60	0.00	-4727.58	-4753.54	-6770.08	-4285.20
300	0.00	0.00	-1.08	-11055.50	0.00	-1243.75	-1481.53	-16597.20	-1599.14

Table B-9 Plastic cone stiffness estimates (N/m) - experiment #1

Load level (N)	RLS	ILS	IA	Kalman	GLS	ETFE	OEM	EEM	GMLM
50	7.91E+05	7.92E+05	7.91E+05	7.93E+05	7.95E+05	7.96E+05	7.94E+05	7.94E+05	7.95E+05
100	9.61E+05	9.61E+05	9.61E+05	9.63E+05	9.64E+05	9.58E+05	9.59E+05	9.59E+05	9.58E+05
150	1.07E+06	1.07E+06	1.07E+06	1.08E+06	1.08E+06	1.08E+06	1.08E+06	1.08E+06	1.08E+06
200	1.12E+06	1.12E+06	1.12E+06	1.12E+06	1.12E+06	1.13E+06	1.13E+06	1.13E+06	1.13E+06
250	1.15E+06	1.15E+06	1.15E+06	1.16E+06	1.16E+06	1.16E+06	1.16E+06	1.16E+06	1.16E+06
300	1.14E+06	1.14E+06	1.14E+06	1.17E+06	1.18E+06	1.16E+06	1.16E+06	1.16E+06	1.16E+06
350	1.14E+06	1.14E+06	1.14E+06	1.17E+06	1.17E+06	1.17E+06	1.16E+06	1.16E+06	1.16E+06

Table B-10 Plastic cone damping estimates (kg/s) - experiment #1

Load level (N)	RLS	ILS	IA	Kalman	GLS	ETFE	OEM	EEM	GMLM
50	46.49	0.00	-0.73	-3762.90	0.00	209.80	201.25	527.88	229.80
100	47.27	0.00	-0.53	-4457.57	0.00	-99.69	132.16	19163.20	130.97
150	0.00	0.00	-0.93	-6263.75	0.00	950.30	877.13	1566.19	717.99
200	0.00	0.00	-1.28	-6486.64	0.00	63.13	62.86	85.43	56.70
250	0.00	0.00	-0.33	-4092.84	0.00	1959.46	1924.95	3351.60	1929.63
300	18.36	0.00	-0.29	-4586.22	0.00	1150.86	560.88	30095.10	162.77
350	35.95	0.00	-0.30	-4868.87	0.00	1114.67	1101.75	1792.18	1107.58

Table B-11 Plastic cone stiffness estimates (N/m) - experiment #2

Load level (N)	RLS	ILS	IA	Kalman	GLS	ETFE	OEM	EEM	GMLM
50	8.29E+05	8.29E+05	8.29E+05	8.23E+05	8.25E+05	8.36E+05	8.25E+05	8.25E+05	8.28E+05
100	1.01E+06	1.01E+06	1.01E+06	1.02E+06	1.02E+06	1.00E+06	1.00E+06	1.00E+06	1.00E+06
150	1.11E+06	1.11E+06	1.11E+06	1.11E+06	1.11E+06	1.11E+06	1.11E+06	1.11E+06	1.11E+06
200	1.20E+06	1.20E+06	1.20E+06	1.20E+06	1.20E+06	1.20E+06	1.20E+06	1.20E+06	1.20E+06
250	1.25E+06	1.25E+06	1.25E+06	1.24E+06	1.24E+06	1.25E+06	1.25E+06	1.25E+06	1.25E+06
300	1.30E+06	1.30E+06	1.30E+06	1.29E+06	1.29E+06	1.29E+06	1.29E+06	1.29E+06	1.29E+06
350	1.31E+06	1.31E+06	1.31E+06	1.32E+06	1.33E+06	1.33E+06	1.32E+06	1.32E+06	1.32E+06

Table B-12 Plastic cone damping estimates (kg/s) - experiment #2

Load level (N)	RLS	ILS	IA	Kalman	GLS	ETFE	OEM	EEM	GMLM
50	4.56	0.00	-0.45	-3160.40	0.00	231.56	236.47	2210.36	359.07
100	0.00	0.00	-0.61	-4209.68	0.00	-180.31	-180.52	-212.33	-172.61
150	0.00	0.00	-0.44	-4739.06	0.00	142.94	40.91	29471.80	-41.43
200	5.65	0.00	-0.46	-4867.03	0.00	417.58	466.86	3409.19	490.90
250	15.62	0.00	-0.40	-5020.75	0.00	154.12	153.95	780.99	178.42
300	0.00	0.00	-0.63	-5088.17	0.00	-242.09	-239.63	-8960.24	-351.76
350	0.00	0.00	-0.31	-5418.49	0.00	-124.23	-123.55	-391.96	-97.53

Table B-13 Plastic cone stiffness estimates (N/m) - experiment #1

Load level (N)	RLS	ILS	IA	Kalman	GLS	ETFE	OEM	EEM	GMLM
50	5.69E+05	5.69E+05	5.69E+05	5.76E+05	5.76E+05	5.78E+05	5.78E+05	5.78E+05	5.78E+05
100	6.63E+05	6.63E+05	6.63E+05	6.69E+05	6.69E+05	6.72E+05	6.73E+05	6.73E+05	6.73E+05
150	7.19E+05	7.19E+05	7.19E+05	7.24E+05	7.24E+05	7.30E+05	7.29E+05	7.29E+05	7.29E+05
200	7.58E+05	7.58E+05	7.58E+05	7.59E+05	7.59E+05	7.63E+05	7.66E+05	7.66E+05	7.65E+05
250	7.77E+05	7.77E+05	7.77E+05	7.90E+05	7.90E+05	7.90E+05	7.91E+05	7.91E+05	7.91E+05
300	7.86E+05	7.86E+05	7.87E+05	8.00E+05	8.00E+05	8.03E+05	8.01E+05	8.01E+05	8.02E+05

Table B-14 Plastic cone damping estimates (kg/s) - experiment #1

Load level (N)	RLS	ILS	IA	Kalman	GLS	ETFE	OEM	EEM	GMLM
50	43.79	0.00	-0.51	-2398.31	0.00	2085.12	2062.03	3497.09	2216.07
100	22.46	0.00	-0.45	-2768.41	0.00	-25.44	-26.53	-550.30	1.24
150	0.00	0.00	-0.45	-3019.03	0.00	28.57	27.80	121.54	27.10
200	0.00	0.00	-0.47	-2983.78	0.00	689.39	309.44	90355.70	360.28
250	35.01	0.00	-0.41	-3375.17	0.00	4028.75	3160.47	20931.80	3180.30
300	86.43	0.00	-0.41	-2777.40	0.00	-1880.14	-2139.33	-10704.20	-2314.82

Table B-15 Plastic cone stiffness estimates (N/m) - experiment #2

Load level (N)	RLS	ILS	IA	Kalman	GLS	ETFE	OEM	EEM	GMLM
50	6.50E+05	6.50E+05	6.50E+05	6.53E+05	6.54E+05	6.60E+05	6.60E+05	6.60E+05	6.60E+05
100	7.49E+05	7.49E+05	7.50E+05	7.42E+05	7.43E+05	7.44E+05	7.45E+05	7.45E+05	7.45E+05
150	8.17E+05	8.17E+05	8.16E+05	8.21E+05	8.21E+05	8.22E+05	8.21E+05	8.21E+05	8.22E+05
200	8.63E+05	8.63E+05	8.63E+05	8.67E+05	8.67E+05	8.71E+05	8.70E+05	8.70E+05	8.70E+05
250	9.30E+05	9.30E+05	9.30E+05	9.29E+05	9.29E+05	9.33E+05	9.32E+05	9.32E+05	9.32E+05
300	9.67E+05	9.67E+05	9.66E+05	9.76E+05	9.76E+05	9.79E+05	9.78E+05	9.78E+05	9.78E+05
350	1.00E+06	1.00E+06	1.00E+06	1.00E+06	1.00E+06	1.01E+06	1.00E+06	1.00E+06	1.00E+06

Table B-16 Plastic cone damping estimates (kg/s) - experiment #2

Load level (N)	RLS	ILS	IA	Kalman	GLS	ETFE	OEM	EEM	GMLM
50	31.61	0.00	-0.62	-2998.86	0.00	374.95	393.33	1381.47	476.53
100	101.54	0.00	-0.75	-3576.23	0.00	-143.26	-133.55	-5167.02	-145.59
150	0.00	0.00	-1.96	-5136.80	0.00	425.28	261.34	9762.97	35.64
200	0.00	0.00	-1.96	-6810.82	0.00	-5.43	-5.39	-872.01	7.94
250	7.56	0.00	-0.36	-3775.00	0.00	370.45	393.39	2039.58	443.97
300	62.95	0.00	-0.23	-3222.39	0.00	1377.73	1358.55	1951.59	1358.75
350	62.95	0.00	-0.23	-3222.39	0.00	1377.73	1358.55	1951.59	1358.75

Table B-17 Plastic triangular prism stiffness estimates (N/m) - experiment #1

Load level (N)	RLS	ILS	IA	Kalman	GLS	ETFE	OEM	EEM	GMLM
50	1.03E+06	1.03E+06	1.03E+06	1.00E+06	1.01E+06	1.01E+06	1.02E+06	1.02E+06	1.02E+06
100	1.25E+06	1.25E+06	1.25E+06	1.23E+06	1.24E+06	1.24E+06	1.23E+06	1.23E+06	1.23E+06
150	1.15E+06	1.15E+06	1.15E+06	1.24E+06	1.25E+06	1.25E+06	1.24E+06	1.24E+06	1.24E+06
200	9.67E+05	9.67E+05	9.68E+05	1.06E+06	1.06E+06	1.06E+06	1.06E+06	1.06E+06	1.07E+06
250	1.03E+06	1.03E+06	1.03E+06	1.05E+06	1.05E+06	1.04E+06	1.05E+06	1.05E+06	1.05E+06
300	1.08E+06	1.08E+06	1.08E+06	1.11E+06	1.11E+06	1.10E+06	1.10E+06	1.10E+06	1.10E+06
350	1.14E+06	1.14E+06	1.14E+06	1.15E+06	1.15E+06	1.15E+06	1.16E+06	1.16E+06	1.16E+06

Table B-18 Plastic triangular prism damping estimates (kg/s) - experiment #1

Load level (N)	RLS	ILS	IA	Kalman	GLS	ETFE	OEM	EEM	GMLM
50	0.00	0.00	-0.66	-4308.33	0.00	-2275.00	-2266.73	-3322.27	-2359.73
100	68.24	0.00	-0.75	-5219.14	0.00	-736.41	-741.08	-7869.58	-398.45
150	0.00	0.00	-0.51	-4376.11	0.00	4577.47	4759.16	11674.20	4725.43
200	116.78	0.00	-0.33	-898.73	0.00	22206.50	22217.40	45459.40	22475.60
250	0.00	0.00	-0.39	-4013.89	0.00	737.17	730.47	5474.36	530.81
300	93.47	0.00	-0.32	-3540.14	0.00	7000.38	7281.09	15737.60	8075.75
350	0.00	0.00	-0.26	-3916.05	0.00	1968.54	2228.39	8080.37	3442.57

Table B-19 Plastic triangular prism stiffness estimates (N/m) - experiment #2

Load level (N)	RLS	ILS	IA	Kalman	GLS	ETFE	OEM	EEM	GMLM
50	9.84E+05	9.84E+05	9.83E+05	9.92E+05	9.97E+05	1.00E+06	9.99E+05	9.99E+05	1.00E+06
100	1.16E+06	1.16E+06	1.16E+06	1.19E+06	1.19E+06	1.19E+06	1.19E+06	1.19E+06	1.19E+06
150	9.69E+05	9.69E+05	9.69E+05	1.09E+06	1.09E+06	1.09E+06	1.09E+06	1.09E+06	1.09E+06
200	8.78E+05	8.78E+05	8.77E+05	9.62E+05	9.62E+05	9.72E+05	9.71E+05	9.71E+05	9.72E+05
250	8.62E+05	8.62E+05	8.62E+05	8.89E+05	8.89E+05	9.07E+05	9.08E+05	9.08E+05	9.07E+05
300	9.39E+05	9.39E+05	9.38E+05	9.45E+05	9.45E+05	9.49E+05	9.48E+05	9.48E+05	9.48E+05
350	1.01E+06	1.01E+06	1.01E+06	1.01E+06	1.01E+06	1.01E+06	1.01E+06	1.01E+06	1.01E+06

Table B-20 Plastic triangular prism damping estimates (kg/s) - experiment #2

Load level (N)	RLS	ILS	IA	Kalman	GLS	ETFE	OEM	EEM	GMLM
50	0.00	0.00	-0.55	-4269.78	0.00	-321.42	-321.05	-7212.49	-426.37
100	0.00	0.00	-0.56	-4699.58	0.00	2373.88	2415.87	3244.24	2399.62
150	0.00	0.00	-0.61	-3627.88	0.00	56268.30	57504.80	58599.10	59460.60
200	0.00	0.00	-0.08	-2078.87	0.00	1137.21	1167.53	1735.77	1164.56
250	0.00	0.00	-0.14	2233.02	2136.71	628.40	639.54	799.35	674.22
300	0.00	0.00	-0.29	-3111.00	0.00	-1184.91	-1263.02	-2586.57	-1315.21
350	0.00	0.00	-0.06	-3095.33	0.00	904.72	917.50	1678.11	953.67

Table B-21 Plastic cube stiffness estimates (N/m) - experiment #1

Load level (N)	RLS	ILS	IA	Kalman	GLS	ETFE	OEM	EEM	GMLM
50	8.05E+05	8.05E+05	8.05E+05	9.10E+05	9.13E+05	9.79E+05	9.43E+05	9.43E+05	9.58E+05
100	8.29E+05	8.29E+05	8.29E+05	9.16E+05	9.17E+05	9.46E+05	9.41E+05	9.41E+05	9.44E+05
150	7.75E+05	7.75E+05	7.76E+05	8.35E+05	8.35E+05	8.61E+05	8.61E+05	8.61E+05	8.60E+05
200	6.74E+05	6.74E+05	6.74E+05	7.54E+05	7.54E+05	7.66E+05	7.65E+05	7.65E+05	7.64E+05
250	5.90E+05	5.90E+05	5.89E+05	6.22E+05	6.22E+05	6.35E+05	6.31E+05	6.31E+05	6.31E+05
300	6.68E+05	6.68E+05	6.69E+05	6.67E+05	6.67E+05	6.61E+05	6.64E+05	6.64E+05	6.63E+05
350	7.41E+05	7.41E+05	7.40E+05	7.40E+05	7.41E+05	7.43E+05	7.43E+05	7.43E+05	7.43E+05

Table B-22 Plastic cube damping estimates (kg/s) - experiment #1

Load level (N)	RLS	ILS	IA	Kalman	GLS	ETFE	OEM	EEM	GMLM
50	0.00	0.00	-0.55	-1320.37	0.00	137048.00	130950.00	324761.00	172700.00
100	0.00	0.00	-0.53	-1779.93	0.00	3450.61	3545.89	5443.63	3652.37
150	127.36	0.00	-0.41	1338.54	1307.08	1369.18	1391.18	2113.05	1442.17
200	0.00	0.00	-0.38	2208.47	2159.13	441.55	444.92	616.69	457.54
250	0.00	0.00	-0.11	7444.32	7469.42	6491.27	6395.25	11594.30	6440.01
300	0.00	0.00	-0.07	-1075.24	0.00	597.16	501.30	56948.80	98.84
350	0.00	0.00	-0.18	-1535.27	0.00	93.70	99.78	412.45	99.43

Table B-23 Plastic cube stiffness estimates (N/m) - experiment #2

Load level (N)	RLS	ILS	IA	Kalman	GLS	ETFE	OEM	EEM	GMLM
50	5.32E+05	5.32E+05	5.32E+05	5.90E+05	5.91E+05	6.06E+05	6.01E+05	6.01E+05	5.99E+05
100	5.84E+05	5.85E+05	5.85E+05	6.38E+05	6.38E+05	6.50E+05	6.48E+05	6.48E+05	6.45E+05
150	5.48E+05	5.48E+05	5.47E+05	6.05E+05	6.05E+05	6.18E+05	6.18E+05	6.18E+05	6.17E+05
200	4.80E+05	4.80E+05	4.80E+05	5.36E+05	5.36E+05	5.49E+05	5.49E+05	5.49E+05	5.49E+05
250	3.83E+05	3.83E+05	3.82E+05	4.29E+05	4.29E+05	4.35E+05	4.37E+05	4.37E+05	NaN
300	4.21E+05	4.21E+05	4.21E+05	4.22E+05	4.22E+05	4.22E+05	4.22E+05	4.22E+05	NaN

Table B-24 Plastic cube damping estimates (kg/s) - experiment #2

Load level (N)	RLS	ILS	IA	Kalman	GLS	ETFE	OEM	EEM	GMLM
50	0.00	0.00	-0.65	-3026.00	0.00	20084.50	23991.10	89469.70	27028.00
100	0.00	0.00	-0.40	-1822.09	0.00	10304.00	10156.90	18426.50	11849.80
150	0.00	0.00	-0.67	1216.50	1230.14	39467.30	41493.80	44458.10	43405.20
200	0.00	0.00	-0.58	1480.17	1432.40	231.25	231.21	286.00	241.83
250	0.00	0.00	-0.01	4145.55	4166.14	8408.96	6605.25	37464.80	NaN
300	0.00	0.00	0.19	-1432.32	0.00	476.97	515.17	1658.96	NaN

Appendix C Linear Stiffness Estimates

Included in this appendix are data tables providing the linear stiffness estimates of the simple geometry payloads determined using the relationships from the Instron experiment analysis. Refer to Section 3.4.3 for discussion.

Table C-1 Summary – STVF payload experiment set #2 - Payload linear secant stiffness (N/m)

Load Level (N)	Aluminum half-sphere	Plastic half-sphere	Plastic cone	Plastic pyramid	Plastic prism	Plastic cube
50	7.94E+06	3.17E+06	1.76E+06	1.16E+06	3.87E+06	5.86E+06
100	9.14E+06	3.67E+06	2.06E+06	1.33E+06	4.71E+06	6.93E+06
150	9.94E+06	4.00E+06	2.27E+06	1.44E+06	5.29E+06	7.66E+06
200	1.06E+07	4.26E+06	2.43E+06	1.52E+06	5.75E+06	8.23E+06
250	1.11E+07	4.47E+06	2.56E+06	1.60E+06	6.14E+06	8.71E+06
300	1.15E+07	4.65E+06	2.68E+06	1.66E+06	6.48E+06	9.12E+06

Table C-2 Aluminum half-sphere secant stiffness approximations

Aluminum half-sphere experiment #1			Aluminum half-sphere experiment #2		
Average Load† (N)	Displacement‡ (m)	Secant stiffness (N/m)	Average Load† (N)	Displacement‡ (m)	Secant stiffness (N/m)
52.00	6.50E-06	7.99E+06	50.50	6.36E-06	7.94E+06
100.80	1.10E-05	9.20E+06	97.83	1.07E-05	9.14E+06
149.80	1.50E-05	1.00E+07	145.18	1.46E-05	9.94E+06
198.79	1.87E-05	1.06E+07	192.96	1.83E-05	1.06E+07
247.89	2.22E-05	1.11E+07	241.38	2.18E-05	1.11E+07
297.00	2.57E-05	1.16E+07	290.09	2.52E-05	1.15E+07

† average load at step intervals for first STVF aluminum half-sphere contact experiments

‡ displacement calculated from average load and $F = 2.01e8\delta^{1.27}$ equation

Table C-3 Plastic half-sphere secant stiffness approximations

Plastic half-sphere experiment #1			Plastic half-sphere experiment #2		
Average Load† (N)	Displacement‡ (m)	Secant stiffness (N/m)	Average Load† (N)	Displacement‡ (m)	Secant stiffness (N/m)
50.40	1.59E-05	3.17E+06	50.57	1.59E-05	3.17E+06
97.82	2.67E-05	3.67E+06	98.05	2.67E-05	3.67E+06
144.77	3.62E-05	4.00E+06	145.61	3.64E-05	4.00E+06
192.71	4.53E-05	4.25E+06	193.14	4.54E-05	4.26E+06
240.48	5.39E-05	4.47E+06	241.28	5.40E-05	4.47E+06
287.45	6.19E-05	4.64E+06	289.94	6.23E-05	4.65E+06

† average load at step intervals for first STVF plastic half-sphere contact experiments

‡ displacement calculated from average load and $F = 7.00e7\delta^{1.28}$ equation

Table C-4 Plastic cone secant stiffness approximations

Plastic cone experiment #1			Plastic cone experiment #2		
Average Load† (N)	Displacement‡ (m)	Secant stiffness (N/m)	Average Load† (N)	Displacement‡ (m)	Secant stiffness (N/m)
50.84	2.89E-05	1.76E+06	50.92	2.90E-05	1.76E+06
98.59	4.78E-05	2.06E+06	98.68	4.78E-05	2.06E+06
146.43	6.45E-05	2.27E+06	146.60	6.45E-05	2.27E+06
194.49	7.99E-05	2.43E+06	194.08	7.98E-05	2.43E+06
242.44	9.45E-05	2.57E+06	241.64	9.42E-05	2.56E+06
290.47	1.08E-04	2.68E+06	290.19	1.08E-04	2.68E+06
N/A	N/A	N/A	337.65	1.21E-04	2.78E+06

† average load at step intervals for respective STVF plastic cone contact experiments

‡ displacement calculated from average load and $F = 4.98e7\delta^{1.32}$ equation

Table C-5 Plastic pyramid secant stiffness approximations

Plastic pyramid experiment #1			Plastic pyramid experiment #2		
Average Load† (N)	Displacement‡ (m)	Secant stiffness (N/m)	Average Load† (N)	Displacement‡ (m)	Secant stiffness (N/m)
51.02	4.41E-05	1.16E+06	50.78	4.39E-05	1.16E+06
98.78	7.45E-05	1.33E+06	98.40	7.43E-05	1.33E+06
146.48	1.02E-04	1.44E+06	146.34	1.02E-04	1.44E+06
194.16	1.27E-04	1.52E+06	193.79	1.27E-04	1.52E+06
242.79	1.52E-04	1.60E+06	242.27	1.52E-04	1.60E+06
290.90	1.76E-04	1.66E+06	290.08	1.75E-04	1.66E+06

† average load at step intervals for first STVF plastic pyramid contact experiments

‡ displacement calculated from average load and $F = 1.57e7\delta^{1.26}$ equation

Table C-6 Plastic prism secant stiffness approximations

Plastic prism experiment #1			Plastic prism experiment #2		
Average Load† (N)	Displacement‡ (m)	Secant stiffness (N/m)	Average Load† (N)	Displacement‡ (m)	Secant stiffness (N/m)
50.83	1.31E-05	3.87E+06	50.93	1.32E-05	3.87E+06
98.61	2.10E-05	4.70E+06	98.68	2.10E-05	4.71E+06
146.35	2.77E-05	5.29E+06	146.67	2.77E-05	5.29E+06
194.19	3.38E-05	5.75E+06	194.60	3.38E-05	5.75E+06
241.95	3.94E-05	6.13E+06	242.58	3.95E-05	6.14E+06
290.23	4.48E-05	6.47E+06	290.58	4.49E-05	6.48E+06
337.55	4.99E-05	6.77E+06	338.24	4.99E-05	6.77E+06

† average load at step intervals for first STVF plastic triangular prism contact experiments

‡ displacement calculated from average load and $F = 4.34e8\delta^{1.42}$ equation

Table C-7 Plastic cube secant stiffness approximations

Plastic cube experiment #1			Plastic cube experiment #2		
Average Load† (N)	Displacement‡ (m)	Secant stiffness (N/m)	Average Load† (N)	Displacement‡ (m)	Secant stiffness (N/m)
50.07	8.58E-06	5.83E+06	51.00	8.70E-06	5.86E+06
97.28	1.41E-05	6.90E+06	98.71	1.42E-05	6.93E+06
145.24	1.90E-05	7.64E+06	146.69	1.91E-05	7.66E+06
192.99	2.35E-05	8.22E+06	194.76	2.37E-05	8.23E+06
241.87	2.78E-05	8.70E+06	242.77	2.79E-05	8.71E+06
288.40	3.17E-05	9.10E+06	290.86	3.19E-05	9.12E+06
336.72	3.56E-05	9.46E+06	N/A	N/A	N/A

† average load at step intervals for first STVF plastic cube contact experiments

‡ displacement calculated from average load and $F = 3.08e8\delta^{1.34}$ equation

Appendix D Payload Stiffness

Included in this appendix are data tables that compare the calculated payload stiffness (k_{calc}) from STVF test-bed experimental data with the independently determined linear payload stiffness estimates ($k_{payload}$). Refer to Section 3.5 for discussion.

Table D-1 Payload stiffness estimation from STVF aluminum half-sphere experiment #1

Load Level (N)	$k_{SMT+payload}$ (N/m)	k_{SMT} (N/m)	Calculated payload stiffness, k_{calc} (N/m)	$k_{payload}$ (N/m)	Error (%)
52.00	1.99E+06	3.46E+06	4.69E+06	7.99E+06	41.30
100.80	2.53E+06	3.46E+06	9.39E+06	9.20E+06	2.06
149.80	2.57E+06	3.46E+06	9.97E+06	1.00E+07	0.44
198.79	2.70E+06	3.46E+06	1.22E+07	1.06E+07	14.85
247.89	2.78E+06	3.46E+06	1.40E+07	1.11E+07	25.98
297.00	2.80E+06	3.46E+06	1.46E+07	1.16E+07	26.41

Table D-2 Payload stiffness estimation from STVF aluminum half-sphere experiment #2

Load Level (N)	$k_{SMT+payload}$ (N/m)	k_{SMT} (N/m)	Calculated payload stiffness, k_{calc} (N/m)	$k_{payload}$ (N/m)	Error (%)
50.50	2.66E+06	3.46E+06	1.14E+07	7.94E+06	43.63
97.83	2.93E+06	3.46E+06	1.90E+07	9.14E+06	107.38
145.18	2.97E+06	3.46E+06	2.08E+07	9.94E+06	109.03
192.96	3.01E+06	3.46E+06	2.31E+07	1.06E+07	118.29
241.38	3.02E+06	3.46E+06	2.38E+07	1.11E+07	114.41
290.09	3.04E+06	3.46E+06	2.46E+07	1.15E+07	113.77

Table D-3 Payload stiffness estimation from STVF plastic half-sphere experiment #1

Load Level (N)	$k_{SMT+payload}$ (N/m)	k_{SMT} (N/m)	Calculated payload stiffness, k_{calc} (N/m)	$k_{payload}$ (N/m)	Error (%)
50.40	1.39E+06	3.46E+06	2.33E+06	3.17E+06	26.47
97.82	1.66E+06	3.46E+06	3.17E+06	3.67E+06	13.54
144.77	1.75E+06	3.46E+06	3.52E+06	4.00E+06	11.94
192.71	1.86E+06	3.46E+06	4.01E+06	4.25E+06	5.68
240.48	1.94E+06	3.46E+06	4.39E+06	4.47E+06	1.61
287.45	1.96E+06	3.46E+06	4.50E+06	4.64E+06	2.98

Table D-4 Payload stiffness estimation from STVF plastic half-sphere experiment #2

Load Level (N)	$k_{SMT+payload}$ (N/m)	k_{SMT} (N/m)	Calculated payload stiffness, k_{calc} (N/m)	$k_{payload}$ (N/m)	Error (%)
50.57	1.25E+06	3.46E+06	1.96E+06	3.17E+06	38.18
98.05	1.54E+06	3.46E+06	2.77E+06	3.67E+06	24.49
145.61	1.70E+06	3.46E+06	3.34E+06	4.00E+06	16.43
193.14	1.81E+06	3.46E+06	3.78E+06	4.26E+06	11.23
241.28	1.88E+06	3.46E+06	4.11E+06	4.47E+06	8.09
289.94	1.94E+06	3.46E+06	4.44E+06	4.65E+06	4.65

Table D-5 Payload stiffness estimation from STVF plastic cone experiment #1

Load Level (N)	$k_{SMT+payload}$ (N/m)	k_{SMT} (N/m)	Calculated payload stiffness, k_{calc} (N/m)	$k_{payload}$ (N/m)	Error (%)
50.84	7.93E+05	3.46E+06	1.03E+06	1.76E+06	41.43
98.59	9.61E+05	3.46E+06	1.33E+06	2.06E+06	35.58
146.43	1.08E+06	3.46E+06	1.56E+06	2.27E+06	31.25
194.49	1.12E+06	3.46E+06	1.67E+06	2.43E+06	31.54
242.44	1.16E+06	3.46E+06	1.74E+06	2.57E+06	32.36
290.47	1.16E+06	3.46E+06	1.74E+06	2.68E+06	35.04

Table D-6 Payload stiffness estimation from STVF plastic cone experiment #2

Load Level (N)	$k_{SMT+payload}$ (N/m)	k_{SMT} (N/m)	Calculated payload stiffness, k_{calc} (N/m)	$k_{payload}$ (N/m)	Error (%)
50.92	8.28E+05	3.46E+06	1.09E+06	1.76E+06	38.13
98.68	1.01E+06	3.46E+06	1.42E+06	2.06E+06	31.28
146.60	1.11E+06	3.46E+06	1.64E+06	2.27E+06	27.89
194.08	1.20E+06	3.46E+06	1.84E+06	2.43E+06	24.42
241.64	1.25E+06	3.46E+06	1.95E+06	2.56E+06	23.86
290.19	1.29E+06	3.46E+06	2.07E+06	2.68E+06	22.96
337.65	1.32E+06	3.46E+06	2.13E+06	2.78E+06	23.48

Table D-7 Payload stiffness estimation from STVF plastic pyramid experiment #1

Load Level (N)	$k_{SMT+payload}$ (N/m)	k_{SMT} (N/m)	Calculated payload stiffness, k_{calc} (N/m)	$k_{payload}$ (N/m)	Error (%)
51.02	5.75E+05	3.46E+06	6.89E+05	1.16E+06	40.46
98.78	6.68E+05	3.46E+06	8.28E+05	1.33E+06	37.54
146.48	7.25E+05	3.46E+06	9.17E+05	1.44E+06	36.29
194.16	7.61E+05	3.46E+06	9.76E+05	1.52E+06	35.98
242.79	7.86E+05	3.46E+06	1.02E+06	1.60E+06	36.31
290.90	7.96E+05	3.46E+06	1.03E+06	1.66E+06	37.61

Table D-8 Payload stiffness estimation from STVF plastic pyramid experiment #2

Load Level (N)	$k_{SMT+payload}$ (N/m)	k_{SMT} (N/m)	Calculated payload stiffness, k_{calc} (N/m)	$k_{payload}$ (N/m)	Error (%)
50.78	6.55E+05	3.46E+06	8.08E+05	1.16E+06	30.10
98.40	7.46E+05	3.46E+06	9.50E+05	1.33E+06	28.28
146.34	8.20E+05	3.46E+06	1.07E+06	1.44E+06	25.32
193.79	8.67E+05	3.46E+06	1.16E+06	1.52E+06	24.11
242.27	9.31E+05	3.46E+06	1.27E+06	1.60E+06	20.23
290.08	9.74E+05	3.46E+06	1.35E+06	1.66E+06	18.21

Table D-9 Payload stiffness estimation from STVF plastic prism experiment #1

Load Level (N)	$k_{SMT+payload}$ (N/m)	k_{SMT} (N/m)	Calculated payload stiffness, k_{calc} (N/m)	$k_{payload}$ (N/m)	Error (%)
50.83	1.02E+06	3.46E+06	1.44E+06	3.87E+06	62.71
98.61	1.24E+06	3.46E+06	1.93E+06	4.70E+06	58.92
146.35	1.21E+06	3.46E+06	1.87E+06	5.29E+06	64.66
194.19	1.03E+06	3.46E+06	1.47E+06	5.75E+06	74.48
241.95	1.04E+06	3.46E+06	1.49E+06	6.13E+06	75.72
290.23	1.10E+06	3.46E+06	1.60E+06	6.47E+06	75.22
337.55	1.15E+06	3.46E+06	1.72E+06	6.77E+06	74.57

Table D-10 Payload stiffness estimation from STVF plastic prism experiment #2

Load Level (N)	$k_{SMT+payload}$ (N/m)	k_{SMT} (N/m)	Calculated payload stiffness, k_{calc} (N/m)	$k_{payload}$ (N/m)	Error (%)
50.93	9.93E+05	3.46E+06	1.39E+06	3.87E+06	63.99
98.68	1.18E+06	3.46E+06	1.79E+06	4.71E+06	61.95
146.67	1.05E+06	3.46E+06	1.51E+06	5.29E+06	71.53
194.60	9.38E+05	3.46E+06	1.29E+06	5.75E+06	77.63
242.58	8.88E+05	3.46E+06	1.19E+06	6.14E+06	80.54
290.58	9.44E+05	3.46E+06	1.30E+06	6.48E+06	79.96
338.24	1.01E+06	3.46E+06	1.42E+06	6.77E+06	78.97

Table D-11 Payload stiffness estimation from STVF plastic cube experiment #1

Load Level (N)	$k_{SMT+payload}$ (N/m)	k_{SMT} (N/m)	Calculated payload stiffness, k_{calc} (N/m)	$k_{payload}$ (N/m)	Error (%)
50.07	8.95E+05	3.46E+06	1.21E+06	5.83E+06	79.30
97.28	8.99E+05	3.46E+06	1.21E+06	6.90E+06	82.41
145.24	8.26E+05	3.46E+06	1.09E+06	7.64E+06	85.80
192.99	7.32E+05	3.46E+06	9.29E+05	8.22E+06	88.69
241.87	6.16E+05	3.46E+06	7.49E+05	8.70E+06	91.39
288.40	6.65E+05	3.46E+06	8.24E+05	9.10E+06	90.94
336.72	7.42E+05	3.46E+06	9.44E+05	9.46E+06	90.02

Table D-12 Payload stiffness estimation from STVF plastic cube experiment #2

Load Level (N)	$k_{SMT+payload}$ (N/m)	k_{SMT} (N/m)	Calculated payload stiffness, k_{calc} (N/m)	$k_{payload}$ (N/m)	Error (%)
51.00	5.76E+05	3.46E+06	6.91E+05	5.86E+06	88.21
98.71	6.25E+05	3.46E+06	7.62E+05	6.93E+06	89.01
146.69	5.92E+05	3.46E+06	7.14E+05	7.66E+06	90.69
194.76	5.23E+05	3.46E+06	6.16E+05	8.23E+06	92.52
242.77	4.14E+05	3.46E+06	4.71E+05	8.71E+06	94.60
290.86	4.22E+05	3.46E+06	4.80E+05	9.12E+06	94.73

Appendix E Geometry Mismatch Results

This appendix contains model geometry sensitivity results for the ACU gravity drop simulation. The results listed here are for the cases of modifying the position, size and orientation of three of the v-guides on the ACU body. The numbering of the v-guides was described in Section 5.2.2. Other results and discussion of the results is found in Section 5.2.3.

Table E-1 ACU simulation contact parameter estimates - v-guide 2 modifications

	Stiffness		Damping		Coeff. of Friction	
Modification	**Value (N/m)**	**Error (%)**	**Value (kg/s)**	**Error (%)**	**Value**	**Error (%)**
Expected parameter values	100000.0	--	38.37	--	0.1000	--
No geometry modifications	99992.7	0.01	37.54	2.16	0.1028	2.80
v-guide 2: 1e-3 m back shift	100008.0	0.01	37.4	2.41	0.1028	2.79
v-guide 2: 2e-3 m back shift	100031	99.96	37.49	2.28	0.1028	2.78
v-guide 2: 5e-3 m back shift	100095.0	0.10	37.62	1.95	0.1027	2.69
v-guide 2: 1e-6 m forward shift	99992.6	0.01	37.54	2.16	0.1028	2.80
v-guide 2: 1e-5 m forward shift	99992.8	0.01	37.54	2.16	0.1028	2.81
v-guide 2: 1e-4 m forward shift	100000.0	0.00	37.54	2.16	0.1029	2.91
v-guide 2: 3e-4 m forward shift	99987.2	0.01	37.48	2.30	0.1294	29.40
v-guide 2: 6e-4 m forward shift	99074.8	0.93	33.53	12.60	0.1445	44.47
v-guide 2: 1e-3 m forward shift	93554.8	6.45	27.42	28.52	0.1117	11.74
v-guide 2: 2e-3 m forward shift	63729.1	36.27	33.35	13.07	0.0571	42.91
v-guide 2: 3e-3 m forward shift	44351.4	55.65	33.45	12.82	0.0374	62.63
v-guide 2: 1e-6 m side shift	99986.9	0.01	37.50	2.25	0.1028	2.81
v-guide 2: 1e-5 m side shift	99930.6	0.07	37.24	2.94	0.1029	2.88
v-guide 2: 1e-4 m side shift	98830.4	1.17	34.25	10.73	0.1030	3.02
v-guide 2: 1e-3 m side shift	65561.1	34.44	30.76	19.84	0.0890	11.04
v-guide 2: 1 deg rotation	70992.7	29.01	37.75	1.62	0.0532	46.84
v-guide 2: 2 deg rotation	52298.9	47.70	37.35	2.64	0.0366	63.35
v-guide 2: 5 deg rotation	24754.4	75.25	44.74	16.60	0.0116	88.36
v-guide 2: 1e-3 m size increase	48967.4	51.03	35.28	8.05	0.0878	12.16
v-guide 2: 2e-3 m size increase	28992.7	71.01	38.81	1.16	0.0275	72.46

Table E-2 ACU simulation contact parameter estimates - v-guide 3 modifications

	Stiffness		Damping		Coeff. of Friction	
Modification	**Value (N/m)**	**Error (%)**	**Value (kg/s)**	**Error (%)**	**Value**	**Error (%)**
Expected parameter values	100000.0	--	38.37	--	0.1000	--
No geometry modifications	99992.7	0.01	37.54	2.16	0.1028	2.80
v-guide 3: 1e-3 m back shift	100003.0	0.00	37.4	2.54	0.1028	2.78
v-guide 3: 2e-3 m back shift	100020	0.02	37.44	2.41	0.1027	2.74
v-guide 3: 5e-3 m back shift	100070.0	0.07	37.59	2.04	0.1026	2.62
v-guide 3: 1e-6 m forward shift	99992.6	0.01	37.54	2.16	0.1028	2.80
v-guide 3: 1e-5 m forward shift	99993.4	0.01	37.56	2.11	0.1028	2.80
v-guide 3: 1e-4 m forward shift	100015.0	0.02	37.61	1.97	0.1024	2.43
v-guide 3: 3e-4 m forward shift	100378.0	0.38	37.85	1.33	0.0981	1.92
v-guide 3: 6e-4 m forward shift	99394.0	0.61	33.07	13.80	0.1070	6.98
v-guide 3: 1e-3 m forward shift	93257.7	6.74	29.17	23.97	0.0986	1.41
v-guide 3: 2e-3 m forward shift	62887.8	37.11	35.07	8.60	0.1145	14.49
v-guide 3: 3e-3 m forward shift	43935.9	56.06	35.30	7.99	0.1175	17.53
v-guide 3: 1e-6 m side shift	99987.2	0.01	37.50	2.27	0.1028	2.80
v-guide 3: 1e-5 m side shift	99935.9	0.06	37.14	3.19	0.1028	2.78
v-guide 3: 1e-4 m side shift	98813.3	1.19	33.26	13.31	0.1025	2.49
v-guide 3: 1e-3 m side shift	65587.8	34.41	22.64	40.99	0.0781	21.89
v-guide 3: 1 deg rotation	70530.3	29.47	37.08	3.35	0.0648	35.23
v-guide 3: 2 deg rotation	52201.0	47.80	38.57	0.52	0.0507	49.29
v-guide 3: 5 deg rotation	24711.7	75.29	45.24	17.92	0.0213	78.70
v-guide 3: 1e-3 m size increase	50143.5	49.86	36.52	4.82	0.0498	50.23
v-guide 3: 2e-3 m size increase	29386.2	70.61	45.05	17.43	0.0101	89.86

Table E-3 ACU simulation contact parameter estimates - v-guide 4 modifications

	Stiffness		Damping		Coeff. of Friction	
Modification	**Value (N/m)**	**Error (%)**	**Value (kg/s)**	**Error (%)**	**Value**	**Error (%)**
Expected parameter values	100000.0	--	38.37	--	0.1000	--
No geometry modifications	99992.7	0.01	37.54	2.16	0.1028	2.80
v-guide 4: 1e-3 m back shift	100019.0	0.02	37.3	2.67	0.1027	2.74
v-guide 4: 2e-3 m back shift	100051	0.05	37.3465	2.66	0.102705	2.71
v-guide 4: 5e-3 m back shift	100116.0	0.12	37.69	1.76	0.1022	2.23
v-guide 4: 1e-6 m forward shift	99992.6	0.01	37.54	2.16	0.1028	2.80
v-guide 4: 1e-5 m forward shift	99992.6	0.01	37.54	2.15	0.1028	2.81
v-guide 4: 1e-4 m forward shift	100026.0	0.03	37.61	1.97	0.1024	2.44
v-guide 4: 3e-4 m forward shift	99979.2	0.02	37.98	1.01	0.1243	24.30
v-guide 4: 6e-4 m forward shift	98483.8	1.52	36.78	4.13	0.1352	35.15
v-guide 4: 1e-3 m forward shift	92931.6	7.07	35.51	7.45	0.1098	9.82
v-guide 4: 2e-3 m forward shift	63634.2	36.37	42.29	10.23	0.0478	52.17
v-guide 4: 3e-3 m forward shift	44363.1	55.64	38.29	0.21	0.0332	66.82
v-guide 4: 1e-6 m side shift	99983.7	0.02	37.51	2.22	0.1028	2.79
v-guide 4: 1e-5 m side shift	99899.5	0.10	37.34	2.69	0.1027	2.66
v-guide 4: 1e-4 m side shift	98583.0	1.42	35.31	7.96	0.1003	0.33
v-guide 4: 1e-3 m side shift	65534.3	34.47	30.99	19.22	0.0818	18.19
v-guide 4: 1 deg rotation	71049.2	28.95	41.27	7.56	0.0529	47.10
v-guide 4: 2 deg rotation	52344.2	47.66	45.57	18.76	0.0337	66.33
v-guide 4: 5 deg rotation	24771.7	75.23	50.33	31.18	0.0114	88.55
v-guide 4: 1e-3 m size increase	48893.2	51.11	37.66	1.84	0.0883	11.67
v-guide 4: 2e-3 m size increase	29195.4	70.80	44.01	14.70	0.0190	80.98